THREE-DIMENSIONAL SIMULATION OF ARBITRARY CRACK GROWTH

A Dissertation

Presented to the Faculty of the Graduate School

of Cornell University

In Partial Fulfillment of the Requirements for the Degree of

Doctor of Philosophy

by

Brett Richard Davis

August 2014

THREE-DIMENSIONAL SIMULATION OF ARBITRARY CRACK GROWTH

Brett Richard Davis, Ph.D.

Cornell University 2014

A finite-element-based simulation technique is developed in Chapter 1 to predict arbitrary shape evolution of 3-D, geometrically explicit cracks under stable growth conditions. Point-by-point extensions along a crack front are predicted using a new, energy-based growth formulation that relies on a first-order expansion of the energy release rate. The key term in this expansion is the variation of energy release rate, made readily available via the virtual crack extension (VCE) method. The variation of energy release rate acts as an influence function relating changes in applied load to geometry changes along the crack front. The crack-growth formulation is incorporated into an incremental-iterative solution procedure that continually updates the crack configuration by re-meshing. The numerical technique allows crack shapes to evolve according to energy-based mechanics, while reducing the effects of computational artifacts, e.g. mesh bias. Chapter 1 offers three simulations of mode I, planar crack growth as proof-of-concept of the new technique.

To extend the simulation approach to more general crack growth situations, Chapter 2 presents a new implementation for decomposing 3-D mixed-mode energy release rates using the VCE method. The technique uses a symmetric/anti-symmetric approach to decompose local crack-front displacements that are substituted into the

global VCE energy release rate form. The subsequent expansion leads to the mixed-mode energy release rate expressions. As a result of the expansion, previously unaddressed modal-interaction coupling terms are found to impact the mixed-mode energy release rates. Five numerical examples are presented as verification of the implementation. This development expands the VCE method's advantages over similar procedures when simulating arbitrary crack growth.

The energy-based growth formulation and accompanying simulation technique is generalized in Chapter 3 to predict arbitrary, mixed-mode, non-planar crack evolution. The implementation uses a novel basis-function approach to generate a crack extension expression, rather than relying on the local, point-by-point approach described in Chapter 1. The basis-function expression dampens the effect of numerical noise on crack growth predictions that could otherwise produce unstable simulation results. Two simulations are presented to demonstrate the technique's ability to capture both general non-planar behavior, as well as local mixed-mode phenomena, e.g. "factory-roof" formation, along the crack front.

BIOGRAPHICAL SKETCH

Brett was born July 27, 1986 to loving parents Harvey and Jane in Schenectady, NY. He is the eldest of two siblings, Sean and Courtney. The young Davis family grew up together in Guilderland, NY a suburb of Albany and Schenectady. Brett's bond to his family became even stronger after suffering the loss of his father at an early age, an event that truly shaped his life.

A product of the New York State public school system, Brett graduated from Guilderland High School in June 2004. At GHS, Brett excelled academically as well as on the lacrosse field. He continued his public education at the University of Virginia in Charlottesville. In May 2008, Brett earned a Bachelor of Science degree in Civil and Environmental Engineering with High Distinction while minoring in Economics. In June 2008, he began studying under Professor Ingraffea at Cornell University as a member of the Cornell Fracture Group.

Brett enjoys a balanced life. He prefers to be active and outdoors, whether it's sailing, golf, tennis, lacrosse, etc. He takes great pride in being the first Cornell Summer Softball team captain in 35 years to bring his advisor, Professor Ingraffea, a championship. Brett loves being with friends and family, spending time at the beach, on the water or in the Adirondacks.

To my family

“Life is far too important a thing ever to talk seriously about.”

- Oscar Wilde, *Lady Windermere’s Fan*

ACKNOWLEDGEMENTS

I would first like to thank my advisor, Professor Anthony Ingraffea, for the opportunity to continue my education at Cornell University. I truly value the experience of being under his leadership; it has formed me both as a young engineering professional and an individual of society. I cannot thank him enough. I would also like to thank the members of my special committee for their guidance and support: Professors A.T. Zehnder, W. Aquino, and C.J. Earls.

Thanks are also extended to my fellow co-authors: Dr. Paul Wawrzynek for his countless technical insights, Dr. Changyu Hwang for his assistance with the VCE method, and especially, Dr. Bruce Carter for being the go-to-guy for pretty much everything. I am also grateful for the conversations and software help received from Dr. Gerd Herber.

I would like to express gratitude to the engineers and researches at NASA Langley Research Center with whom I have collaborated, specifically: Drs. Wade Jackson, James Ratcliffe, and Ronald Krueger. A special thanks is extended to Dr. Michael Czabaj for being there to answer questions, bounce ideas off of, and review papers among other things.

Thanks to all the Cornell Fracture Group members past and present. Albert and Ashley, I'm glad we shared this journey together. Bruce was there to keep us in line. Finally, to Mother, Sean, Sister and Sarah, thanks for doing what you do.

This thesis was funded by the NASA University Institutes Project under Grant NCC3-989, and the Cornell University Ross-Tetelman Fellowship.

TABLE OF CONTENTS

LIST OF FIGURES

LIST OF TABLES

LIST OF ABBREVIATIONS

DCB	double cantilever beam
DOF	degrees of freedom
GVCE	global virtual crack extension
MUMPS	multifrontal massively parallel sparse direct solver
SLB	single leg bending
VCCT	virtual crack closure technique
VCE	virtual crack extension
XFEM	extended finite element method

LIST OF SYMBOLS

Parameters

a	crack length
$\boldsymbol{b}$	crack-growth basis function
E	Young's modulus
f	applied force vector
G	energy release rate
G_c	critical energy release rate
$G_{I,II,III}$	modal energy release rate
h	height of crack front element
K	stiffness matrix
$K_{I,II,III}$	modal stress intensity factor
ℓ	virtual extension effective width
l	length of crack front element
n	number of basis functions
r_t	crack-front template radius
s	normalized position along crack front
u	nodal displacement vector
v	crack-front extension vector
w	width of crack-front element
α	virtual extension angle increment
β	bounding angle for virtual extensions
μ	shear modulus
ν	Poisson's ratio
Π	potential energy
φ	virtual extension angle
δa	local virtual crack-front extension
δA	area associated with virtual crack-front extension

$\delta \boldsymbol{b}$	global virtual basis-function extension
$\frac{\delta G_i}{\delta a_j}$	local variation of energy release rate
$\frac{\delta G_i}{\delta b_k}$	global basis-function variation of energy release rate
Δa	local crack extension increment
$\Delta \boldsymbol{a}$	crack-front extension function
Δb	basis-function coefficient
ΔP	total applied load increment
ΔP_c	critical applied load increment
ΔP_g	super-critical applied load increment

Subscripts

c	critical value
g	super-critical value
I, II, III	fracture modes
i, j	crack-front positions
k	individual basis function
L	local crack-front coordinate system designation
m	mobilized crack-front positions
s	stationary crack-front positions

Superscripts

0	current load condition
1	target load condition

CHAPTER 1

3-D SIMULATION OF ARBITRARY CRACK GROWTH USING AN ENERGY-BASED FORMULATION: PLANAR GROWTH

1.1 Introduction

Many finite-element-based techniques have been developed and utilized for simulating crack propagation, and these techniques can be generally divided into two categories: (1) non-geometrical representations, and (2) geometrical representations [1]. The first category uses constitutive relations or kinematic methods to inform the numerical model of a crack's presence. The second uses modeling techniques to represent explicitly the front and surfaces of the crack as geometrical features. Both forms of crack representation then employ crack growth methods to advance the shape of the front. As highlighted in the following paragraphs, the prediction of crack advance for many numerical methods is often restricted or even entirely governed by numerical artifacts, such that crack-shape evolution is not predicted based on physical, cracking mechanisms.

The category of non-geometric crack growth simulation approaches includes damage mechanics and routines using the extended finite-element method (XFEM).

Damage mechanics uses selected fields to construct a damage parameter that effectively degrades element constitutive properties [2,3]. Crack-front evolution can be inferred based on inspection of elements that have suffered sufficient damage to

constitute new crack advance [4]. Since element-constitutive relationships govern crack-front locations and their potential advances, crack representations can be diffuse and the predicted evolution biased by the geometry of the finite-element mesh [5–7]. Crack-shape evolution is neither arbitrary nor unique, but dictated by element orientation and size, allowing different front predictions for different meshes.

XFEM uses additional enrichment functions to represent cracks within finite-elements. These augmented elements numerically reproduce the discontinuities across crack faces and the appropriate stress fields near the front associated with a physical crack [8–10]. The XFEM representation can then be coupled with a variety of techniques (e.g. damage mechanics [11], cohesive models [12], and prescribed-increment methods [13,14]) to simulate growth. Compared to explicit representations of cracks, the use of XFEM obviates the need for re-meshing at the expense of more complex book-keeping and numerical quadrature. It is important to distinguish XFEM as a method for representing cracks, not as a direct approach that predicts growth and shape evolution of cracks.

Alternatively, conventional finite-element-based methods can utilize a geometrically explicit crack representation to predict growth. These include cohesive-zone methods extended from early classical models of Dugdale [15] and Barrenblatt [16], nodal-release methods, adaptive-finite-element methods, and constrained-optimization approaches.

Geometrically explicit cohesive-zone methods use special elements governed by traction-separation functions that capture behavior at the crack front. When the traction-separation relationship reaches its limit, the cohesive element ceases to

transmit tractions, thereby creating new zero-traction surfaces and extending the crack [17,18]. Crack-shape evolution is therefore constrained by the size, shape, orientation, and locations of the cohesive elements. Since it is computationally intensive to place cohesive elements throughout an entire model, they are often inserted at predetermined locations along the expected crack path, limiting the ability to predict crack-shape evolution.

Nodal-release methods compare fracture mechanics parameters to critical values to determine whether a point along the crack front is to advance. The nodes along the crack front that exceed the critical value are released, creating new surface area that extends the front [19–21]. As in the cohesive-element approach, the crack-shape evolution can only follow existing element boundaries, restricting the direction and distance of the predicted advance of the crack front.

The cohesive-element and nodal-release approaches have the potential to produce jagged crack fronts that do not match observed configurations [20,21]. Some have used a heavily refined mesh throughout the entire model or a locally refined mesh around the crack front to mitigate mesh-biased shape evolution [22]. The high level of refinement greatly inflates the computational cost. Another option is to produce meshes constructed with *a priori* knowledge of the future crack geometry. However, this latter technique contradicts the notion of predicting arbitrary evolution by linking a physical feature (expected crack-front shape) with a computational artifact (the mesh). For example, with an initial circular flaw, one might design a mesh that contains an organization of elements in a concentric circular pattern around the initial crack front.

Another geometric approach to predict crack growth is adaptive-finite-element methods with re-meshing schemes [23,24]. These techniques have the ability to advance the crack front in an arbitrary direction given a prescribed magnitude. In this case, crack growth is a local prediction; growth at a point along the front is based on the fracture parameters at that point only. The magnitude of the advance can be proportioned along the front based on the distribution of fracture-parameter values or empirical growth laws [25,26]. Once the crack front is advanced, a new finite-element mesh is generated around the updated front. This allows the non-uniform evolution of the crack shape to be simulated. However, the growth is still restricted by a predetermined maximum extension size. Despite having the ability to capture non-uniform advances, the entire front or a significant section of the front is typically advanced at once, which might not be realistic. In some cases, certain portions of a crack front might advance, while others remain stationary.

Other geometrically explicit methods frame crack growth as a constrained optimization problem rather than a series of local extensions along the front. The shape of the front is updated to maximize the energy-released subject to a prescribed area of advance and critical-energy value [27,28]. However, there is no guarantee the correct crack shape for a given load will be identified. Knowledge of the expected growth path is often introduced to expedite the constrained optimization procedure.

The objective of this chapter is to describe and demonstrate a computational methodology that enables prediction of arbitrary crack geometry evolution that is realistic and generally unbiased by finite-element artifacts. Other crack growth methods rely on *a priori* information of the future shape or mesh geometry. However,

of interest here are complex, initial crack geometries with unknown crack-shape evolution.

The simulation technique developed in this chapter incorporates three main components: (1) explicitly representing cracks with re-meshing capabilities, (2) calculating fracture parameters (e.g. energy release rate, G) via the Virtual Crack Extension (VCE) method, and (3) predicting growth using a new energy-based formulation. For this work a geometrically explicit representation of the crack front was considered more practical and effective. Continually updating and re-meshing around an explicit front ensures the arbitrary nature of the evolution. The VCE method is attractive because of its potential energy approach to calculate both energy release rate and, more importantly, the variation of energy release rate – the critical parameter in the energy-based growth formulation.

The salient contribution of this work is the development and implementation of the aforementioned energy-based growth formulation within an iterative solution procedure. The formulation features the expansion of the energy release rate, yielding an explicit expression to calculate point-by-point advances along a crack front. Within the expansion, the variation of energy release rate with respect to crack advance is used as an influence function. This function provides the mechanics for the interaction of points along the crack front, which allows the capture of arbitrary front evolution. The scope of this chapter's algorithmic implementation is restricted to planar, stable crack-growth, making it applicable to delamination problems in composite structures, for example. However, the energy-based growth formulation

has the potential to be applied within a generalized approach for situations that might involve non-planar or unstable growth, as demonstrated in Chapter 3.

The next section will provide background and a description of the VCE method. The following sections will introduce the foundation and implementation of the energy-based growth formulation. The algorithm and iterative approach for arbitrary crack growth will also be detailed. Finally, three simulations are offered as proof-of-concept and verification. The first two show the uniform and curvilinear growth of an initially straight crack in a double cantilever beam specimen. The third simulation tracks the evolution of an embedded, initially elliptical crack subject to equal and opposite crack face point loads.

1.2 Virtual crack extension method

A novel contribution of the new energy-based method for simulating crack evolution is the use of the first-order variation of energy release rate with respect to crack advance. This rate of energy release rate, in the 3-D sense, serves as an influence function that relates an extension at one point along a crack front to the energy release rates elsewhere along the front. Both the energy release rate and rate of energy release rate are used within the energy-based growth formulation, to be discussed in Section 1.3. The VCE method is an attractive and efficient way to extract both energy release rates and rates of energy release rate. It provides an alternative to using a finite-difference approach to estimate rates of energy release rate. The finite

difference approach has well known deficiencies associated with selecting accurate and numerically stable finite perturbations, as well as being computational costly, requiring a complete finite-element analysis for each discretized crack-front position.

The VCE method, also known as the stiffness derivative method, was first introduced by Dixon and Pook [29] and Watwood [30], and further developed by Hellen [31] and Parks [32]. Through applications of variational principle theory, a direct-integration approach simplified the VCE method and improved efficiency [33–35]. Hwang *et al.*, utilized the formulation of [34], generalizing the technique for planar 3-D cracks [36]. The work in [36] provides the direct integral expressions for stiffness derivatives, energy release rate, and higher order derivatives of energy release rate. This section offers a brief introduction into the foundation of the VCE method. For a more complete formulation and discussion see [34–36].

1.2.1 Virtual crack extension formulation

The potential energy, Π, of a finite-element system is given by

$$\Pi = \frac{1}{2} u^T K u - u^T f \ , \tag{1.1}$$

where u, K, and f are the displacement vector, the stiffness matrix, and the applied force vector, respectively.

The energy release rate, G, at crack-front position i is defined as the negative variation of the potential energy with respect to a virtual, incremental, crack-front extension, δa, in the normal direction of the front at that position:

$$G_i \equiv -\frac{\delta \Pi}{\delta A_i} = -\frac{\delta \Pi}{\delta a_i \ell_i}. \tag{1.2}$$

In the 3-D sense, the virtual extension has an associated area, δA_i, comprised of a virtual extension, δa_i, and an effective width, ℓ_i. Applying the variation to the finite element expression for potential energy leads to the following:

$$G_i = -\frac{1}{\ell_i}\left(\frac{1}{2}\frac{\delta u}{\delta a_i}^T Ku + \frac{1}{2}u^T \frac{\delta K}{\delta a_i}u + \frac{1}{2}u^T K \frac{\delta u}{\delta a_i} - \frac{\delta u}{\delta a_i}^T f - u^T \frac{\delta f}{\delta a_i}\right), \tag{1.3}$$

$$G_i = -\frac{1}{\ell_i}\left(\frac{\delta u}{\delta a_i}^T (Ku - f) + \frac{1}{2}u^T \frac{\delta K}{\delta a_i}u - u^T \frac{\delta f}{\delta a_i}\right). \tag{1.4}$$

By maintaining finite element equilibrium, $Ku - f = 0$, the expression for energy release rate becomes:

$$G_i = -\frac{1}{\ell_i}\left(\frac{1}{2}u^T \frac{\delta K}{\delta a_i}u - u^T \frac{\delta f}{\delta a_i}\right). \tag{1.5}$$

For simplicity in the current implementation, it is assumed that applied forces are not influenced by the virtual incremental extensions, and the variational force term,

$\frac{\delta f}{\delta a_i}$, is zero. The necessary parameters required for a local energy release rate calculation at position i are displacements, u, and variation in stiffness due to a virtual incremental crack extension, $\frac{\delta K}{\delta a_i}$. The simplification reduces Eq. (1.5) to:

$$G_i = -\frac{1}{\ell_i}\left(\frac{1}{2}u^T \frac{\delta K}{\delta a_i}u\right). \tag{1.6}$$

Note that if the virtual extensions do alter the applied load, f, (e.g. by the presence of crack-face pressures, thermal, and/or body force loadings) the effect must be accounted for with the variational force term, $\frac{\delta f}{\delta a_i}$, and included throughout the derivations. Non-zero contributions to the stiffness variation only occur over elements that experience the virtual extension. This observation simplifies calculations and implementation of the method.

The expression for the first-order variation of the energy release rate with respect to incremental crack extension, δa_j, follows from Eq. (1.6):

$$\frac{\delta G_i}{\delta a_j} = -\frac{1}{\ell_i}\left(u^T \frac{\delta K}{\delta a_i}\frac{\delta u}{\delta a_j} + \frac{1}{2}u^T \frac{\delta^2 K}{\delta a_i \delta a_j}u\right). \tag{1.7}$$

In addition to displacements and the variation in stiffness, the rate of energy release rate, $\frac{\delta G_i}{\delta a_j}$, depends on the variation in displacements, $\frac{\delta u}{\delta a_j}$, and the second-order stiffness variation, $\frac{\delta^2 K}{\delta a_i \delta a_j}$. The $\frac{\delta u}{\delta a_j}$ term relates the influence of a virtual crack extension to the

global displacements. The $\frac{\delta^2 K}{\delta a_i \delta a_j}$ term captures the local interaction of two adjacent virtual crack-front extensions and their effect on the stiffness. This is illustrated by Figure 1.1, showing the overlapping area between two adjacent virtual extensions and the associated non-zero contribution. Also shown in Figure 1.1 is the zero contribution to the second-order stiffness variation from non-adjacent virtual extensions.

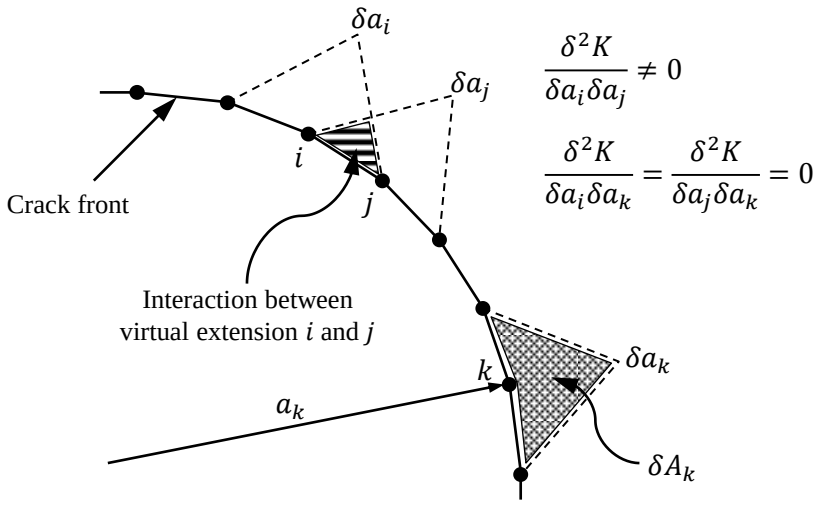

Figure 1.1. Illustration of interaction between virtual extensions at adjacent nodes (i and j). This interaction is accounted for by a non-zero second-order stiffness derivative. Virtual extensions at non-adjacent nodes have no interaction.

To calculate the energy release rate and its variation, virtual extensions are applied at each position along the crack front creating virtual "strains". Through the Jacobian and finite-element basis functions, the virtual "strains" are used to formulate the

variations in the strain-displacement relation, $\frac{\delta B}{\delta a_i}$, providing the components necessary for the explicit integral expressions of the stiffness variations:

$$\frac{\delta K}{\delta a_i} = \int_V \left[\frac{\delta B^T}{\delta a_i} DB + B^T D \frac{\delta B}{\delta a_i} + \frac{\delta |J|}{\delta a_i} B^T DB \right] dV, \tag{1.8}$$

where V is volume, D is the constitutive relationship, B is the strain-displacement relationship and $|J|$ is the determinant of the Jacobian. The second-order stiffness variation and other required expressions can be found in [36].

1.3 Energy-based prediction of crack growth

The new energy-based method for prediction of crack evolution is governed by an energy release rate balance equation. By employing a critical value for energy release rate, the change in energy release rate due to an applied-load increment can be divided into critical and super-critical portions. Within an iterative scheme, the superfluous energy provides the impetus for crack growth and is used within the balance equation to calculate point-wise advances along the crack front. The front is iteratively updated through re-meshing schemes, until a stable crack-shape configuration is reached, where all points along the front are at or below the critical energy release rate value.

1.3.1 Energy-based prediction of crack growth

The crack-growth formulation extends directly from a first-order expansion of the energy release rate:

$$G_i^1 = G_i^0 + \frac{\delta G_i}{\delta P} \odot \Delta P_i + \frac{\delta G_i}{\delta a_j} \Delta a_j. \tag{1.9}$$

Although others have investigated various expansions of fracture mechanics parameters [37], the simple energetic form expressed in Eq. (1.9) lends itself well to numerical implementation. The target energy release rate, G_i^1, is expanded into three components: G_i^0, the current energy release rate prior to an applied increment ΔP_i; $\frac{\delta G_i}{\delta P} \odot \Delta P_i$*, the portion due to change in loading; and $\frac{\delta G_i}{\delta a_j} \Delta a_j$, the portion due to crack extension. Here $\frac{\delta G_i}{\delta P}$ characterizes the change in energy release rate with respect to the loading; $\frac{\delta G_i}{\delta a_j}$ is the aforementioned influence function – the first-order variation of energy release rate calculated from the VCE method; and Δa_j is the crack extension increment. The calculation of the $\frac{\delta G_i}{\delta P}$ term will be discussed in Section 1.3.2. The components of Eq. (1.9) have physical meaning, taking into consideration the energy available at the crack front, the contribution from loading, and the contribution from crack growth. Note that Eq. (1.9) neglects higher order terms and other forms of energetic dissipation, such as heat and sound, which are assumed to be negligible.

* $\odot$ denotes the component-wise multiplication of two vectors, $a_i = b_i \odot c_i$

The expanded energy release rate forms a general stability balance equation that can be manipulated to calculate growth increments along an arbitrary crack front for a given load change. To create an effective balance equation, a local failure criterion, representing the material toughness, must be selected. For simplicity in the current implementation, a local critical energy release rate, G_{ic}, is set as the failure criterion. However, the formulation is not limited to this simplification. For example, effective energy release rates comprised of decomposed modes subject to power laws can be incorporated easily.

Two primary assumptions constrain the growth formulation to make results physically meaningful. The first asserts that the crack front cannot retreat or "heal" itself (i.e. the advances are all positive or zero):

$$\Delta a_i \geq 0. \tag{1.10}$$

The second assumption restricts the target energy release rate from exceeding the critical value, described in Eq. (1.11). Analogous to the concept of a yield surface in plasticity theory, the crack front cannot exist at energy release rate levels above the material's critical value:

$$G_i^1 \leq G_{ic}. \tag{1.11}$$

Eq. (1.11) serves as the stability condition for a crack-front configuration. If Eq. (1.11) holds at all points along a crack front, the front is considered stable. The violation of Eq. (1.11) indicates a required update to the shape of the front.

Substituting the local failure condition, $G_i^1 = G_{ic}$, into the general stability balance Eq. (1.9) yields the following local growth condition:

$$G_{ic} = G_i^0 + \frac{\delta G_i}{\delta P} \odot \Delta P_i + \frac{\delta G_i}{\delta a_j} \Delta a_j. \tag{1.12}$$

The general growth condition, with the aforementioned assumptions, forms the energy-balance equation that is implemented within the simulation approach to predict arbitrary crack growth.

1.3.2 Implementation of the energy-based crack-growth formulation

The energy-based crack-growth balance formulation, Eq. (1.12), is embedded within an incremental-iterative simulation algorithm depicted in Figure 1.2. The simulation technique incorporates finite-element model generation, analysis, fracture mechanics calculations, the crack-growth formulation, and crack-front geometry updates via re-meshing. This procedure requires a current stable crack-front configuration, i.e. $G_i^0 \leq G_{ic}$. The finite-element model is incrementally loaded. If crack growth is not predicted based on the criterion in Eq. (1.11), the algorithm is allowed to proceed to the next load increment without any change to the crack-front geometry. If crack-growth is predicted, Eq. (1.12) is used to update iteratively the

crack-front shape (i.e. Δa_i) until a stable configuration is reached. It is assumed that for a stable crack-growth problem, a stable front configuration for a given load increment can be found. Once the new, stable shape has been predicted, the simulation continues with additional loading increments. The remainder of Section 1.3.2 describes the calculations and implementation of the crack-growth formulation. Section 1.3.3 discusses re-meshing of the updated crack front.

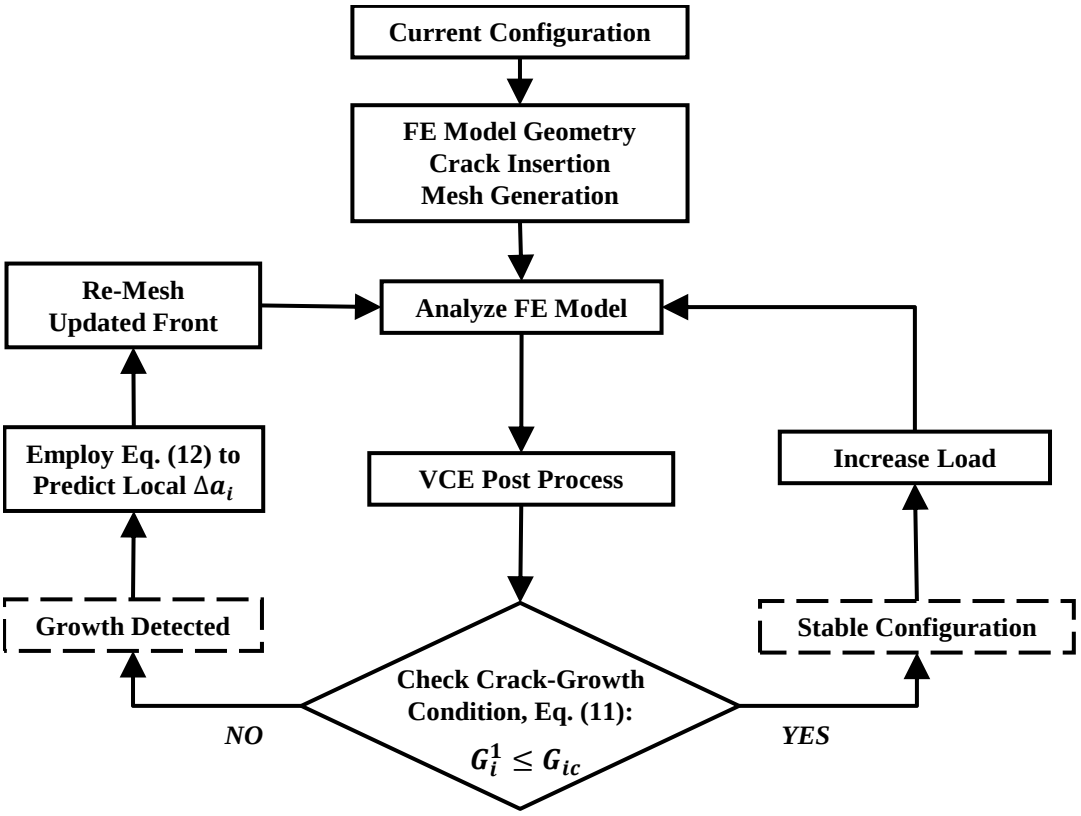

Figure 1.2. High level schematic of iterative crack-growth simulation algorithm.

The VCE method is used to calculate energy release rates along the crack front. Energy release rates need to be extracted for both the current stable configuration, G_i^0,

and after a target applied-load increment, G_i^1. These vector quantities represent the energy release rate for each position along a discretized crack front.

At the current load level, the crack-front configuration is stable; for all points along the front $G_i^0 < G_{ic}$. After the load increment, ΔP_i, is applied, the energy release rates are checked again. G_i^1 results are compared to the critical values from the local failure criterion, G_{ic}, to determine if a growth condition is reached, Eq. (1.11). Points along the front are separated into mobilized, $G_i^1 > G_{ic}$, and stationary points, $G_i^1 \leq G_{ic}$, as denoted in Figure 1.3. As the notation implies, the mobilized points violate Eq. (1.11) and are expected to advance, while the stationary points will remain at their current position for the current iteration. The presence of mobilized positions signals an update to the front geometry is required. One can now write $G_i = G_m + G_s$, where subscripts m and s reference the sets for mobilized and stationary points, respectively.

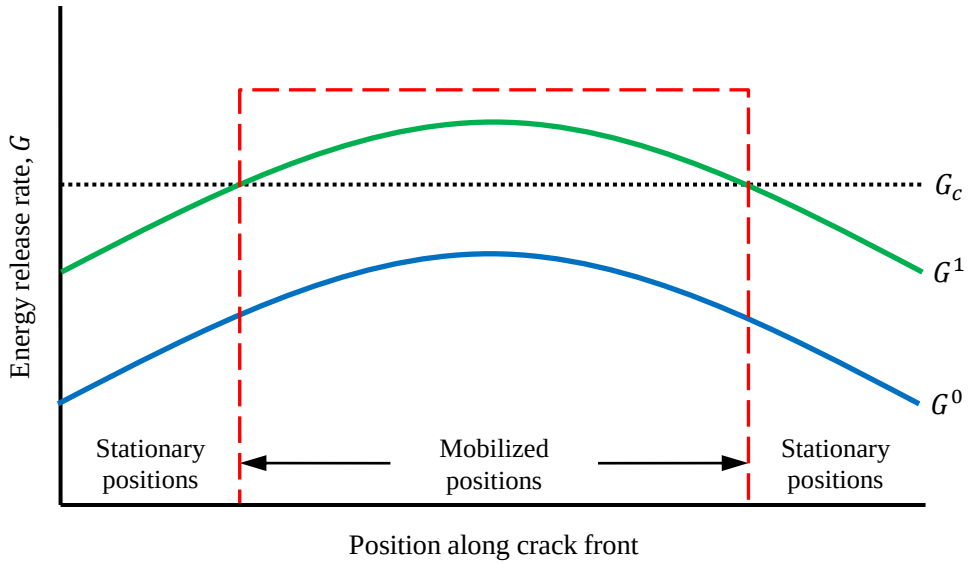

Figure 1.3. Schematic for energy release rates along the crack front at the current (G^0) and target (G^1) load levels. A constant G_c is portrayed; the sets of mobilized and stationary positions along the front are denoted accordingly. A growth condition has been reached.

As depicted schematically in Figure 1.4, for mobilized positions the target load increment, ΔP_i, can be decomposed into ΔP_{ic} (a loading increment that results in the energy release rate reaching a critical value) and ΔP_{ig} (a super-critical loading increment that contributes to local crack growth):

$$\Delta P_m = \Delta P_{mc} + \Delta P_{mg}. \tag{1.13}$$

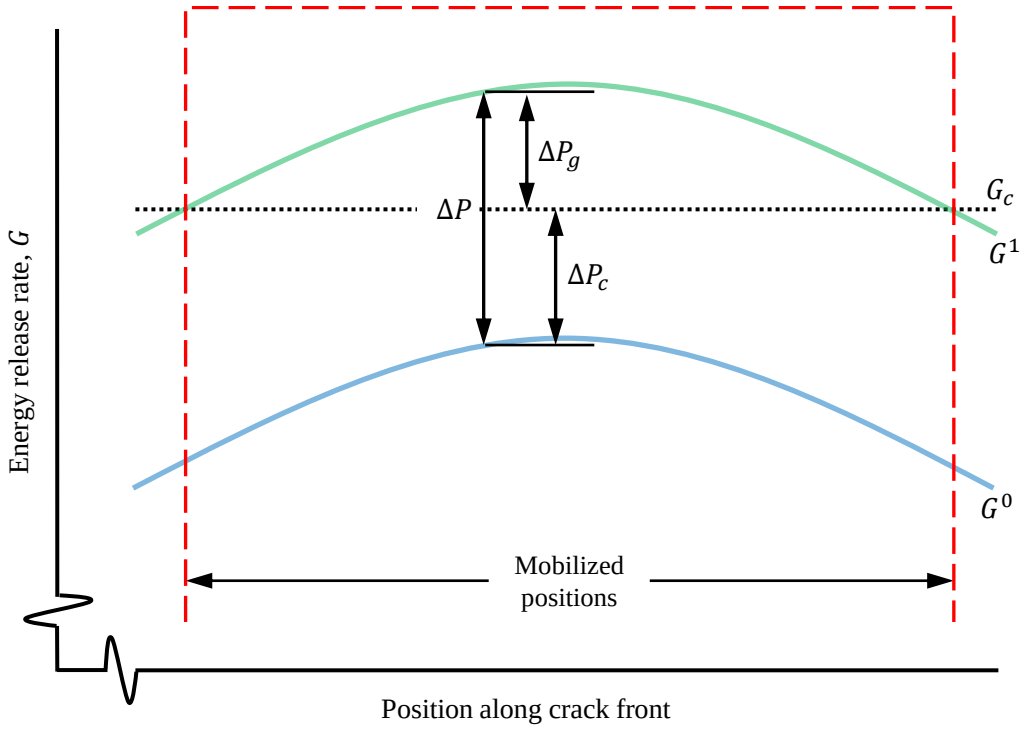

Figure 1.4. For the set of mobilized positions, the target load increment, ΔP, is divided into portions that contribute to reaching a critical condition, ΔP_c, and that contribute to growth, ΔP_g.

The stability equation, Eq. (1.12), is rearranged to determine the non-zero values of ΔP_{mc}. It is assumed that the front geometry remains unchanged, i.e. $\Delta a_i = 0$. This

implies that ΔP_{mc} is associated with the current crack configuration and does not involve energy change related to growth. Therefore, for the set of mobilized positions:

$$\Delta P_{mc} = \frac{\delta G_m}{\delta P}^{-1} \odot (G_{mc} - G_m^0), \tag{1.14}$$

where G_{mc} and G_m^0 are the critical and current energy release rates, respectively, for mobilized positions. The $\frac{\delta G_m}{\delta P}$ term is obtained through a finite-difference calculation between G_m^1 and G_m^0. ΔP_{mc} represents the load that the current crack positions can withstand before exceeding the material's critical limit and dissipating energy through growth.

The ΔP_{mc} values along the front are subtracted from the target load increment, ΔP_m, to acquire the portion that contributes energy to the system for growth, ΔP_{mg}, at the mobilized positions:

$$\Delta P_{mg} = \Delta P_m - \Delta P_{mc}. \tag{1.15}$$

To calculate the crack extensions, Δa_j, the energy balance described by Eq. (1.12) is updated such that $G_i^0 = G_{ic}$. Substituting the superfluous energy from ΔP_{mg}, and restricting ΔP_{ig} to zero for stationary positions, Eq. (1.12) can be rewritten as:

$$G_{ic} = G_{ic} + \frac{\delta G_i}{\delta P} \odot \Delta P_{ig} + \frac{\delta G_i}{\delta a_j} \Delta a_j. \tag{1.16}$$

Rearranging Eq. (1.16) yields the explicit expression for local crack extensions, Δa_j, at the mobilized positions:

$$\Delta a_j = -\frac{\delta G_i}{\delta a_j}^{-1} \frac{\delta G_i}{\delta P} \odot \Delta P_{ig}. \tag{1.17}$$

Mobilized positions along the crack front are advanced by Δa_j in an outward normal direction while extensions at stationary positions are zero. The crack-front geometry is updated, and re-meshed, which will be discussed in Section 1.3.3. With an updated finite-element model, the iterative process within the current load increment is continued. The updated model is loaded at the current stable level prior to adding ΔP_i. A new G_i^0 is calculated. The target load increment is applied to the updated configuration. A new G_i^1 is calculated. A new set of mobilized and stationary nodes is identified. The next iteration of extensions for the newly mobilized nodes is calculated accordingly. The iterations are continued until a stable configuration is reached for the given target load increment. The stability of the crack-front geometry is achieved when, for all positions along the crack front, the energy release rates are at or below the failure criterion, Eq. (1.11).

The current implementation, using Eq. (1.17) to update the front, operates under the assumption that a stable crack configuration can always be found in a stable crack-growth problem, which implies that the energy release rate generally decreases with crack advance. In the case of an unstable crack-growth problem, where the energy release rate increases with crack advance, the current algorithmic approach and Eq.

(1.17) do not apply. However, the fundamental concept embedded within the energy-based growth formulation, Eq. (1.12), has the potential to be applied in a general algorithm for both stable and unstable crack growth situations.

1.3.3 Application of crack-front extensions and re-meshing

This section outlines the steps for implementing crack growth within a given iteration once the predicted crack-front extensions are calculated.

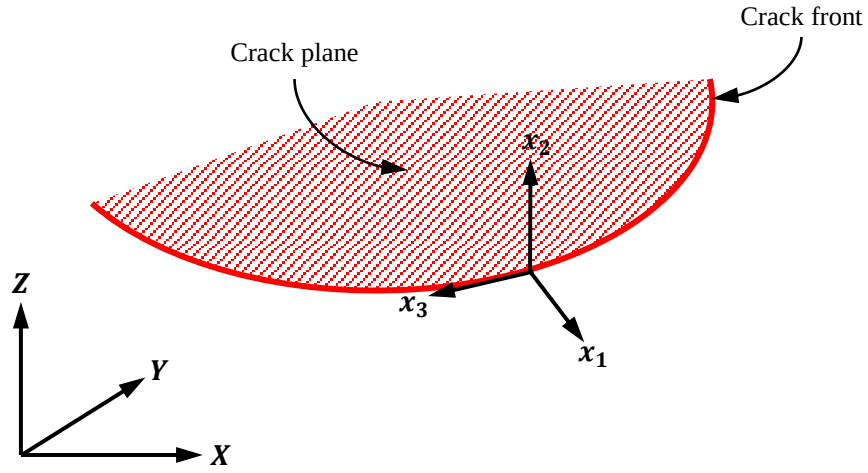

Figure 1.5. Local crack-front coordinate system, x_1, x_2, x_3, for an arbitrarily shaped front in a global coordinate system X, Y, Z.

To apply extensions along an arbitrary crack front, a local coordinate system is defined along the crack front, as depicted in Figure 1.5. The x_1 direction is unit normal to the crack front, the x_2 direction is unit normal to the crack plane, and the x_3 direction is unit tangent to the crack front as determined via the cross product of the x_1 and x_2 unit vectors. Crack-front extensions are applied along the crack-front normal

x_1 direction. As mentioned previously, the current implementation restricts the crack to remain in-plane, keeping x_2 constant.

The resulting crack-front extension vector for a mobilized position is described by:

$$v_n = \Delta a \cdot x_{1n}, \tag{1.18}$$

where Δa is the magnitude of advance at the mobilized position. The applied growth for all iterations within an applied-load increment is based on the current stable crack front. This maintains constant, local front unit normals throughout the increment's iterations. Calculated advances for each iteration can then be summed and stored in a total increment extension vector that is used in the re-meshing process.

At each position, the iterative extension relative to the total extension over the current increment is used as a numerical tolerance as the crack-front shape approaches the stability condition in Eq. (1.11). This indirect tolerance approach was determined to be more robust within the algorithm than explicitly comparing G_i^1 to G_{ic}. For the current implementation, the relative extension tolerance was set to $\frac{\Delta a_{iteration}}{\Delta a_{increment}} \leq 5.0\ x\ 10^{-4}$. If the criterion is satisfied at all mobilized positions along the front, the updated configuration is considered stable; otherwise further extension iterations ensue. This relative extension tolerance corresponds to a direct $\frac{G_i^1 - G_{ic}}{G_{ic}}$ residual tolerance of approximately $1.0\ x\ 10^{-5}$ for stable configurations found in the proof-of-concept simulations in Section 1.4. These tolerances can be altered depending on the nature of the problem.

With continual re-meshing of arbitrarily evolving crack fronts, growth interaction with geometric boundaries must be handled specially. For example, as the growth of a curved crack front advances in a locally normal direction, it is possible for the predicted front to extend outside the boundary of the model, as seen in Figure 1.6. In this case, growth of a point initially located on the free surface is restricted to remain on the free surface, and internal points that are predicted to advance across the boundary are restricted to a location that intersects the model boundary. The largest extension, either from the initial-free-surface position or from the predicted crack-front intersection with the boundary, is taken as the updated position of the crack front along the free surface.

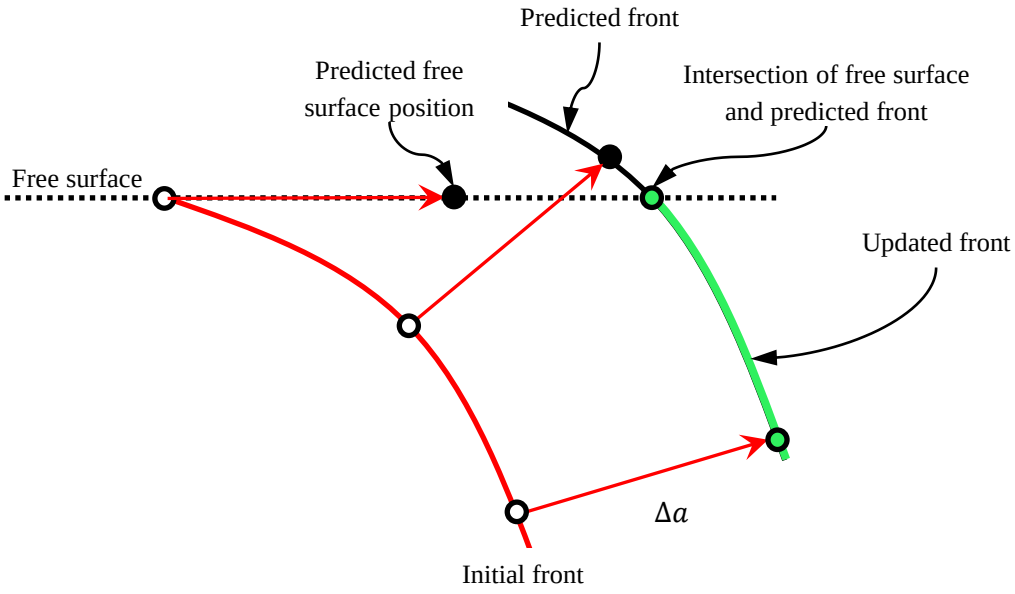

Figure 1.6. Schematic characterizing issues with arbitrary growth along free surfaces. The crack-front position on the free surface is constrained to grow along the free surface. Interior positions grow normal to the front. If the predicted advance of an interior position leads to the crack front intersecting the free surface, that intersection point is compared to the predicted free-surface position. The position further along the free surface is used in the updated re-discretized crack front.

To obtain accurate and reliable simulation results, the crack front must be appropriately discretized. This requires maintaining adequate crack-front-element aspect ratios and node spacing along the advancing crack front. There are various situations that might cause element aspect ratios to deteriorate or a poor distribution of crack-front nodes to arise, which adversely influence simulation results. In the context of an embedded crack, as nodes advance in an outward normal direction, the spacing between nodes increases, modifying initial element aspect ratios and node distribution. Alternatively, advancing nodes on a curvilinear through crack front tend to disperse from the center and accumulate near the free surface boundaries. If too few points represent a section of the front, accurate configurations might not be captured. Additionally, if points are poorly spaced, applied extensions might have a significant effect on other positions. This magnified influence could create oscillations in extension calculations, rendering the iterative approach unstable. To avoid these potential issues, element lengths are adjusted adaptively or the crack front is re-discretized during the simulation. For the latter, a spline function is fit using the predicted positions, creating a mathematical representation of the updated crack front. The spline function is then used to calculate new, appropriately spaced node positions, preserving the updated crack-front geometry.

With the updated crack-front configuration determined, a variety of meshing algorithms can be employed. For the current implementation, a set of elements is placed around the front creating a template that allows for efficient and accurate calculations of energy release rate and rate of energy release rate. This template consists of quarter-point brick (Figure 1.7a) or wedge (Figure 1.7b) elements

immediately surrounding the crack front, and two additional rings of regular quadratic brick elements surrounding the quarter-point elements.

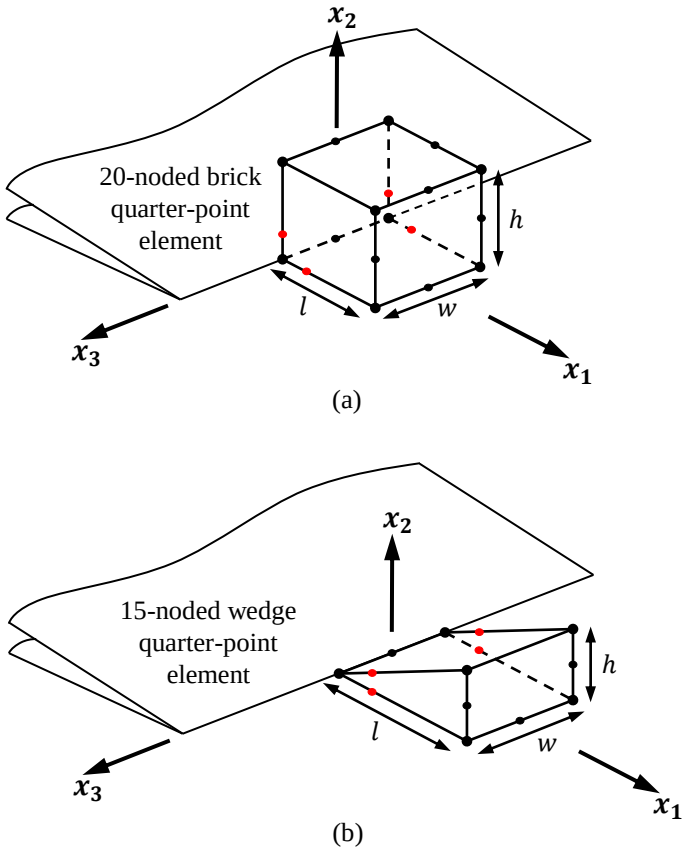

Figure 1.7. Schematics of crack-front quarter-point elements (a) 20-noded bricks and (b) 15-noded wedges.

1.4 Proof-of-concept simulations and results

In this section, three proof-of-concept simulations are presented and compared with published results from the literature to verify and demonstrate the accuracy and

flexibility of the new energy-based growth formulation for predicting 3-D arbitrary crack evolution. Section 1.4.1 describes the simulation of uniform crack growth in a double cantilever beam model. Section 1.4.2 illustrates the simulation of curvilinear crack growth in a double cantilever beam model. Section 1.4.3 shows the evolution of an embedded elliptical crack into a circular configuration.

Custom, in-house software was used for the finite-element re-meshing, crack-front advances, and model generations. The models created for the simulations were imported into the commercial finite-element software ABAQUS/Standard 6.11-1. ABAQUS served as both the finite-element environment and solver. Displacement results from the finite-element analysis were used in the VCE method to calculate G_i and $\frac{\delta G_i}{\delta a_j}$. The fully 3-D verification simulations presented here are capable of predicting the inherent symmetrical crack-shape evolution that arises in each case, rather than enforcing the symmetry through quarter models, for example. More generally and more importantly, however, the toolset allows for the prediction of non-uniform and asymmetric crack-shape evolution that will be demonstrated in Chapter 3 of this dissertation. Note that, with no loss of generality, the proof-of-concept simulations use arbitrary geometries and material properties.

1.4.1 Double cantilever beam: uniform growth

The first simulation, as shown in Figure 1.8, consisted of an initially straight crack front of length $a = 5$ cm in a double cantilever beam (DCB) specimen subject to uniform applied displacements, u_z, along the cantilevered edges. The DCB specimen

material was modeled as isotropic with a unit Young's modulus, $E = 1\ \mathrm{N/cm^2}$, and Poisson's ratio of zero, $\nu = 0$. A constant, local, critical energy release rate for each position, $G_{ic} = 9.4\ x\ 10^{-6}\ \mathrm{N/cm}$, was arbitrarily selected. An initial displacement of $0.100\ \mathrm{cm}$ was applied, followed by an increment of $0.018\ \mathrm{cm}$, and 29 equal increments of $0.005\ \mathrm{cm}$, resulting in a final applied displacement of $0.263\ \mathrm{cm}$. By investigating the analytical derivative of energy release rate with respect to crack length for a DCB specimen, the expected crack growth for this configuration is determined to be inherently stable [38], i.e. G decreases with increasing a, $dG/da < 0$. With $\nu = 0$, the crack front is expected to advance in a self-similar fashion, with the crack length remaining constant across the front.

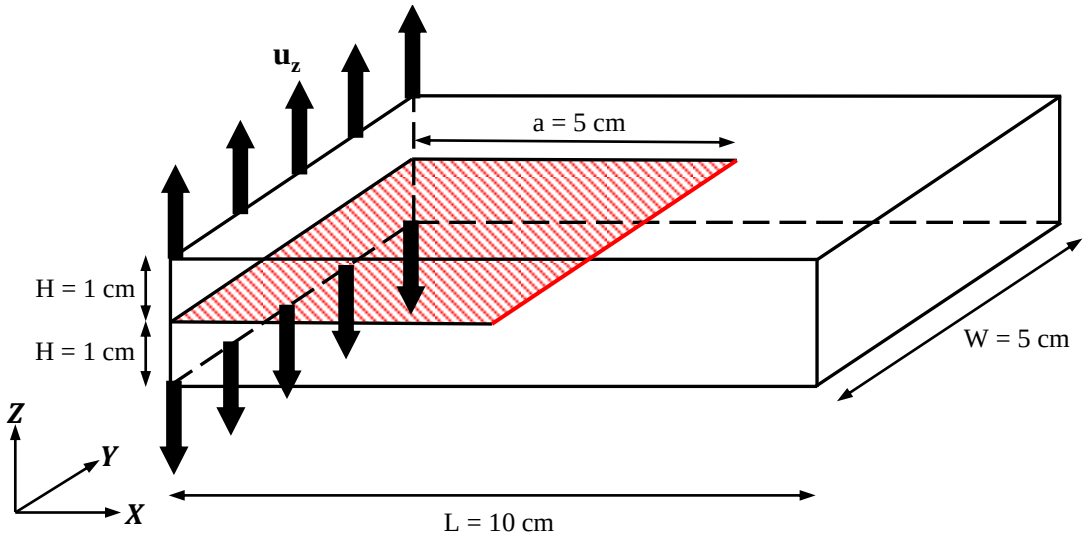

Figure 1.8. Double cantilever beam geometry and boundary conditions for stable crack growth.

The initial finite-element mesh used for the uniform DCB growth simulation is depicted in Figure 1.9. The model was generated using 5,904 quadratic brick and

wedge elements, with a total of 82,887 degrees of freedom. The crack front was discretized into 40 equal segments through the width of the model. The front was surrounded by quarter-point brick elements with the following aspect ratios: $l/a = 0.025$, $l/h = l/w = 1.0$ (See Figure 1.7 for parameter reference). The finite-element meshes vary as the crack-front advances, leading to slight deviations in the total number of elements, degrees of freedom, and aspect ratios.

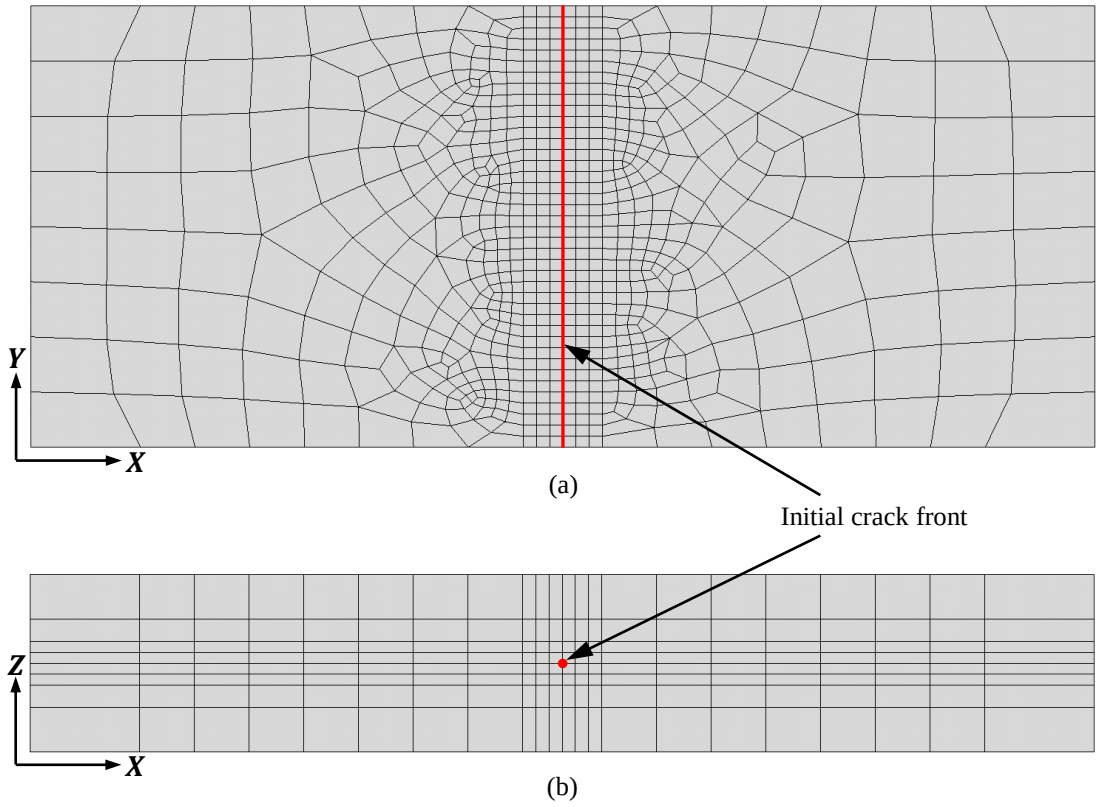

Figure 1.9. Finite-element mesh configuration for initial double cantilever beam specimen (a) top view (b) side view.

A new, stable, crack-front configuration was determined for each of the applied-displacement increments. Approximately 11 crack-front extension iterations were

required for each increment. Within each displacement increment, the crack front was re-discretized using the spline function methodology described in Section 1.3.3. As expected, the predicted crack growth was self-similar. A plot of the evolving crack-front profile is shown in Figure 1.10. The crack length remained constant along the crack front, and the results can be compared to an analytical expression from beam theory [39].

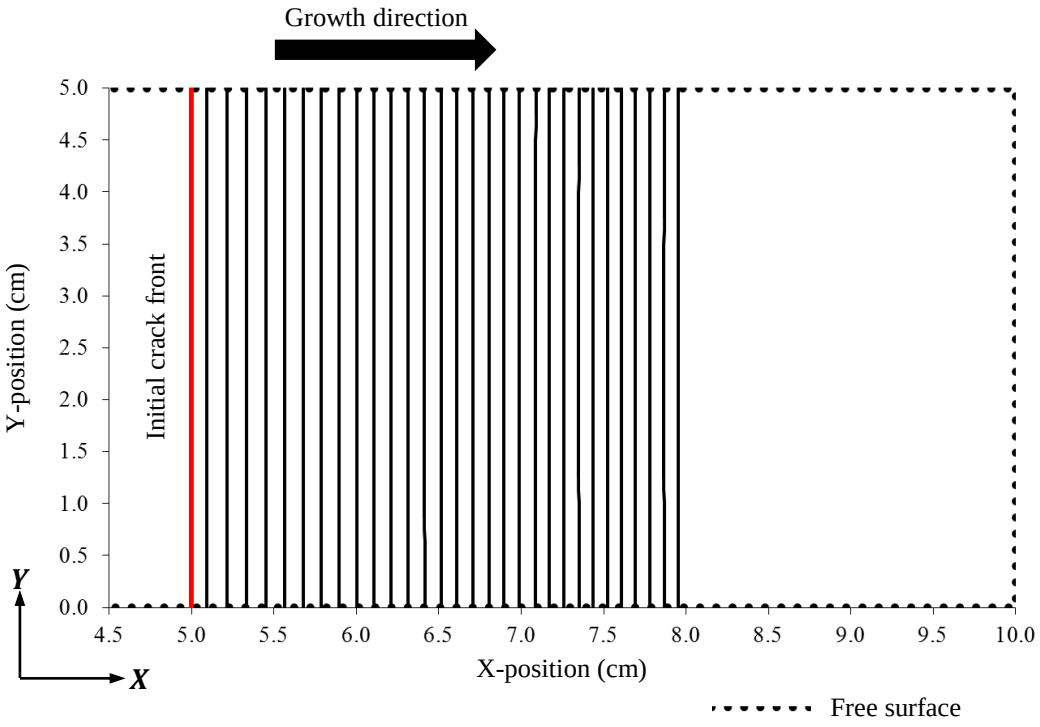

Figure 1.10. Self-similar crack-front profile evolution for DCB specimen with $\nu = 0$.

Table **1.1** summarizes the comparison between selected simulated crack lengths and those from beam theory. For all 30 increments, the average percent difference

between predicted crack lengths and beam theory crack lengths was approximately 0.5%.

Table 1.1. Summary of selected simulated crack lengths compared to analytical beam theory for a double cantilever beam specimen experiencing uniform crack growth.

Increment	Reaction Load (N)	Energy Release Rate (N/cm) Simulation Avg.	Crack Length (cm) Simulation Avg.	Crack Length (cm) Beam Theory	% Error Crack Length
1	7.679E-04	9.399E-06	5.092	5.123	0.605
6	6.971E-04	9.400E-06	5.677	5.708	0.543
11	6.430E-04	9.400E-06	6.211	6.242	0.497
16	5.999E-04	9.400E-06	6.708	6.737	0.430
21	5.642E-04	9.399E-06	7.172	7.204	0.444
26	5.343E-04	9.400E-06	7.610	7.642	0.419

1.4.2 Double cantilever beam: curvilinear growth

The initial DCB specimen geometry from Section 1.4.1 was used in the second proof-of-concept simulation; however, in this case a non-zero Poisson's ratio, $\nu = 0.3$, was used with a unit Young's modulus, $E = 1\ \mathrm{N/cm^2}$. The introduction of a non-zero Poisson's ratio creates a non-uniform energy release rate distribution along the crack front due to anticlastic curvature associated with bending [40,41]. As a result, this specimen initially experiences non-uniform growth. The same constant, local, critical energy release rate for each position, $G_{ic} = 9.4\ x\ 10^{-6}\ \mathrm{N/cm}$, was selected. The initial applied displacement was 0.100 cm, and was increased by 30 equal increments

of 0.005 cm, resulting in a final applied displacement of 0.250 cm. The crack growth for this configuration remains stable, but is expected to evolve in a curvilinear fashion.

The simulation methodology successfully predicted stable crack-front configurations for each of the applied-displacement increments. On average, 11 crack-front extension iterations were required for each increment. As in the previous DCB simulation, the updated crack fronts were re-discretized using a spline function as described in Section 1.3.3. The simulated growth initiated at the center of the crack front where geometric constraint is highest. As illustrated in Figure 1.11, the growth continued in the center as it bowed out symmetrically along the width of the crack front towards the free surfaces. Initially, the front experienced partial growth, meaning a portion of the front advanced, while other portions remained stationary. Figure 1.12 shows the finite-element meshes surrounding the first four increments of evolution that exhibit this partial growth. As the crack front moved towards the free surfaces, sections of the front evolved by different amounts, indicating non-uniform growth. However, once the curved crack front reached the free surfaces, growth continued in a uniform, self-similar fashion; the front maintained its curvature as it continued to advance stably. The general behavior predicted is comparable to observations in the literature [21,42,43].

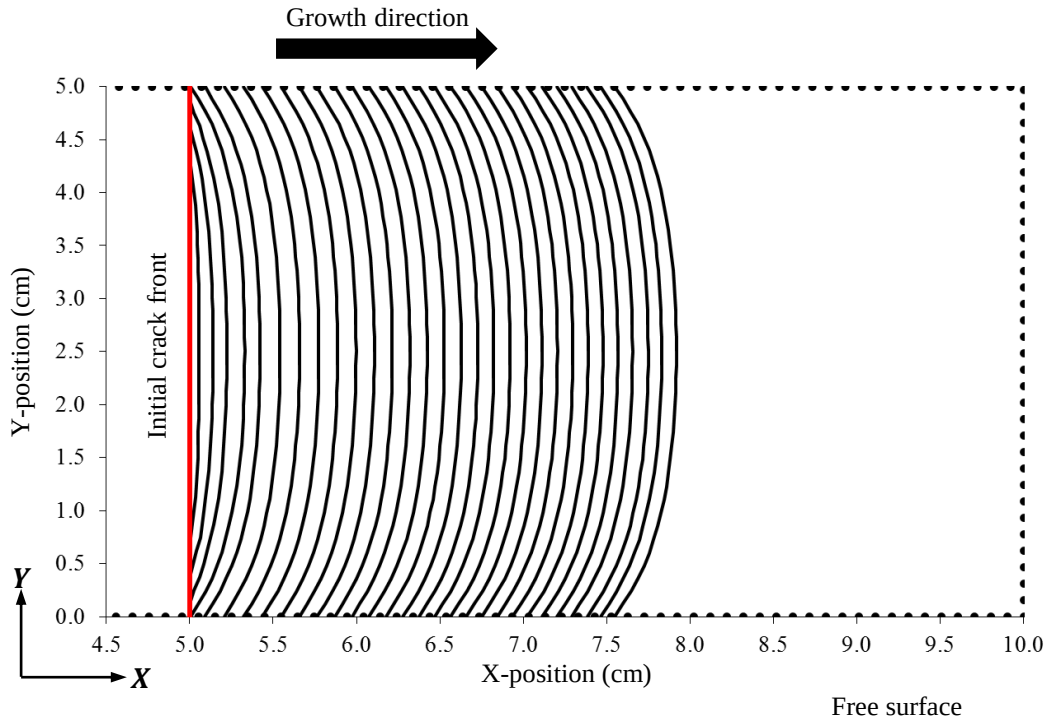

Figure 1.11. Curvilinear crack-front profile evolution for DCB specimen with $\nu = 0.3$.

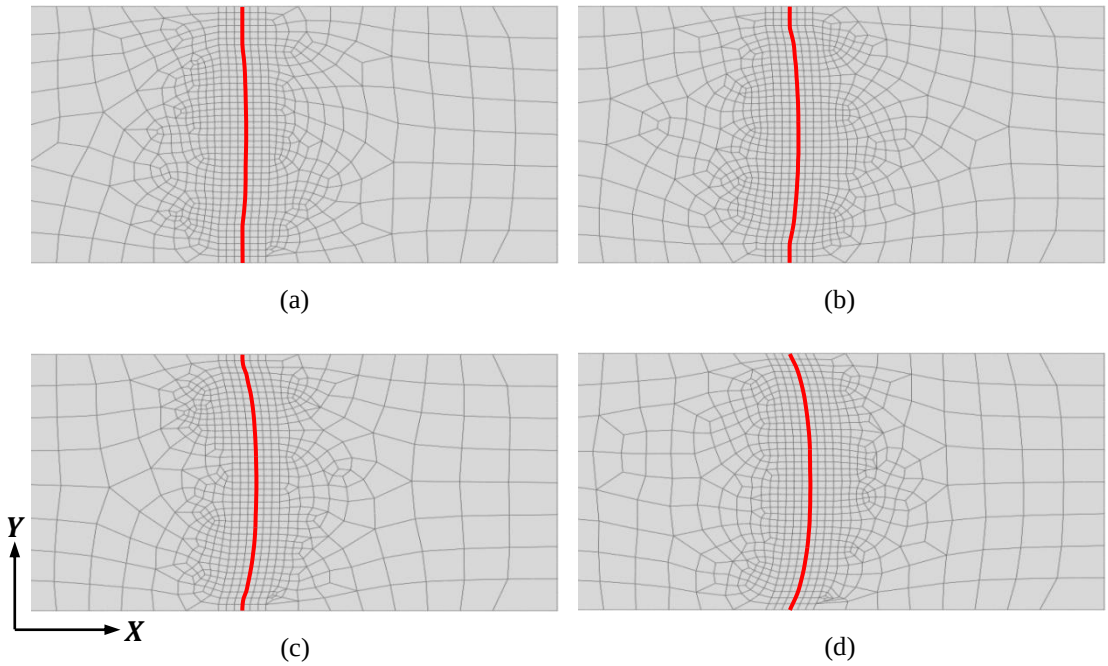

Figure 1.12. Finite-element meshes of evolving double cantilever beam specimen with $\nu = 0.3$ after crack-growth increments (a) 1, (b) 2, (c) 3 and (d) 4. The crack front is highlighted.

1.4.3 Embedded elliptical crack

The third proof-of-concept simulation, as shown in Figure 1.13, consisted of an initially elliptical crack of aspect ratio 2:1 embedded within a rectangular body. The initial minor and major radii of the crack are $a = 0.125$ cm, and $a = 0.25$ cm, respectively. Comparing the largest crack size to the overall dimensions yields the following aspect ratios, $a/H = 1/16$, and $a/L = a/W = 1/20$, which is appropriate sizing to approximate crack behavior within an infinite body. The crack faces were subjected to symmetrical point loads. An isotropic material with $E = 1.0\ x\ 10^5$ N/cm^2 and $\nu = 0.3$ was used. Similar to the previous simulations, a constant, local, critical energy release rate for each crack-front position, $G_{ic} = 2.25$ N/cm, was chosen as the failure criterion. By investigating the analytical derivative of energy release rate with respect to crack length for a penny-shaped crack subjected to equal and opposite concentrated loads [44], the expected crack growth for this configuration was also determined to be inherently stable, i.e. $dG/da < 0$. The applied load was increased over 35 increments starting at $P = 100$ N and ending at $P = 475$ N. The loading consisted of 30 increments of 10 N, followed by five increments of 15 N. The initially elliptical geometry offers an opportunity to predict partial, non-uniform growth. As in the DCB specimen in Section 1.4.2, certain portions of the embedded crack front will experience growth, while others remain stationary. Compared to the DCB specimen in Section 1.4.2, the embedded elliptical crack is expected to exhibit a more dramatic, non-uniform transition as it evolves into a circular configuration [14,45].

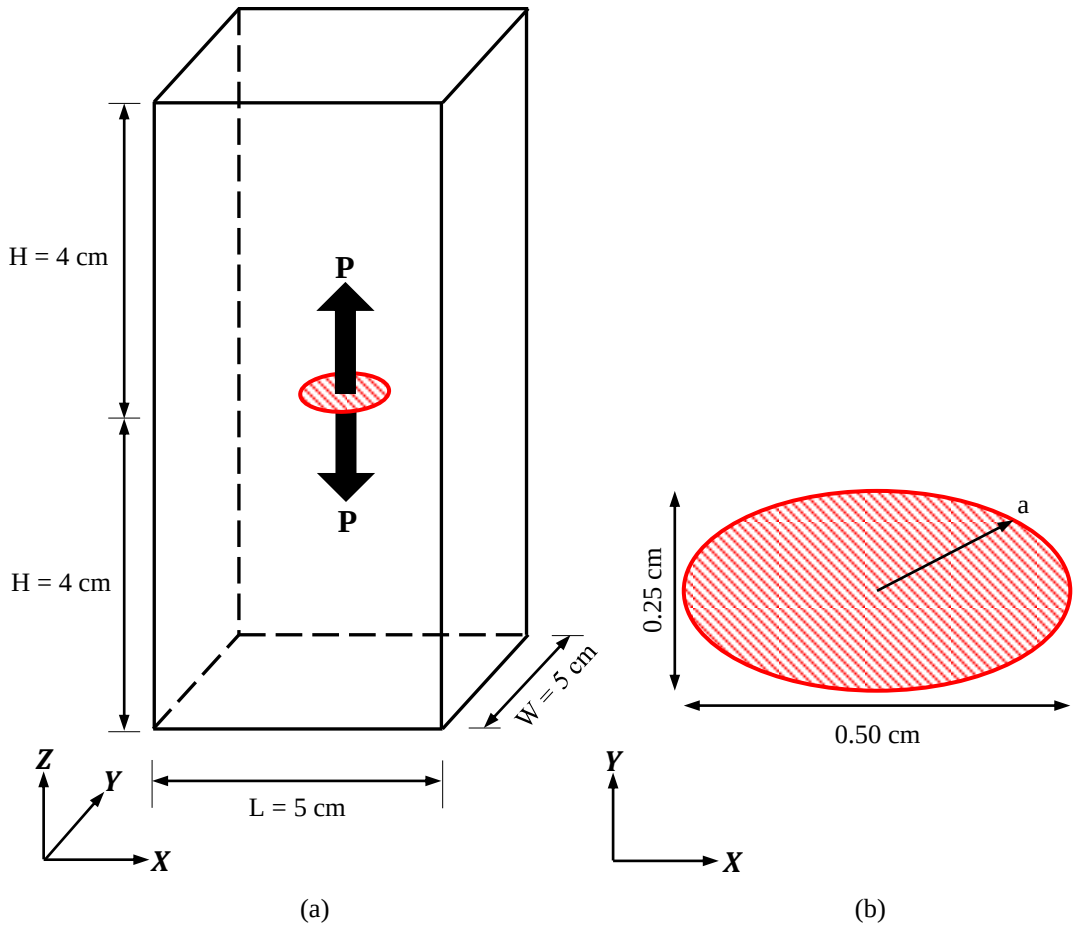

Figure 1.13. Embedded elliptical crack problem (a) geometry and boundary conditions, and (b) initial crack geometry: ellipse aspect ratio 2:1, with varying radius a.

The initial local mesh around the crack used for the embedded elliptical-crack simulation is depicted in Figure 1.14. The initial model is generated using 28,266 quadratic brick and wedge elements, with a total of 315,093 degrees of freedom. The crack front was discretized into 80 segments. The crack front was surrounded by quarter-point brick elements with initial aspect ratios at the major and minor axes described in Table 1.2. The total number of elements, total degrees of freedom, and element aspect ratios vary with the evolution of the crack front.

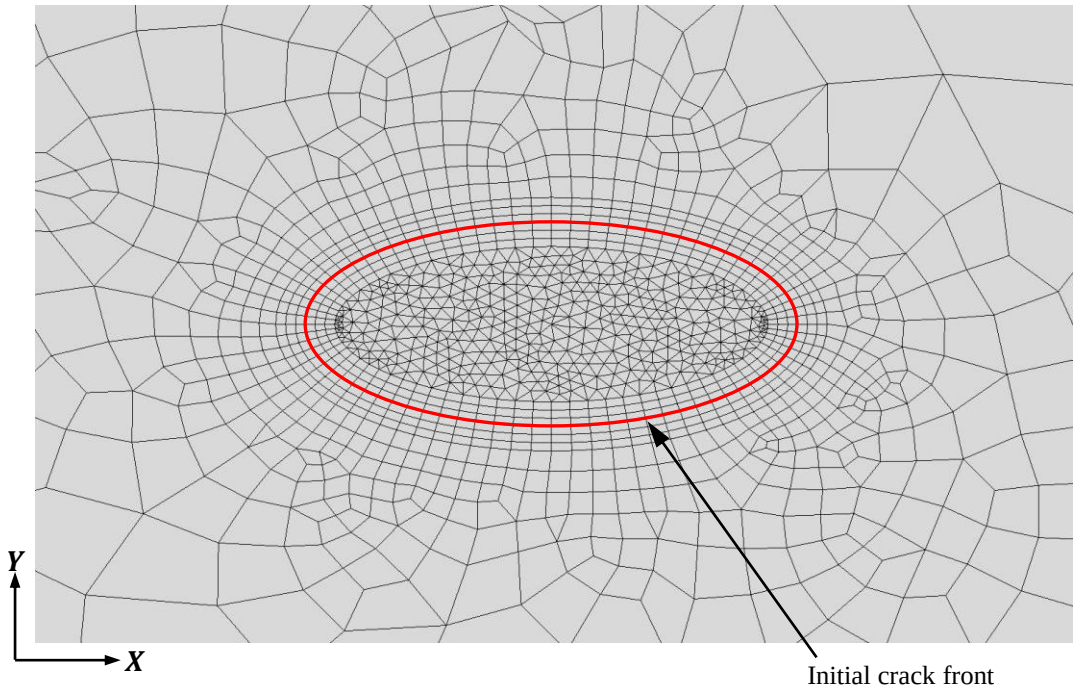

Figure 1.14. Finite-element mesh configuration for embedded, initially elliptical crack subjected to symmetric, central, crack face point loads.

Table 1.2. Initial aspect ratios of elements at the ends of the major and minor axes of the embedded elliptical crack.

Ellipse Axis	a	l/a	l/h	l/w
minor	0.125	0.08	1.00	0.510
major	0.250	0.04	1.00	1.017

The implementation of the energy-based growth method successfully predicted stable crack configurations for each load increment. On average, each increment required 5 iterations. For this simulation, augmentation to the crack front discretization, as described in Section 1.3.3, was not required. The initially elliptical crack first experienced growth near the minor axis. Figure 1.15 depicts the evolving

crack-front profile for every other load increment. The crack front continued to bow symmetrically along the minor axis, eventually evolving into a circular configuration. Figure 1.16 shows the finite-element meshes surrounding the crack front for four load increments as the shape approached a circular configuration. The simulation successfully captures the unique nature of the growth. To the best of the authors' knowledge, no experimental or numerical comparisons exist in the literature for this type of evolution. However, once the crack front reaches a circular shape, the predicted radius can be compared to an analytical expression for a penny-shaped crack subjected to equal and opposite concentrated loads [44]. After the 25^{th} load increment, a circular configuration was reached. A total of eleven uniform, concentric, circular crack-growth increments were simulated. The average percent difference between the simulated crack lengths and the analytical crack lengths was approximately 0.1%. Table 1.3 summarizes the comparison for selected increments.

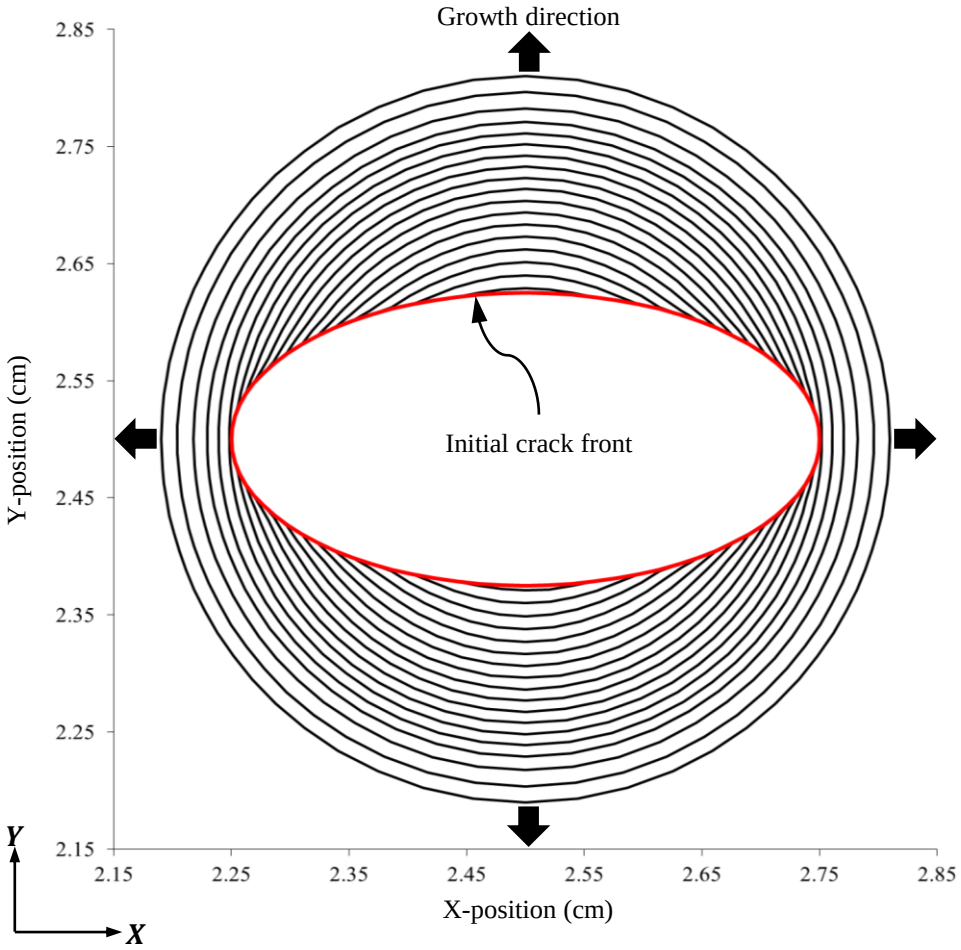

Figure 1.15. Non-uniform crack-front evolution profile for an embedded, initially elliptical crack. Every other crack-growth increment is displayed for clarity.

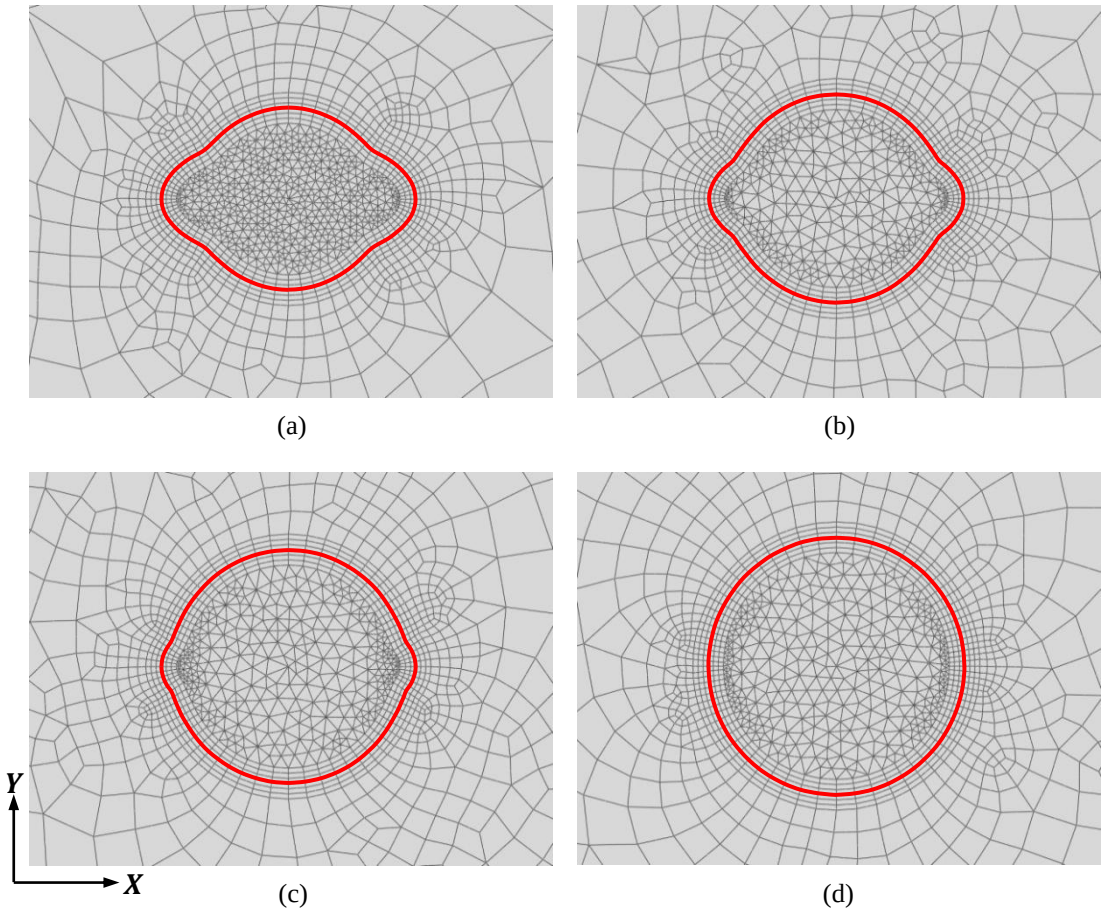

Figure 1.16. Finite-element meshes of evolving, embedded, initially elliptical crack front subject to symmetric point loads after crack-growth increment (a) 10, (b) 15, (c) 20 and (d) 25. The crack front is highlighted.

Table 1.3. Summary of selected simulated crack lengths compared to an analytical expression for a penny-shaped crack subjected to equal and opposite concentrated loads.

Increment	Applied Load (N)	Energy Release Rate (N/cm) Simulation Avg.	Crack Length (cm) Simulation Avg.	Crack Length (cm) Analytical	% Error Crack Length
25	350	2.244	0.2516	0.2519	0.119
27	370	2.250	0.2611	0.2614	0.115
29	390	2.250	0.2707	0.2707	0.000
31	415	2.250	0.2824	0.2822	0.071
33	445	2.250	0.2962	0.2956	0.203
35	475	2.250	0.3097	0.3087	0.324

1.5 Discussion

Three aspects of the newly proposed method and implementation deserve further discussion: (1) accuracy and stability, (2) computational cost, and (3) generalization.

As with any incremental-iterative approach, the new simulation technique is sensitive to the size of the applied-load increment relative to the geometry of the crack front. To avoid numerical instabilities and capture accurate growth, it is important to proportion the load-increment size to both the overall geometry and the desired discretization of the crack front. If the load increment is too large relative to a crack or the spacing of crack-front nodes, the algorithm might not reach an accurate or stable configuration. At this time, no determining factors have been identified for a critical load-increment size given a model geometry and finite-element mesh; user judgment and trial-and-error are currently employed.

Another potential concern is the perceived computational cost. Continual updating of a finite-element mesh is often regarded as arduous in the literature. However, with ever-improving automatic meshing techniques and sub-modeling approaches, the additional cost of re-meshing compared to the value gained by representing a physical feature (e.g. a crack) as an explicit part of the geometric model is minimal. Re-meshing around the geometrically explicit representation of the crack allows for the energy-based crack-growth formulation to dictate evolution, rather than relying on prescribed paths defined by the finite-element mesh, for example. Most of the computational cost in the current simulation algorithm is associated with calculating the $\frac{\delta G_i}{\delta a_j}$ influence matrix, as opposed to re-meshing. To obtain the $\frac{\delta G_i}{\delta a_j}$ influence matrix,

back solves are required with the global stiffness matrix for each crack-front node [36]. These back solves are in addition to those associated with the initial finite element analysis. For example, the embedded-elliptical crack-growth simulation, which has approximately 290,000 degrees-of-freedom and 80 crack-front nodes, requires on the order of 100 minutes (wall clock time) for an iteration to complete. Of the total wall clock time, 87% is spent extracting the $\frac{\delta G_i}{\delta a_j}$ influence matrix compared to 6% for two finite-element analyses and output extraction, 4% for the energy release rate calculations, 2.5% for data input and output, and 0.5% for the re-meshing of the updated model. The presented simulations were executed on a single node with dual quad-core Intel® Xeon(R) E5420 CPUs and 16GB of shared RAM. To accelerate the calculation and alleviate memory issues associated with the $\frac{\delta G_i}{\delta a_j}$ back solves, a standalone, sparse direct solver, MUMPS (MUltifrontal Massively Parallel sparse direct Solver), was utilized. Parallel processing schemes were not employed for the current implementation. However, the extraction of the $\frac{\delta G_i}{\delta a_j}$ influence matrix is embarrassingly parallelizable. The ability to distribute the individual back solves to multiple processors will greatly reduce computation time and effort.

Although the implementation described herein uses geometrically explicit crack fronts, it should be noted that the energy-based growth formulation described in Section 1.3 is general and not reliant on this approach. To reiterate, the three main components of the simulation technique require: (1) representation of a crack in a finite-element model, (2) energy release rate calculations, and (3) execution of the energy-based growth formulation. These components are employed independently. In

other words, the energy-based growth formulation, item (3), can be coupled with a variety of techniques for representing cracks and for calculating energy release rates, e.g. XFEM and the Virtual Crack Closure Technique (VCCT) [46,47]. For this work, an explicit crack representation was deemed more practical and the VCE method more effective for its ability to extract $\frac{\delta G_i}{\delta a_j}$ efficiently.

Finally, the scope of the current implementation is limited to planar, stable, crack-growth problems. As mentioned previously, this is not an inherent limitation of the methodology, but a simplifying restriction for development purposes. Mixed-mode planar growth can certainly be handled by the current implementation provided that an effective growth criterion is used. Opportunities exist within the formulation and simulation framework for the introduction of existing trajectory criteria based on mode-mixity or other parameters to capture non-planar crack behavior. One such possibility is a maximum energy release rate approach [48]. For each position on the front, a series of trial extensions that sweep radially along the front normal are tested to identify the direction associated with the maximum energy release rate. This direction is used accordingly within the VCE method and energy-based growth formulation to calculate non-planar extensions. The challenge with non-planar growth is the accurate tracking and representation of the evolving crack front geometry in a finite element environment. Extending the growth formulation for application to non-planar growth is the topic of Chapter 3. Restricting the current implementation to stable crack-growth problems, where the energy release rate generally decreases with increasing crack length, strengthens the assumption that a unique stable crack front configuration can be found for a given load. However, of ultimate interest is

developing a capability that can capture both stable and unstable crack-growth problems. The energy-based formulation can be generalized to capture unstable crack-growth evolution, and also be used to determine metrics for transitions from stable to unstable growth behavior. A general approach to simulate non-planar and unstable growth problems has been developed in Chapter 3 of this dissertation.

1.6 Conclusions

This chapter presented the development of a new, energy-based growth method and implementation for predicting evolution of planar, 3-D cracks in stable crack-growth situations. The energy-based approach uses a first-order expansion of the energy release rate that allows for an explicit expression for point-by-point advances along the front. The salient feature of the simulation technique is the use of the $\frac{\delta G_i}{\delta a_j}$ influence function made readily available via the VCE method. The $\frac{\delta G_i}{\delta a_j}$ influence function relates changes in applied load to changes in geometry along the crack front. Other simulation techniques lack such a mechanics-based connection, requiring user-prescribed updates along the crack front or reliance on finite-element meshes.

Three proof-of-concept simulations were shown to verify the approach. In contrast to previous crack-growth prediction methods, the current approach allows for smooth, non-uniform, arbitrary crack-front advance by:

1) calculating (rather than prescribing) the magnitude of local crack advance based on an explicit energetic expression;
2) reducing dependency of crack shape on initial finite-element meshes.

This chapter's implementation is applicable to planar growth situations, making the developed approach readily available for use in the study of delamination evolution in composite structures, for example. Future work, presented in Chapter 3, involves generalizing the algorithm to non-planar and unstable crack growth, allowing the simulation of crack-front evolution during the prelude to ultimate structural failure.

CHAPTER 2

DECOMPOSITION OF 3-D MIXED-MODE ENERGY RELEASE RATES USING THE VIRTUAL CRACK EXTENSION METHOD

2.1 Introduction

Numerous finite-element-based approaches have been developed to calculate accurately and efficiently mixed-mode linear elastic fracture mechanics parameters, e.g. the stress intensity factor and energy release rate. These methods include displacement correlation [49], crack closure integrals [50–52], modified crack closure integrals (virtual crack closure technique) [46,53], interaction integrals (M-integrals) [54–58], and J-integrals [59,60]. All of these methods have been well developed and documented throughout the literature.

Since the focus of Chapter 2 is on mixed-mode problems, the M-integral is regarded as the method of choice [57,61]. The use of this conservative interaction integral combines two solutions: the numerical finite element solution and an auxiliary solution from the crack front asymptotic expansions of field quantities. This superposition allows for the mode decomposition of the stress intensity factor. Simpler methods, such as the virtual crack closure technique (VCCT), have natural decomposition methods that arise through their implementation [47]. Other forms of mode decomposition, often applied to equivalent domain J-integral approaches, use

symmetric and anti-symmetric fields around the crack front to capture the stress intensity factor and energy release rate modes [62,63].

The virtual crack extension (VCE) method (also known as the stiffness derivative method) is another computational approach to calculate energy release rates. First introduced by Dixon and Pook [29] and Watwood [30], and further developed by Hellen [31] and Parks [32], the method uses stiffness variations to calculate energy release rates from the potential energy form. Early VCE calculations utilized finite perturbations of meshes to approximate the required stiffness derivatives. This finite difference approach often introduced geometric approximation and numerical truncation errors. Accuracy was highly sensitive to perturbation size relative to the finite element mesh. Through applications of variational principle theory, a direct-integration approach simplified the VCE method and improved efficiency [33–35]. The variational approach eliminated the need for finite perturbations and also allowed for the calculation of higher order derivatives of energy release rates. Hwang *et al.* [36], utilized the formulation of [34], and generalized the technique for planar 3-D cracks.

Several methods have been proposed to decompose energy release rates via the VCE method. Previous work in two-dimensions attempted to draw concepts used in the decomposition of the J-integral by employing a complex variable J_1 and J_2 approach [64]. This technique yielded satisfactory results as long as mode II was not dominant. Lin and Abel [34] proposed a general method using Betti's reciprocal theorem and Yau's [8] mutual energy representation. Haber and Koh [33] used a similar approach that combined calculated displacement fields with analytic solutions

for pure mode I and pure mode II behavior. Ishikawa [62] demonstrated a 2-D VCE mode decomposition that successfully employed the symmetric/anti-symmetric field methodology. This technique was extended to 3-D for the equivalent domain J-integral [63,65,66], and identified by Hwang *et al.* [36] as a feasible 3-D mode decomposition approach for the VCE method.

A salient feature of the VCE method is its additional ability to extract the variations of energy release rate with respect to crack advance. These rates of energy release rate make the VCE method attractive for crack growth predictions and simulations, as demonstrated in Chapter 1 [67]. The rate of energy release rate provides a mechanics-based relationship between global energy change and local crack extensions along the front. This parameter can be used as an influence function allowing for explicit calculations of crack advances rather than relying on user-prescribed extension increment methods. The rate of energy release rate is also valuable as a metric for determining crack growth stability. Until now, a 3-D *mixed-mode* VCE calculation has not been developed. Such a capability will allow for the VCE method to be used within 3-D arbitrary crack growth simulations that might require non-planar crack growth and mixed-mode growth criteria. The current VCE implementation, discussed herein, uses virtual crack extensions that remain in the crack plane. This is not a limitation of the method. Adjustments to the virtual extension directions are easily made, allowing for out-of-plane energy release rate calculations. This facilitates using a trajectory criteria based on the maximum energy release rate [48,68] to predict non-planar crack growth, to be shown in Chapter 3.

The objective of this chapter is to extend the mode I formulation developed by Hwang *et al.* [36] to a general, fully 3-D, mixed-mode energy release rate approach. The implementation presented herein follows the symmetric/anti-symmetric field decomposition of Nikishkov [63], and the 2-D VCE method of Ishikawa [62]. Expanding the VCE global energy release rate form to extract the mixed-mode contributions reveals the presence of unique and previously unexplored modal-interaction coupling terms. The significance of these terms and their relation to the mixed-mode energy release rates must be considered. The scope of Chapter 2 focuses on the computation of the energy release rate and its mode decomposition. The decomposition of mixed-mode variations of energy release rates will be proposed, but was not implemented due to its high computational cost. At this point, the mixed-mode values of the variation of energy release rate have little perceived value in crack growth simulations (in contrast to the total variation of energy release rate [67]), but remain an area of interest in ongoing research.

The next section will introduce the VCE method. A symmetric/anti-symmetric formulation for decomposing 3-D, mixed-mode displacement fields will be presented. The decomposed displacement fields are substituted into the VCE method to derive the expressions for the 3-D, mixed-mode energy release rates. The following sections will discuss the implementation of the mode decomposition method and provide numerical examples. Mixed-mode crack loading configurations in isotropic and orthotropic materials will be presented. VCE energy release rate results will be compared to analytic and M-integral approaches.

2.2 3-D Mixed-mode virtual crack extension method

This section offers a brief summary of the VCE method. The 3-D planar formulation is extended to construct the new expressions for the mixed-mode energy release rates and rates of energy release rates. A more detailed formulation and discussion of the general VCE method can be found in [34–36].

2.2.1 Virtual crack extension formulation

The VCE method is derived from the expression for the potential energy, Π, of a finite element system:

$$\Pi = \frac{1}{2}u^T K u - u^T f, \tag{2.1}$$

where u, K, and f are the displacement vector, the stiffness matrix, and the applied force vector, respectively.

The energy release rate, G, at crack-front position i is defined as the negative variation of the potential energy with respect to a virtual, incremental, crack-front extension, δa, in the normal direction of the front at that position:

$$G_i \equiv -\frac{\delta \Pi}{\delta A_i} = -\frac{\delta \Pi}{\delta a_i \ell_i}. \tag{2.2}$$

In the 3-D sense, the virtual extension has an associated area, δA_i, comprised of a virtual extension, δa_i, and an effective width, ℓ_i. Applying the variation to the finite element expression for potential energy leads to the following form of the energy release rate:

$$G_i = -\frac{1}{\ell_i}\left(\frac{1}{2}\frac{\delta u}{\delta a_i}^T Ku + \frac{1}{2}u^T\frac{\delta K}{\delta a_i}u + \frac{1}{2}u^T K\frac{\delta u}{\delta a_i} - \frac{\delta u}{\delta a_i}^T f - u^T\frac{\delta f}{\delta a_i}\right). \tag{2.3}$$

Grouping like terms leads to:

$$G_i = -\frac{1}{\ell_i}\left(\frac{\delta u}{\delta a_i}^T (Ku - f) + \frac{1}{2}u^T\frac{\delta K}{\delta a_i}u - u^T\frac{\delta f}{\delta a_i}\right). \tag{2.4}$$

By maintaining finite element equilibrium, such that $Ku - f = 0$, the expression for energy release rate becomes:

$$G_i = -\frac{1}{\ell_i}\left(\frac{1}{2}u^T\frac{\delta K}{\delta a_i}u - u^T\frac{\delta f}{\delta a_i}\right). \tag{2.5}$$

For simplicity in the current implementation, it is assumed that applied forces, f, are not influenced by the virtual incremental extension, and therefore the variational force term, $\frac{\delta f}{\delta a_i}$, is zero. This simplification reduces Eq. (2.5) to:

$$G_i = -\frac{1}{\ell_i}\left(\frac{1}{2}u^T \frac{\delta K}{\delta a_i} u\right). \tag{2.6}$$

Note, if the virtual extensions alter the nature of the applied load (e.g. with crack-face pressures, thermal, and body-force loadings), the effect must be accounted for with the variational force term, $\frac{\delta f}{\delta a_i}$, and included throughout the formulation. Non-zero contributions to the stiffness variations only occur over elements that experience the virtual extensions. This simplifies calculations and the implementation of the method.

The expression for the first-order variation of the energy release rate with respect to incremental crack extension, δa_j, follows from Eq. (2.6):

$$\frac{\delta G_i}{\delta a_j} = -\frac{1}{\ell_i}\left(u^T \frac{\delta K}{\delta a_i}\frac{\delta u}{\delta a_j} + \frac{1}{2}u^T \frac{\delta^2 K}{\delta a_i \delta a_j} u\right). \tag{2.7}$$

Note that Eqs. (2.6) and (2.7) represent the total global formulations of the VCE expressions for the energy release rate and rate of energy release rate. The integration within the domain surrounding the crack front and the corresponding calculations are performed in a global coordinate system.

2.2.2 Mixed-mode displacement decomposition

In the VCE method, the primary finite element field of interest is displacement. As a result, to calculate mixed-mode energy release rates, the displacements near the crack front involved in the numerical integration domain must be decomposed into

mode I, II and III components. Unlike the VCCT method that relies on calculations at and behind the crack front, the VCE technique uses a local volume that encompasses the entirety of the crack front to obtain energy release rates.

The displacement decomposition technique can easily be applied for a straight, uniform crack front. However, for an arbitrary front, the use of a local crack-front coordinate system is required, as shown in Figure 2.1. A point-by-point coordinate transformation is employed to establish a local orientation for a position near the front.

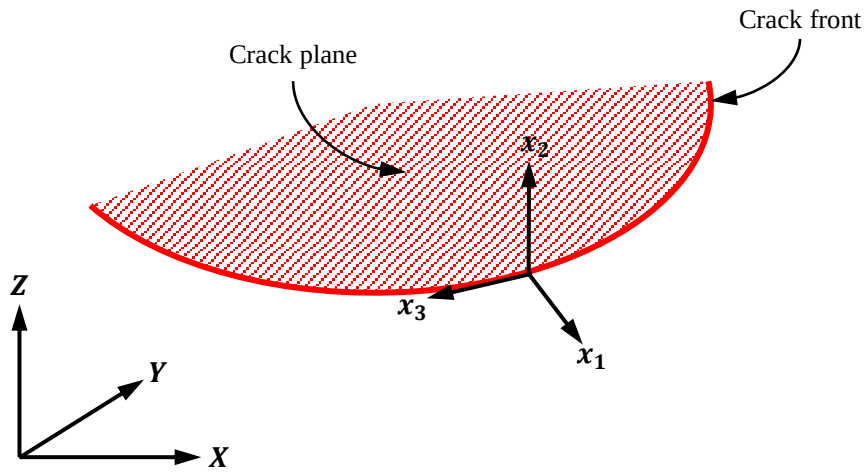

Figure 2.1. Local crack front coordinate system, x_1, x_2, x_3 for an arbitrarily shaped crack front in a global coordinate system X, Y, Z.

To determine the mixed-mode displacement contributions at a point $P(x_1, x_2, x_3)$ within the integration domain, the displacements at the mirrored point across the crack plane, $P'(x_1, -x_2, x_3)$, are required. Point P' is symmetric across the crack plane from point P, as shown in Figure 2.2. The displacements in the local coordinate system at point P, $u(u_1, u_2, u_3)$, and at point P', $u'(u_1', u_2', u_3')$, are used in the

following symmetric/anti-symmetric expressions for the mixed-mode displacement components at point P [63]:

$$u_I = \frac{1}{2}\begin{Bmatrix} u_1 + u_1' \\ u_2 - u_2' \\ u_3 + u_3' \end{Bmatrix}, \tag{2.8}$$

$$u_{II} = \frac{1}{2}\begin{Bmatrix} u_1 - u_1' \\ u_2 + u_2' \\ 0 \end{Bmatrix}, \tag{2.9}$$

$$u_{III} = \frac{1}{2}\begin{Bmatrix} 0 \\ 0 \\ u_3 - u_3' \end{Bmatrix}. \tag{2.10}$$

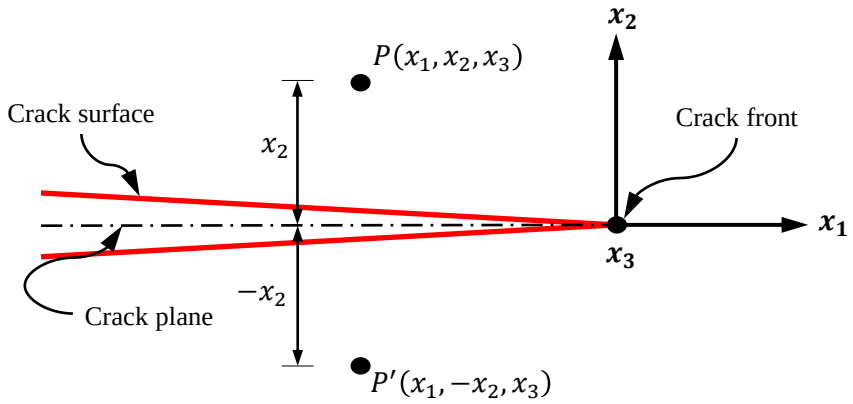

Figure 2.2. Symmetric points P and P' about the crack plane used to decompose mixed-mode displacement components.

The local displacement-mode decomposition denoted in Eqs. (2.8) – (2.10) satisfies the following summation:

$$u = u_I + u_{II} + u_{III}. \tag{2.11}$$

The decomposed displacements for all nodes surrounding the crack front in the integration domain are used in the VCE formulation to calculate mixed-mode energy release rates.

2.2.3 3-D Mixed-mode energy release rates

The global expressions for energy release rate and rate of energy release rate are modified to obtain their respective decomposed modes. Substituting Eq. (2.11) into Eq. (2.6) yields the following expression for the total energy release rate:

$$G_i = -\frac{1}{\ell_i}\left[\frac{1}{2}(u_I + u_{II} + u_{III})^T \frac{\delta K}{\delta a_i}_L (u_I + u_{II} + u_{III})\right]. \tag{2.12}$$

Note that the stiffness derivative is calculated in the local crack-front coordinate system, and is denoted by the subscript L. As mentioned in Section 2.2.2, the displacements u_I, u_{II} and u_{III} are also in the local coordinate system. Expanding Eq. (2.12) leads to the separation of the decomposed energy release rate modes:

$$G_i = -\frac{1}{\ell_i}\left[\left(\frac{1}{2}{u_I}^T \frac{\delta K}{\delta a_{i_L}} u_I\right) + \left(\frac{1}{2}{u_{II}}^T \frac{\delta K}{\delta a_{i_L}} u_{II}\right) + \left(\frac{1}{2}{u_{III}}^T \frac{\delta K}{\delta a_{i_L}} u_{III}\right) + \left({u_I}^T \frac{\delta K}{\delta a_{i_L}} u_{II}\right) + \left({u_{II}}^T \frac{\delta K}{\delta a_{i_L}} u_{III}\right) + \left(\frac{1}{2}{u_{III}}^T \frac{\delta K}{\delta a_{i_L}} u_I\right)\right]. \tag{2.13}$$

Extending from Ishikawa's 2-D VCE mode decomposition [62], the mode I and II energy release rates are as follows:

$$G_{I_i} = -\frac{1}{\ell_i}\left(\frac{1}{2}{u_I}^T \frac{\delta K}{\delta a_{i_L}} u_I\right), \tag{2.14}$$

$$G_{II_i} = -\frac{1}{\ell_i}\left(\frac{1}{2}{u_{II}}^T \frac{\delta K}{\delta a_{i_L}} u_{II}\right). \tag{2.15}$$

The unique contribution of the current derivation is the computation of the mode III energy release rate distribution along the crack front. The remaining terms in Eq. (2.13), excluding Eqs. (2.14) and (2.15), comprise a pure mode III component, $\frac{1}{2}{u_{III}}^T \frac{\delta K}{\delta a_{i_L}} u_{III}$, and three modal-interaction coupling terms. Understanding the influence of the coupling-mode terms is critical in determining their respective contributions to the 3-D mixed-mode energy release rates. Consider the following coupling mode terms from Eq. (2.13):

$$G_{I/II_i} = -\frac{1}{\ell_i}\left({u_I}^T \frac{\delta K}{\delta a_{i_L}} u_{II}\right), \tag{2.16}$$

$$G_{II/III_i} = -\frac{1}{\ell_i}\left(u_{II}{}^T \frac{\delta K}{\delta a_{i_L}}\, u_{III}\right), \tag{2.17}$$

$$G_{III/I_i} = -\frac{1}{\ell_i}\left(u_{III}{}^T \frac{\delta K}{\delta a_{i_L}}\, u_I\right). \tag{2.18}$$

In Eq. (2.16), mode I and mode II displacements are coupled. The mode I displacements are symmetric about the crack plane, while the mode II displacements are anti-symmetric about the crack plane, as discussed in Section 2.2.2. When calculating G_{I/II_i} over a symmetric domain around the crack front, the contribution from the symmetric mode I displacements will have the same sign above and below the crack plane. However, the anti-symmetric mode II displacements will have opposite signs above and below the crack plane. Since the domain is also symmetric above and below the crack plane, integrating the mode I and mode II coupling term will lead to a cancellation between the volume above and the volume below the plane. The result is $G_{I/II_i} = 0$.

The same argument can be applied to the G_{III/I_i} coupling term expressed in Eq. (2.18). The symmetric mode I displacements, and the anti-symmetric mode III displacements relative to the crack plane negate each other when integrating around the symmetric crack-front domain. This leads to the same result for the mode III and mode I coupling term, $G_{III/I_i} = 0$.

However, in Eq. (2.17) mode II and mode III displacements are coupled to determine G_{II/III_i}. In this case, both displacements involved are anti-symmetric

relative to the crack plane. With both displacement terms having opposite signed contributions above and below the crack plane, integrating around the symmetric crack front domain will lead to an additive result rather than a cancellation, i.e. $G_{II/III_i} \neq 0$. A more rigorous analytical exercise to demonstrate the symmetric relationship and resulting cancellation/additive effects of integrating the coupling terms is shown in Appendix A.

Expanding the variation of stiffness within Eq. (2.17) yields an expression of G_{II/III_i} in terms of strains, and virtual strain rates. The only contributing non-zero components of these terms to G_{II/III_i} are out-of-plane shear. Therefore, any addition to the total energy release rate from G_{II/III_i} must be a factor of the out-of-plane mode III energy release rate:

$$G_{III_i} = -\frac{1}{\ell_i}\left(\frac{1}{2}{u_{III}}^T \frac{\delta K}{\delta a_{i_L}} u_{III}\right) + G_{II/III_i}. \tag{2.19}$$

The supporting expansion and derivation showing the non-zero contribution of the G_{II/III_i} coupling term to the overall mode III energy release rate is found in Appendix B.

With the individual mixed-mode terms determined and the modal-interaction coupling terms accounted for, the VCE total energy release is successfully decomposed, satisfying the following summation:

$$G_i = G_{I_i} + G_{II_i} + G_{III_i}. \tag{2.20}$$

Note that this mixed-mode decomposition relies on the symmetries and anti-symmetries of the near-crack front displacements, which are a product of both the local crack geometry and the material composition. Consequently, the technique cannot be used to calculate mixed-mode energy release rates for a bi-material interface crack, except for special cases where the symmetry conditions are satisfied, i.e. identical materials on either side of the interface. In practice, this mixed-mode VCE formulation is limited to single homogenous materials, either isotropic or generally anisotropic, where the crack plane coincides with the material symmetry.

2.2.4 3-D Mixed-mode rates of energy release rate

A similar approach is followed to form the mixed-mode, rates of energy release rates. Taking the variation of Eq. (2.13), with consideration of the zero and non-zero coupling term contributions, the total variation of energy release rate can be expressed as:

$$\begin{aligned}\frac{\delta G_i}{\delta a_j} = -\frac{1}{\ell_i}\Bigg[&\left(u_I{}^T \frac{\delta K}{\delta a_{i_L}} \frac{\delta u_I}{\delta a_{j_L}} + \frac{1}{2} u_I{}^T \frac{\delta^2 K}{\delta a_i \delta a_{j_L}} u_I\right) + \\ &\left(u_{II}{}^T \frac{\delta K}{\delta a_{i_L}} \frac{\delta u_{II}}{\delta a_{j_L}} + \frac{1}{2} u_{II}{}^T \frac{\delta^2 K}{\delta a_i \delta a_{j_L}} u_{II}\right) + \\ &\left(u_{III}{}^T \frac{\delta K}{\delta a_{i_L}} \frac{\delta u_{III}}{\delta a_{j_L}} + \frac{1}{2} u_{III}{}^T \frac{\delta^2 K}{\delta a_i \delta a_{j_L}} u_{III}\right) + \\ &\left(u_{II}{}^T \frac{\delta K}{\delta a_{i_L}} \frac{\delta u_{III}}{\delta a_{j_L}} + u_{II}{}^T \frac{\delta^2 K}{\delta a_i \delta a_{j_L}} u_{III} + \frac{\delta u_{II}}{\delta a_{j_L}}{}^T \frac{\delta K}{\delta a_{i_L}} u_{III}\right)\Bigg].\end{aligned} \tag{2.21}$$

Separating the different contributions yields the expressions for mode I, II and III rates of energy release rate:

$$\frac{\delta G_i}{\delta a_{j_I}} = -\frac{1}{\ell_i}\left({u_I}^T \frac{\delta K}{\delta a_{i_L}} \frac{\delta u_I}{\delta a_{j_L}} + \frac{1}{2} {u_I}^T \frac{\delta^2 K}{\delta a_i \delta a_{j_L}} u_I \right), \tag{2.22}$$

$$\frac{\delta G_i}{\delta a_{j_{II}}} = -\frac{1}{\ell_i}\left({u_{II}}^T \frac{\delta K}{\delta a_{i_L}} \frac{\delta u_{II}}{\delta a_{j\ L}} + \frac{1}{2} {u_{II}}^T \frac{\delta^2 K}{\delta a_i \delta a_{j_L}} u_{II} \right), \tag{2.23}$$

$$\begin{aligned} \frac{\delta G_i}{\delta a_{j_{III}}} = -\frac{1}{\ell_i}\Bigg[& \left({u_{III}}^T \frac{\delta K}{\delta a_{i_L}} \frac{\delta u_{III}}{\delta a_{j\ L}} + \frac{1}{2} {u_{III}}^T \frac{\delta^2 K}{\delta a_i \delta a_{j_L}} u_{III} \right) + \\ & \left({u_{II}}^T \frac{\delta K}{\delta a_{i_L}} \frac{\delta u_{III}}{\delta a_{j\ L}} + {u_{II}}^T \frac{\delta^2 K}{\delta a_i \delta a_{j_L}} u_{III} + \frac{\delta {u_{II}}^T}{\delta a_{j\ L}} \frac{\delta K}{\delta a_{i_L}} u_{III} \right) \Bigg]. \end{aligned} \tag{2.24}$$

Note that the parameters involved in the mixed-mode rate of energy release rate formulations include local decomposed displacements, local first and second order stiffness derivatives, and local decomposed variations in displacements. As mentioned previously, the mixed-mode rates of energy release rates are computationally intensive. The overwhelming computational cost lies in the extraction of the $\frac{\delta u_I}{\delta a_{j_L}}$, $\frac{\delta u_{II}}{\delta a_{j\ L}}$, and $\frac{\delta u_{III}}{\delta a_{j\ L}}$ paremeters, which requires that all nodal displacements and element stiffness's be transformed into a local coordinate system followed by a back-solve for each position along the crack front. Currently, the *mixed-mode* variations of energy release rates, unlike the *total* variation of energy release rate, have unknown

significance in crack growth simulation techniques and are not part of this chapter's scope. However, from a theoretical fracture mechanics perspective, the mixed-mode rates of energy release rates remain an interesting concept with potential future applications.

2.3 Numerical Implementation

The current mixed-mode VCE implementation relies on the use of a local crack-front element template to surround a geometrically explicit crack representation. The symmetric arrangement of elements encompassing the crack front facilitates the use of the mixed-mode decomposition formulation presented in Section 2.2.2. Two example templates are shown in Figure 2.3. Decomposed displacements are obtained, according to the method described in Section 2.2.2, for each node of the elements involved in the VCE integration scheme. Points P and P' can be directly identified with the symmetric crack-front mesh, avoiding the need to interpolate displacements required in the decomposition procedure. A template of well-organized elements along the crack front also improves integration schemes and accuracy of fracture mechanics calculations. The added value of implementing and maintaining a crack-front template exceeds the associated meshing effort.

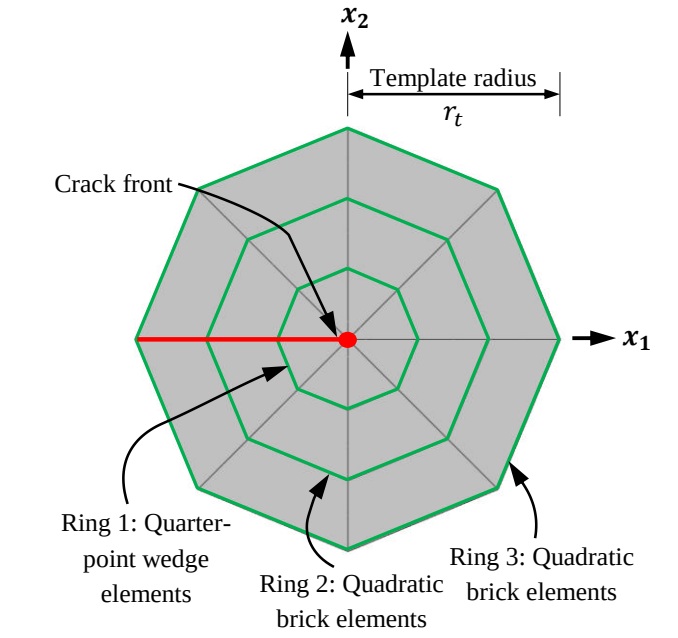

(a)

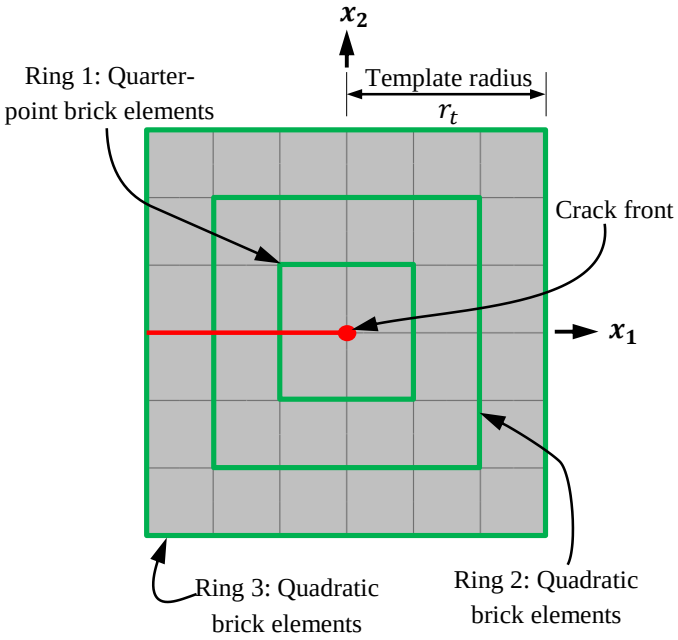

(b)

Figure 2.3. Crack-front template structure for (a) FRANC3D rosette mesh and (b) in-house square-ring composite laminate mesh.

The crack-front templates used employ serendipity quarter-point elements to reproduce the theoretical square-root-singular fields near the crack front [69,70]. Figure 2.4 shows a schematic of a 20-noded brick and 15-noded wedge element with dimension parameters that will be referenced in the numerical examples of Section 2.4. Each template also has a characteristic template radius, serving as a refinement control, to be sized appropriately relative to the crack geometry and overall model geometry.

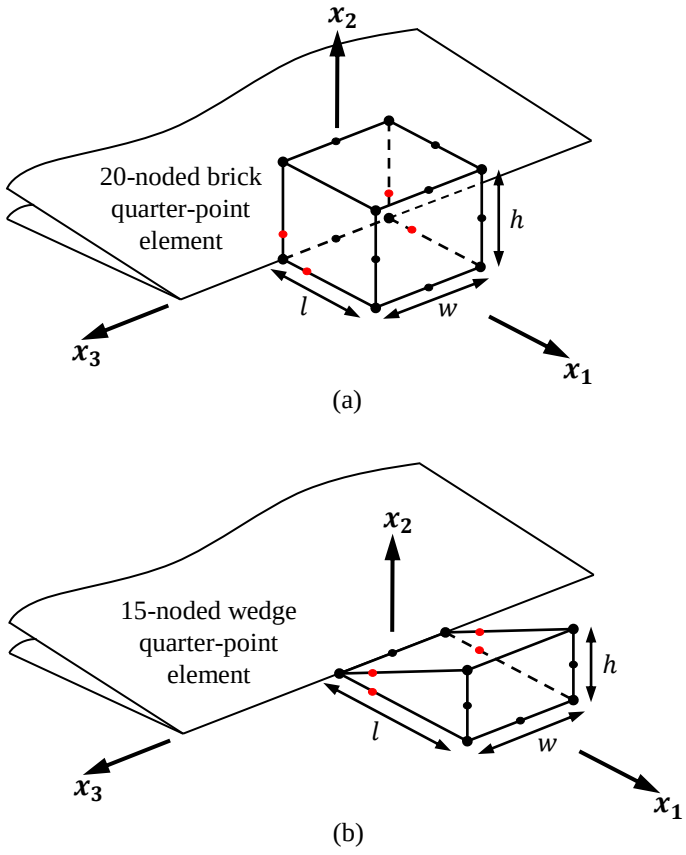

Figure 2.4. Schematics of crack-front quarter-point elements (a) 20-noded brick and (b) 15-noded wedge.

The current implementation uses two types of templates. The first template and the rest of the volume mesh is generated by the FRANC3D 6.0.5 software [71]. The FRANC3D template, as shown in Figure 2.3a, encompasses the crack front with a ring of eight, 15-noded quarter-point wedge elements. A user-controlled number of standard 20-noded, quadratic, brick element-rings encircle the quarter-point ring, creating a rosette template. The FRANC3D meshing capability can be applied to arbitrary crack geometries.

The second template, produced by an in-house software package, is designed to model delaminations, i.e. planar cracks at layer interfaces in composite laminates. The general mesh generation scheme uses a layered approach to homogenize lamina that can then be assigned orthotropic material properties as well as an orientation. The crack front template, as shown in Figure 2.3b, consists of three square rings of elements surrounding the front. The four inner-ring elements, immediately neighboring the crack front, are 20-noded, quarter-point, brick elements. Standard quadratic, brick elements comprise the outer two insulating rings.

With a well-formed crack representation and finite element mesh, the discretized models are solved using ABAQUS/Standard 6.11-1 [72] commercial software. The converged finite element results and necessary crack front information are forwarded to a standalone, mixed-mode VCE post-processor where the fracture mechanics calculations are executed. The current VCE implementation can calculate energy release rates at both corner and midside node positions along the crack front. The selection of corner or midside nodes alters the profile of the virtual extensions used in the calculations, the former being linear and the latter quadratic. A preliminary

investigation revealed that energy release rate calculations at corner nodes outperformed midside nodes, confirming observations made in the literature for similar methods [73].

The current VCE implementation enables numerical integration schemes over one or two rings of template elements. The single ring of integration comprises only the quarter-point elements. The second ring of integration includes both the quarter-point elements and the next layer of surrounding brick elements. Applying the virtual extensions over the second ring of elements improves energy release rate results by effectively shifting the area of high virtual strain caused by the virtual extensions away from the singular elements, to elements where field gradients are not as severe. In this case, the singular elements encompassing the crack front experience negligible virtual strain, and the bulk of the virtual strain is moved outwards to the second ring. Others [58,61] have demonstrated the increase in fracture parameter accuracy with the M-integral approach when using multiple rings of elements. It was observed in this work that using the second ring of integration within the VCE method is more effective when calculating variations of energy release rate compared to energy release rates.

Herein, the VCE results for energy release rates were obtained at corner-node positions along the crack front using virtual extensions in the crack plane. Since the scope of this chapter is concerned with energy release rate calculations, a single ring of numerical integration (quarter-point crack-front elements only) was deemed sufficiently accurate.

For comparison, M-integral calculations were performed using the FRANC3D software. With FRANC3D, the M-integral approach using appropriate mesh densities

for engineering applications has been shown to be accurate to within 1% of expected solutions [58]. For the following comparisons, the stress intensity factors were calculated at midside nodes along the crack front. The subsequent expression relates total energy release rate, G, to the mixed-mode stress intensity factors under linear elastic fracture mechanics assumptions [74]:

$$G = \frac{K_I^2}{E'} + \frac{K_{II}^2}{E'} + \frac{K_{III}^2}{2\mu}, \tag{2.25}$$

where $E' = E$ for plane stress, $E' = E/(1-\nu^2)$ for plane strain, and $\mu = E/\big(2(1+\nu)\big)$ is the shear modulus. Eq. (2.25) was used to convert M-integral stress intensity factor results to mixed-mode energy release rates for comparison with the current VCE approach.

2.4 Numerical examples

In this section, five verification analyses are presented to demonstrate the accuracy of the new, 3-D, mixed-mode energy release rate implementation using the VCE method (four in Subsections 2.4.1 and 2.4.2 and one in Subsection 2.4.3). The examples also highlight the impact and variability of the coupling terms for a range of mode-mixity conditions. The mixed-mode VCE results are compared with analytical and M-integral methods, as well as published results from the literature. To obtain a

direct relative percent difference between the VCE and M-integral methods, the corner node VCE results are linearly interpolated to midside positions. The point-by-point differences are normalized by the average total energy release rate of the reference solution (i.e. the analytic or M-integral approach).

Section 2.4.1 describes four isotropic numerical examples by presenting the model geometries, material properties, and finite element details. Table 2.1 summarizes the pertinent model information, including mode-mixity, material properties, number of elements and degrees-of-freedom (DOF), and crack-front discretization information (i.e. template radius, and ratio of crack-front element length to crack length). Each model in Section 2.4.1 was meshed using the FRANC3D software. The resulting templates consisted of three rings of elements. Section 2.4.2 reports the mixed-mode energy release rate results and numerical comparison to reference solutions for the examples described in Section 2.4.1. Section 2.4.3 demonstrates the capability of the VCE method to extract mixed-mode energy release rates along a delamination front in an orthotropic unidirectional composite laminate. Figures depicting the finite element meshes for the numerical examples can be found in Appendix C.

Table 2.1. Summary of isotropic numerical examples: model description and crack-front information. See Figure 2.3 and Figure 2.4 for crack front template parameter reference.

Numerical Example	Mode-Mixity	Material Properties		Model Description		Crack Front Template		
		E (GPa)	ν	No. of Elements	No. of DOF	r_t (mm)	Segments	l/a
Inclined Penny Crack	I/II/III	0.100	0.00	139,083	638,181	0.125	96	0.033
Arcan Specimen	I/II	71.4	0.33	20,944	106,227	0.127	26	0.007
Angled-Crack 3-Point Bend	I/III	70.6	0.33	133,391	644,070	0.500	70	0.008
Surface-Cracked Cylinder	II/III	206	0.30	62,243	322,071	0.200	82	0.017

2.4.1 Isotropic numerical examples

The first problem considered a 45°-inclined circular crack centrally embedded within a rectangular body, as shown in Figure 2.5. The overall model geometry was sized with appropriate aspect ratios to approximate crack behavior within an infinite body. Analytical expressions for the mixed-mode stress intensity factors for an inclined penny crack under remote tension [75] are used as a reference solution:

$$K_I = \sigma sin^2(\gamma)\sqrt{\pi a}(2/\pi), \tag{2.26}$$

$$K_{II} = \sigma sin(\gamma)cos(\gamma)\sin(\theta)\sqrt{\pi a}(2/\pi)\left(\frac{2}{2-\nu}\right), \tag{2.27}$$

$$K_{III} = \sigma sin(\gamma)cos(\gamma)\cos(\theta)\sqrt{\pi a}(2/\pi)\left(\frac{2(1-\nu)}{2-\nu}\right), \tag{2.28}$$

where γ is the angle of inclination, and θ is the position along the crack front.

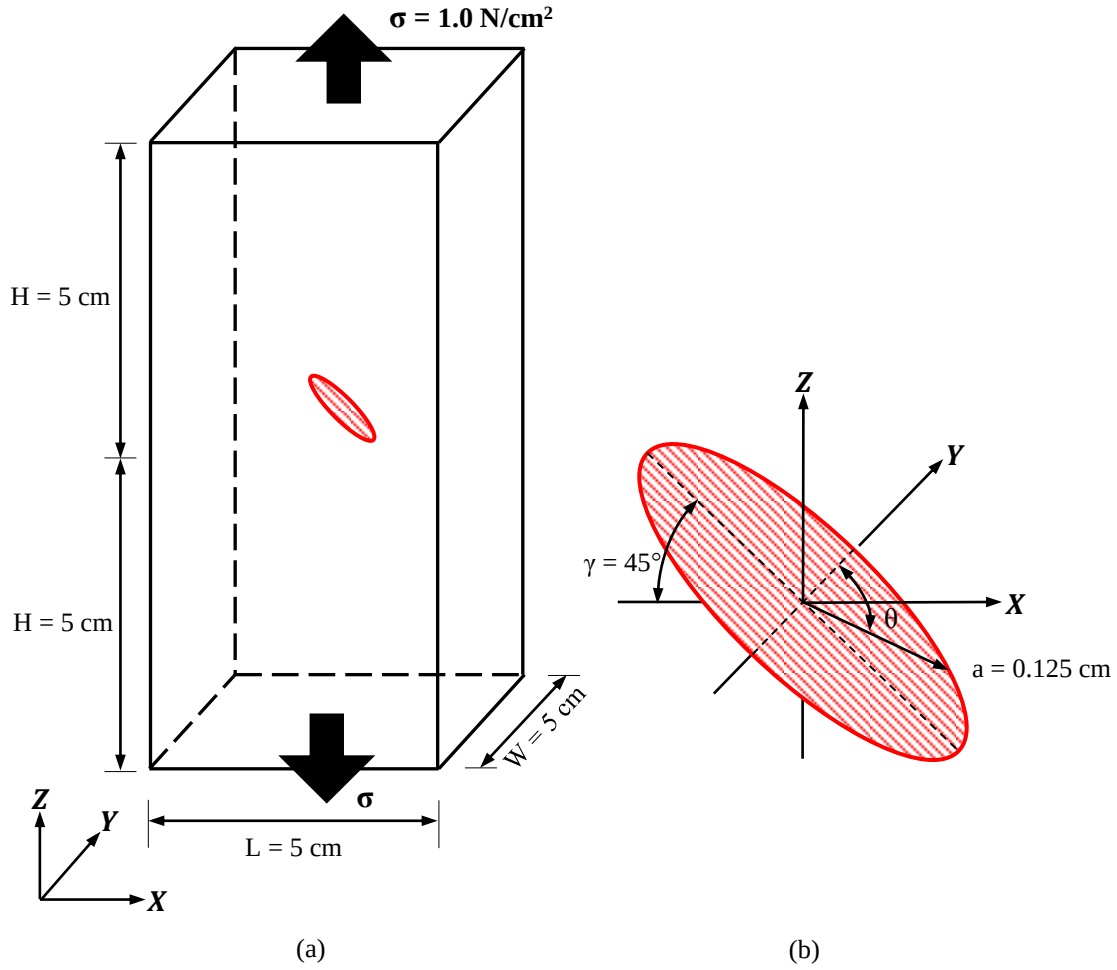

Figure 2.5. Embedded inclined penny crack: (a) global geometry and loading conditions and (b) local crack-front geometry.

The second numerical example was a mixed-mode Arcan specimen [76,77]. The setup consisted of a test fixture and a fracture specimen with a straight-through edge crack, as shown in Figure 2.6. The test fixture and fracture specimen were assumed to be perfectly bonded with coincident mesh interfaces. The Arcan specimen was loaded with an applied displacement at an angle, $\varphi = 60°$, to induce mixed-mode I/II behavior along the crack front.

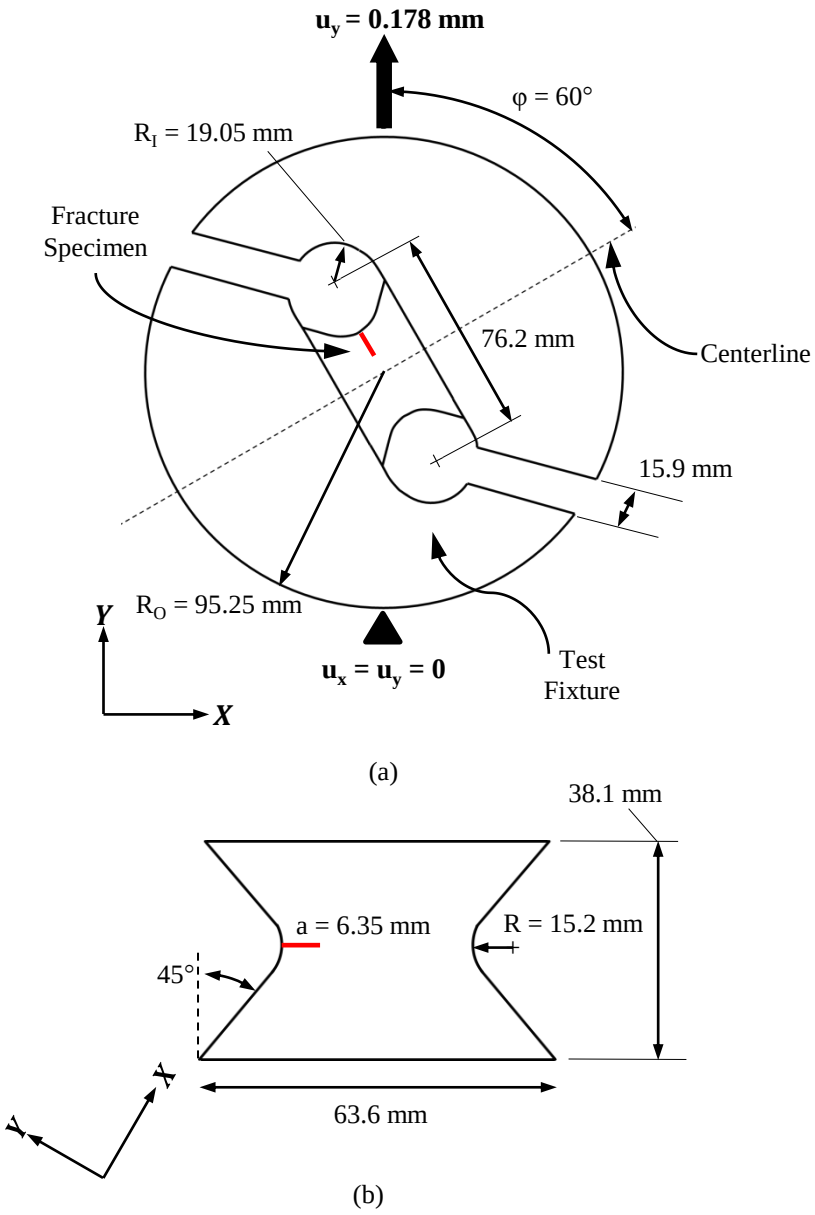

Figure 2.6. Geometry and loading conditions for the Arcan (a) test fixture, thickness of 18.3 mm and (b) fracture specimen, thickness of 2.29 mm.

The third numerical example is a modified three-point bend specimen with an angled crack [78]. Figure 2.7 shows the geometry and loading conditions. The straight-through edge crack was rotated 45° about the center line z-axis. This crack geometry induced mixed-mode I/III behavior along the front. The acute angle created

at the intersection of the crack front and the free surface prohibits a well-formed symmetric crack-front template at the free-surface locations. As a result, the VCE calculations at the free surfaces were truncated. The interior template elements retained the proper symmetric organization.

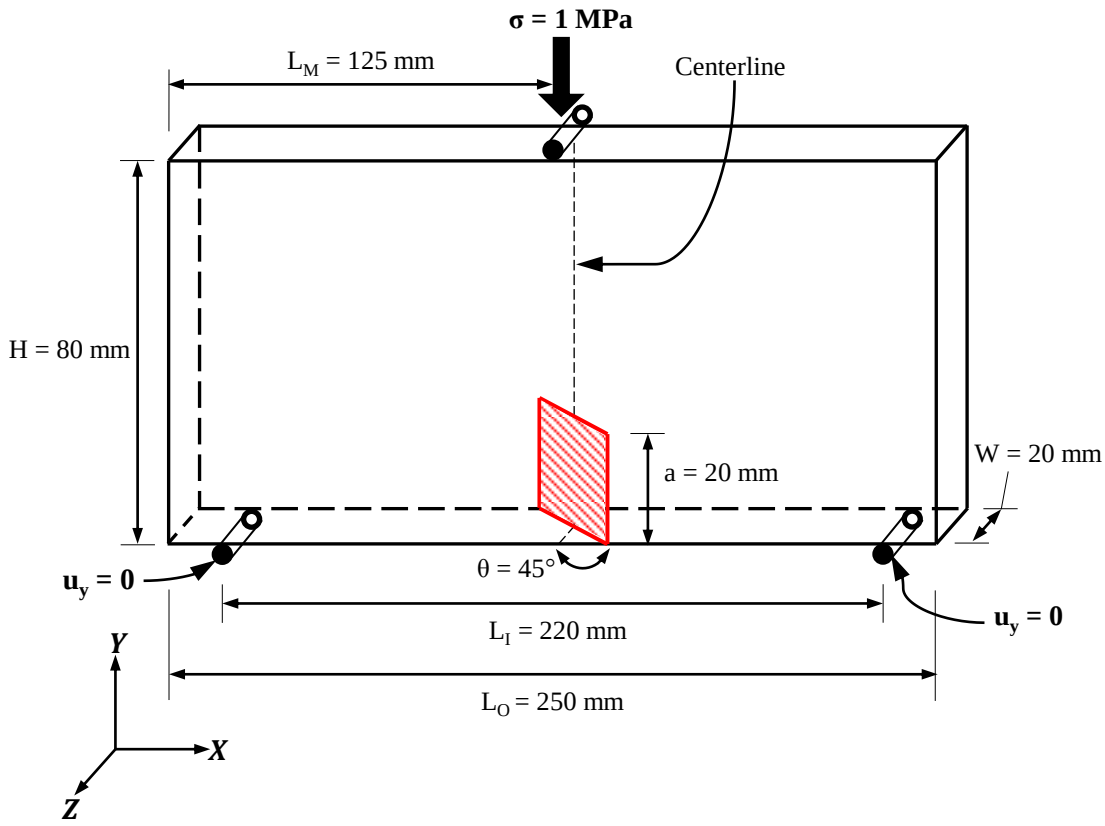

Figure 2.7. Geometry and loading conditions for the angled-crack three-point bend specimen.

The final isotropic numerical example is a half-penny-shaped surface crack in a cylindrical specimen [79,80]. Figure 2.8a shows the global geometry and loading conditions. The local, in-plane geometry of the crack front is depicted in Figure 2.8b. Similar to the modified three-point bend specimen, the crack front intersects the

curved free surface at an acute angle thereby preventing a well-organized template from being formed at the intersection. The interior portion of the crack front template was unaffected and remained in proper form.

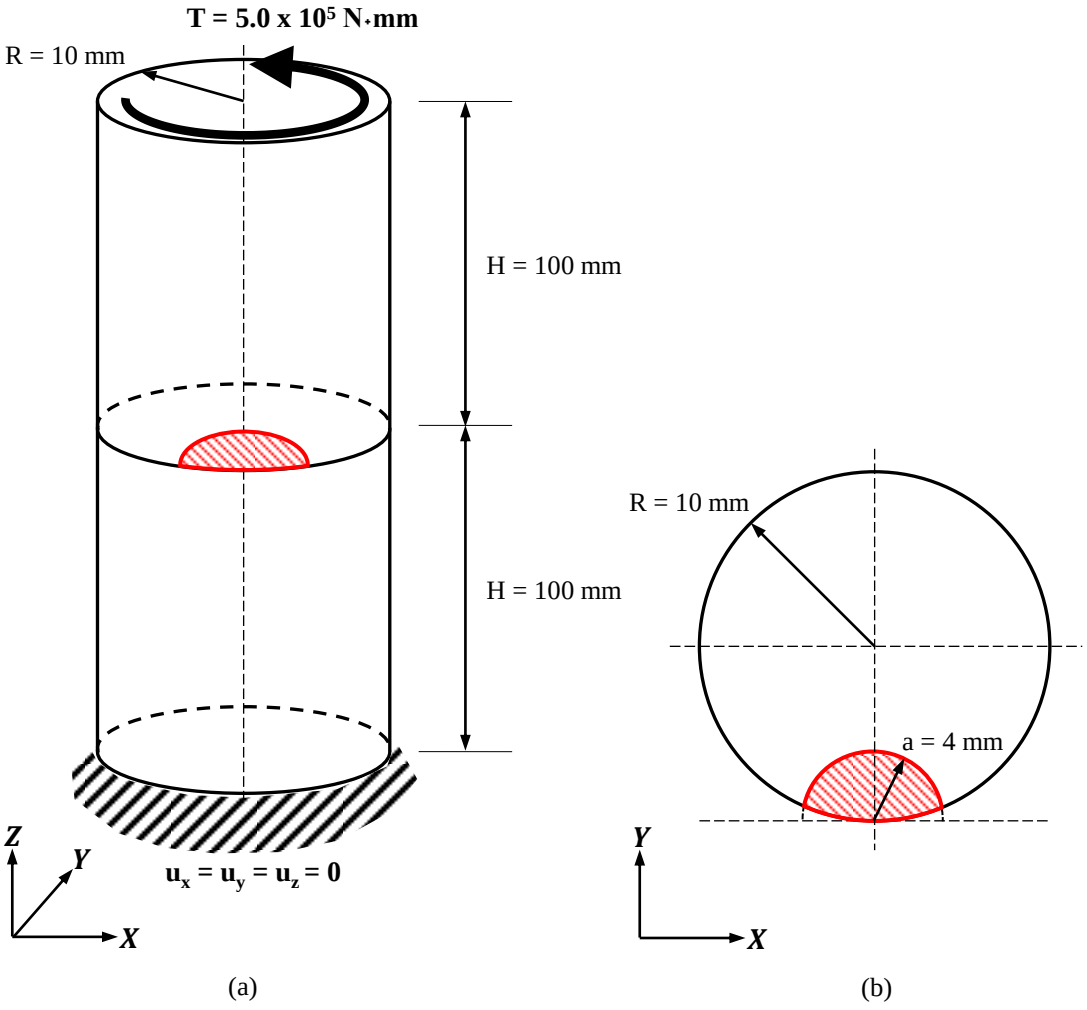

Figure 2.8. Geometry and loading conditions for the half-penny-shaped surface crack in a cylindrical specimen: (a) global geometry and (b) local crack-plane geometry.

2.4.2 Mixed-mode energy release rate results

Figure 2.9 - Figure 2.12 display the mixed-mode and total energy release rate distributions calculated by the VCE implementation for the numerical examples in Section 2.4.1. The reference solutions are not included in the plots because the point-by-point relative difference between the solutions ranged from 0.001% and 0.870%, neglecting free surface effects. At the presented scales of Figure 2.9 - Figure 2.12, the two distributions are indistinguishable. Appendix D contains the individual mixed-mode plots for the inclined penny crack problem, comparing the mode I, II, III, and total energy release rate distributions of the VCE and analytical approaches. Table 2.2 summarizes the average mixed-mode ratios for each model.

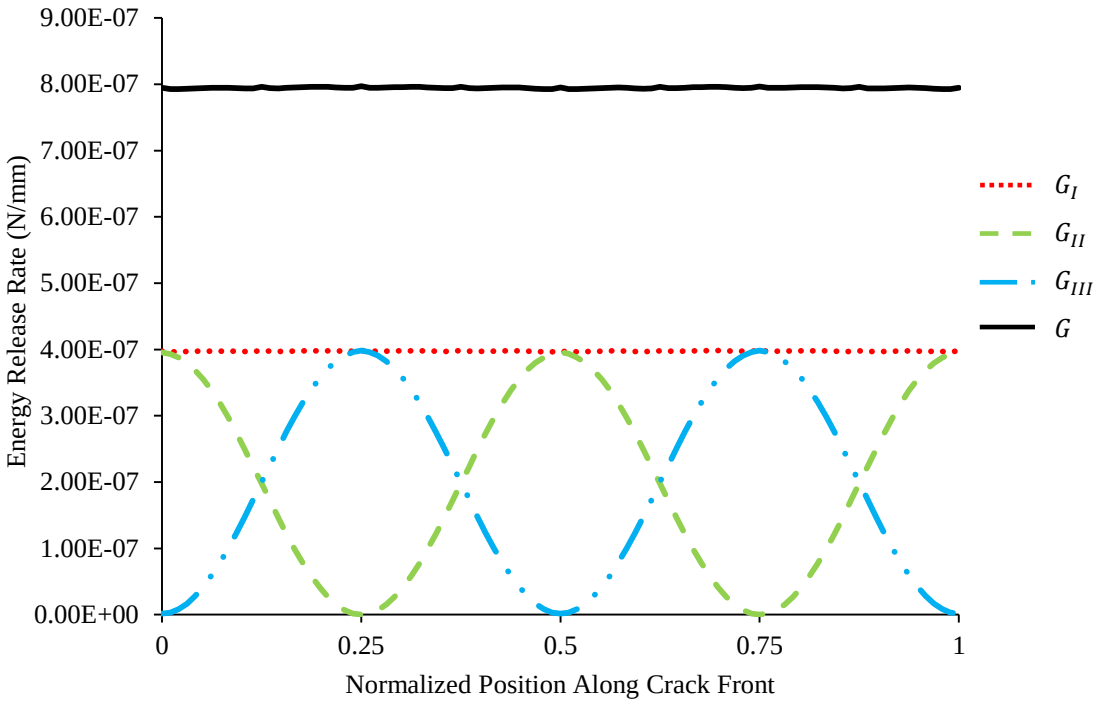

Figure 2.9. Mixed-mode and total energy release rate distributions calculated by the VCE method for the inclined penny-crack specimen.

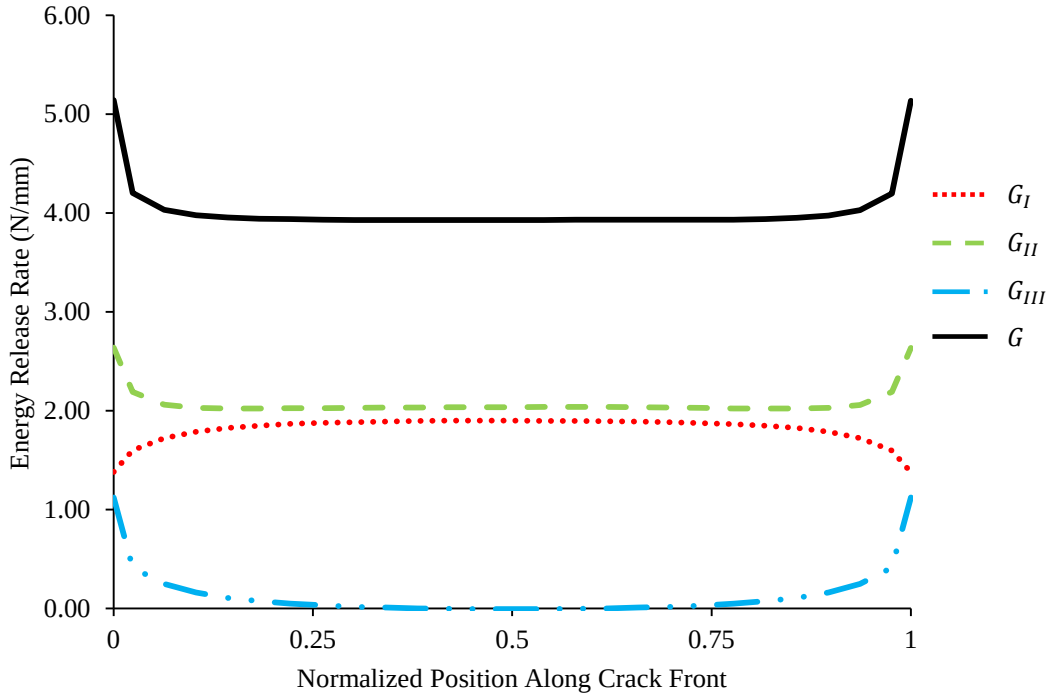

Figure 2.10. Mixed-mode and total energy release rate distributions calculated by the VCE method for the Arcan fracture specimen.

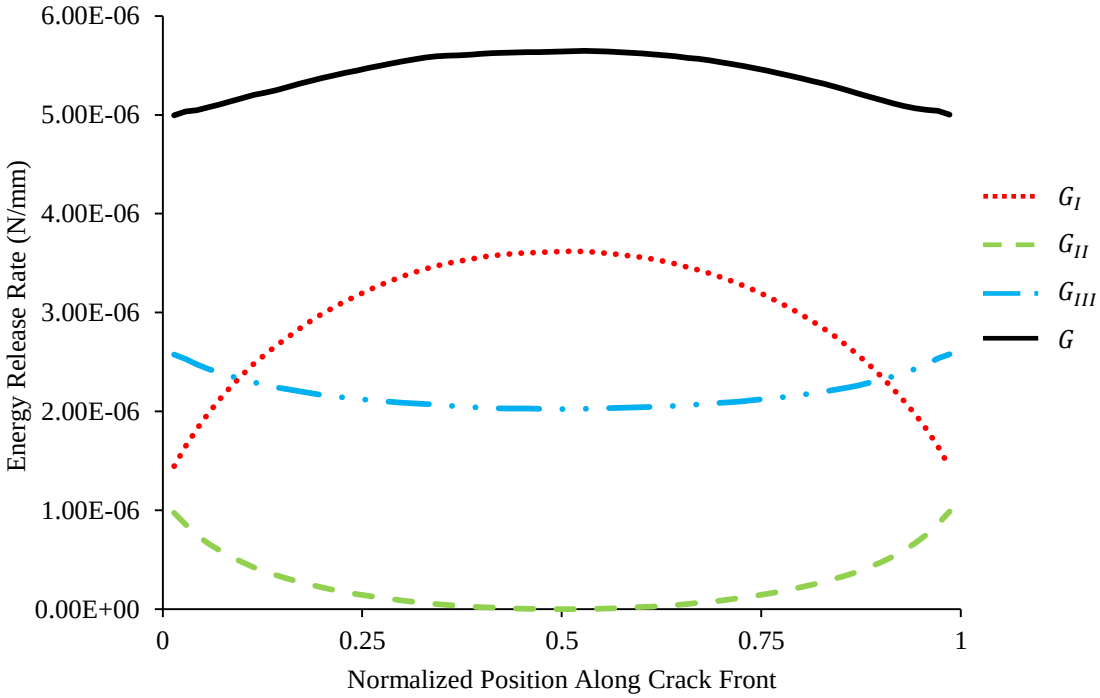

Figure 2.11. Mixed-mode and total energy release rate distributions calculated by the VCE method for the angled-crack three-point bend specimen.

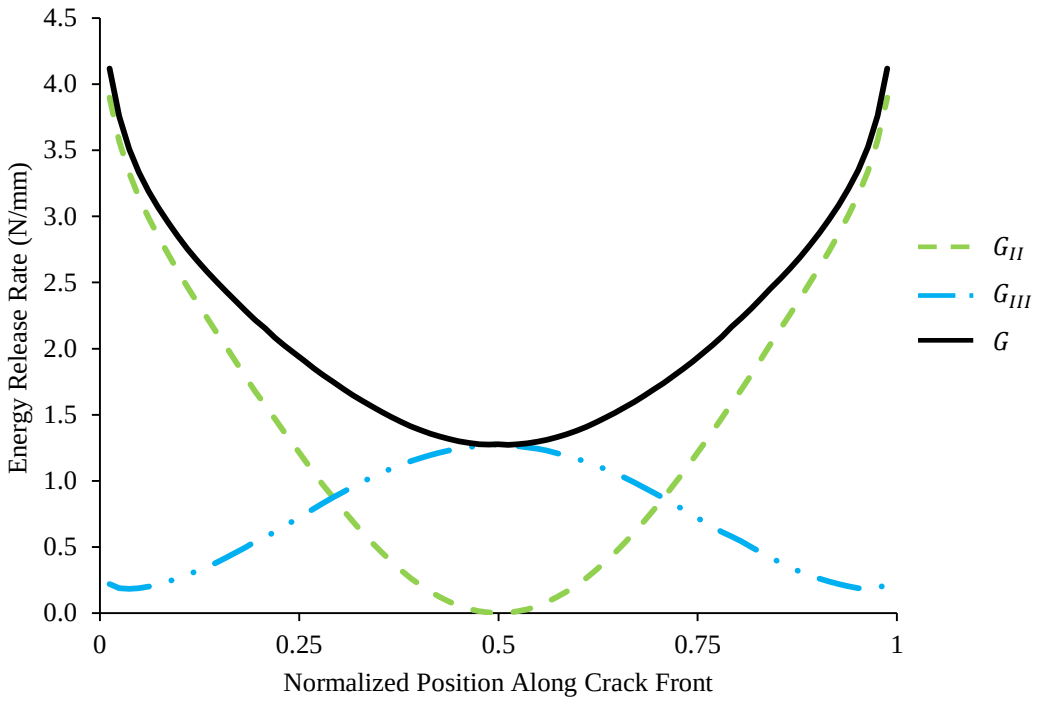

Figure 2.12. Mixed-mode and total energy release rate distributions calculated by the VCE method for the surface-cracked cylindrical specimen.

Table 2.2. Average mixed-mode ratios calculated by the VCE method.

Numerical Example	G_I / G	G_{II} / G	G_{III} / G
Inclined Penny Crack	0.50	0.25	0.25
Arcan Specimen	0.44	0.52	0.04
Angled-Crack 3-Point Bend	0.55	0.05	0.40
Surface-Cracked Cylinder	0.00	0.66	0.34

The mixed-mode and total energy release rates calculated by the VCE method compare extremely well with reference solutions. Table 2.3 summarizes the comparison of average mixed-mode and total energy release rates. While the inclined penny-crack specimen was compared to an analytical reference solution [75], the

remaining examples were verified using the M-integral approach from FRANC3D [71]. Note that the calculated averages neglect free-edge effects where crack fronts intersect the free surface.

Table 2.3. Comparison of average mixed-mode and total energy release rates from the VCE method and reference solutions.

Numerical Example	G_I (N/mm)			G_{II} (N/mm)		
	VCE	Ref. Sol.	% Diff	VCE	Ref. Sol.	% Diff
Inclined Penny Crack	3.974E-07	3.979E-07	0.06	1.976E-07	1.989E-07	0.16
Arcan Specimen	1.845	1.835	0.25	2.039	2.018	0.53
Angled-Crack 3-Point Bend	3.012E-06	2.993E-06	0.35	2.316E-07	2.293E-07	0.04
Surface-Cracked Cylinder	2.146E-05	2.272E-05	0.00	1.358	1.361	0.14

Numerical Example	G_{III} (N/mm)			G (N/mm)		
	VCE	Ref. Sol.	% Diff	VCE	Ref. Sol.	% Diff
Inclined Penny Crack	1.996E-07	1.989E-07	0.09	7.947E-07	7.958E-07	0.14
Arcan Specimen	0.0733	0.0821	0.22	3.957	3.935	0.56
Angled-Crack 3-Point Bend	2.170E-06	2.160E-06	0.19	5.414E-06	5.383E-06	0.58
Surface-Cracked Cylinder	0.7347	0.7419	0.34	2.093	2.102	0.43

The example problems with significant mode III behavior were further investigated to observe the non-zero contribution of the coupling term to the mode III energy release rate. For the inclined penny-crack specimen, angled-crack three-point bend specimen, and surface-cracked cylinder specimen, Figure 2.13 - Figure 2.15, respectively, display the total mode III energy release rate, G_{III}, and the two separate terms as expressed in Eq. (2.19): $G_{II/III}$, and $-\frac{1}{\ell}\left(\frac{1}{2}{u_{III}}^T\frac{\delta K}{\delta a}u_{III}\right)$. Table 2.4 presents

the the average ratios of $G_{II/III}$ to the mode III energy release rate, as well as the other mode coupling terms, $G_{I/II}$ and $G_{III/I}$, to the total energy release rate.

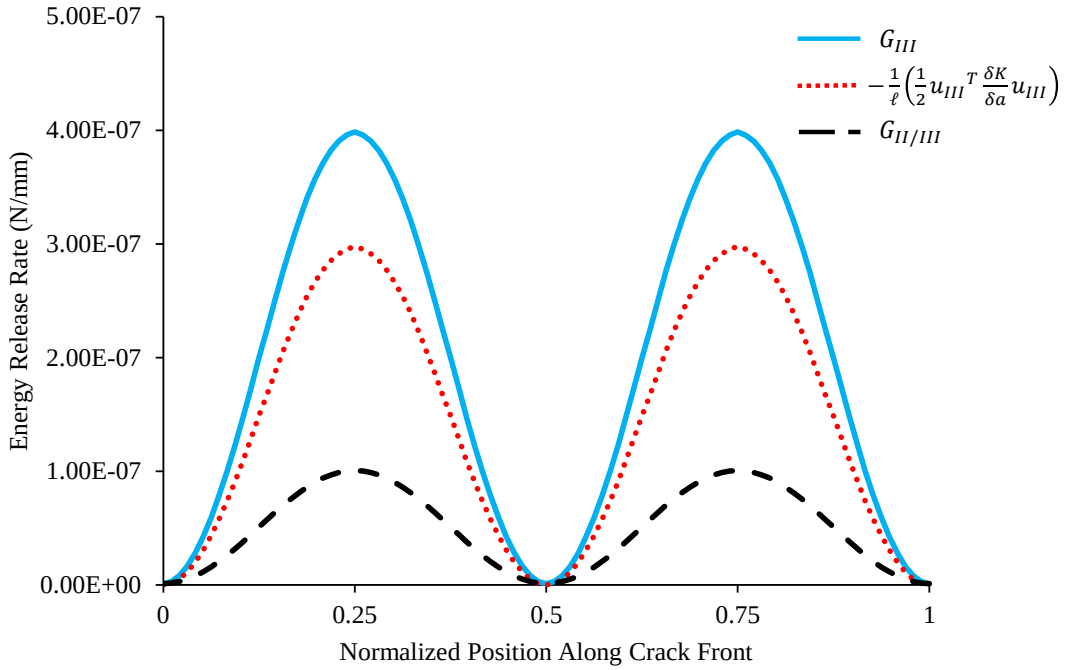

Figure 2.13. Distributions of mode III energy release rate components for the inclined penny-crack specimen.

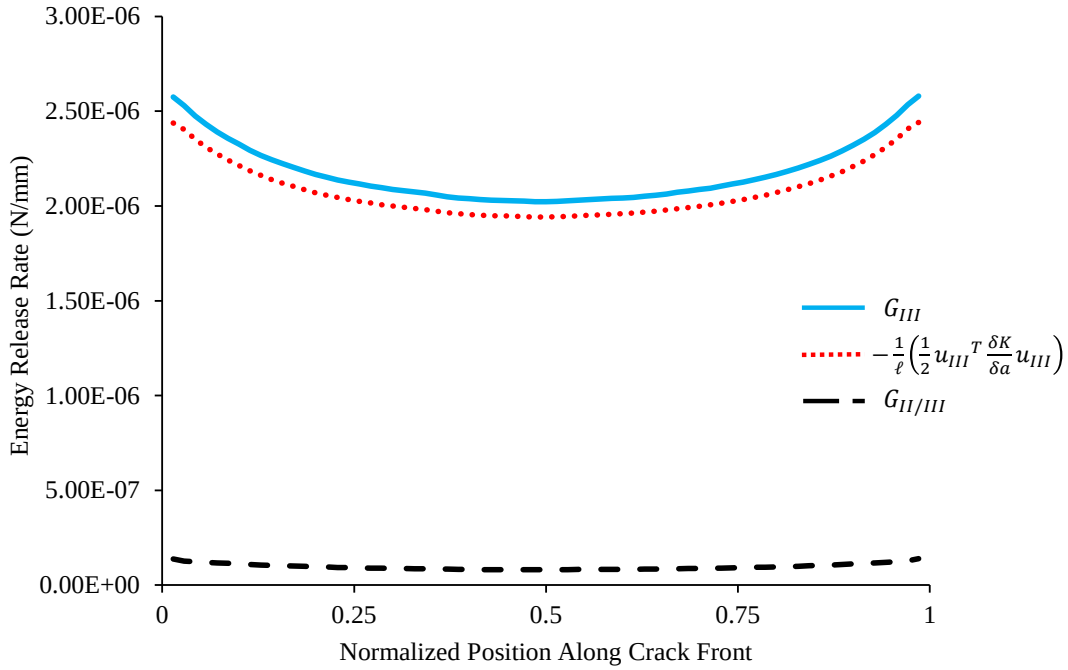

Figure 2.14. Distributions of mode III energy release rate components for the angled-crack three-point bend specimen.

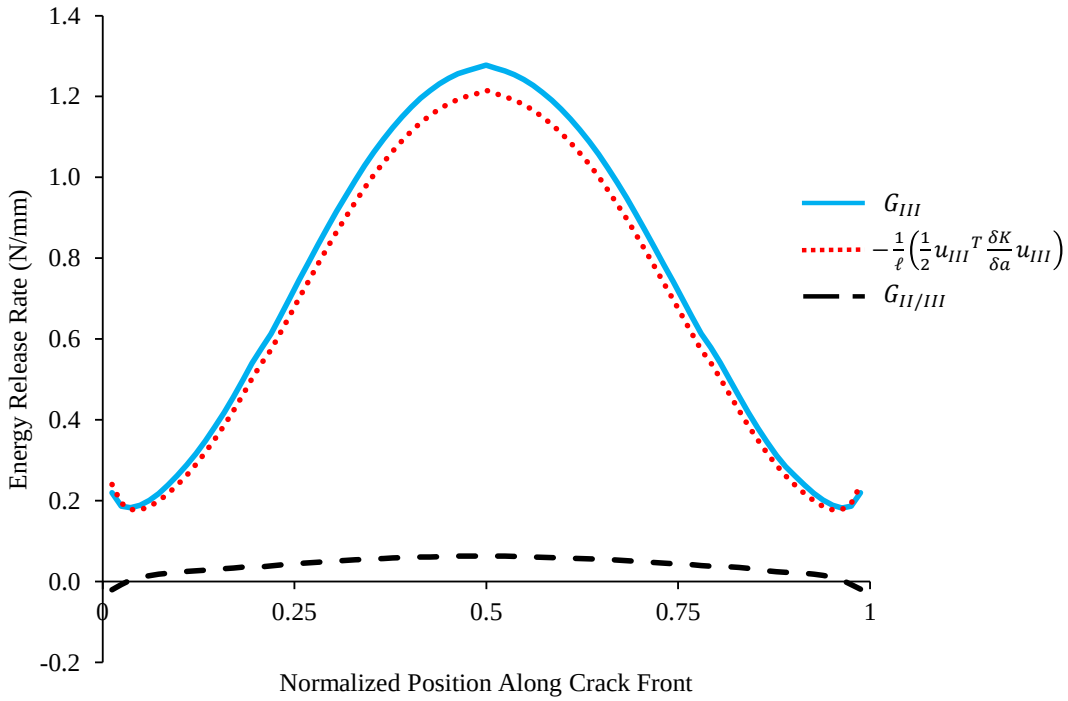

Figure 2.15. Distributions of mode III energy release rate components for the surface-cracked cylindrical specimen. The locally negative coupling term values arise due to a breakdown in the symmetry of the near-crack front displacement fields at the free surfaces.

Table 2.4. Average normalized modal-interaction coupling terms from the VCE method.

Numerical Example	$G_{II/III}$ / G_{III}	$G_{I/II}$ / G	$G_{III/I}$ / G
Inclined Penny Crack	0.26	1.3E-07	2.3E-08
Angled-Crack 3-Point Bend	0.04	9.8E-11	9.5E-09
Surface-Cracked Cylinder	0.06	2.5E-08	5.4E-07

In the first example, the inclined penny crack, $G_{II/III}$ oscillated along the crack front. $G_{II/III}$ was maximum (approximately 25% of the mode III energy release rate) when G_{III} was maximum and G_{II} was minimum. $G_{II/III}$ was at a minimum, with a negligible contribution, when G_{III} was minimum and G_{II} was maximum. The angled-crack three-point bend specimen exhibited relatively uniform mode-mixity ratios across the front. In this case, where mode I/III behavior was dominant, the $G_{II/III}$ term accounted for less than 5% of the total mode III energy release rate. The surface crack in the cylindrical specimen exhibited mode II/III behavior. For this example, the $G_{II/III}$ term contributed only 6% of the total mode III energy release rate. Despite the variance in impact, the $G_{II/III}$ coupling term is certainly significant, especially when operating within a 1% energy release rate error tolerance. The zero contributions from the $G_{I/II}$ and $G_{III/I}$ coupling terms, discussed in Section 2.3, were also verified by the numerical example results.

2.4.3 Single leg bending specimen

The final numerical example is a single leg bending (SLB) specimen [81]. Figure 2.16 shows the geometry and test configuration. The specimen was modeled as a unidirectional ($[0]_{32}$) composite laminate with orthotropic material properties. Table 2.5 summarizes the graphite/epoxy properties used in the analysis. A displacement of $u_z = 2.8$ mm was applied along the midsection of the specimen. The straight edge crack experienced mixed-mode I/II behavior along the front.

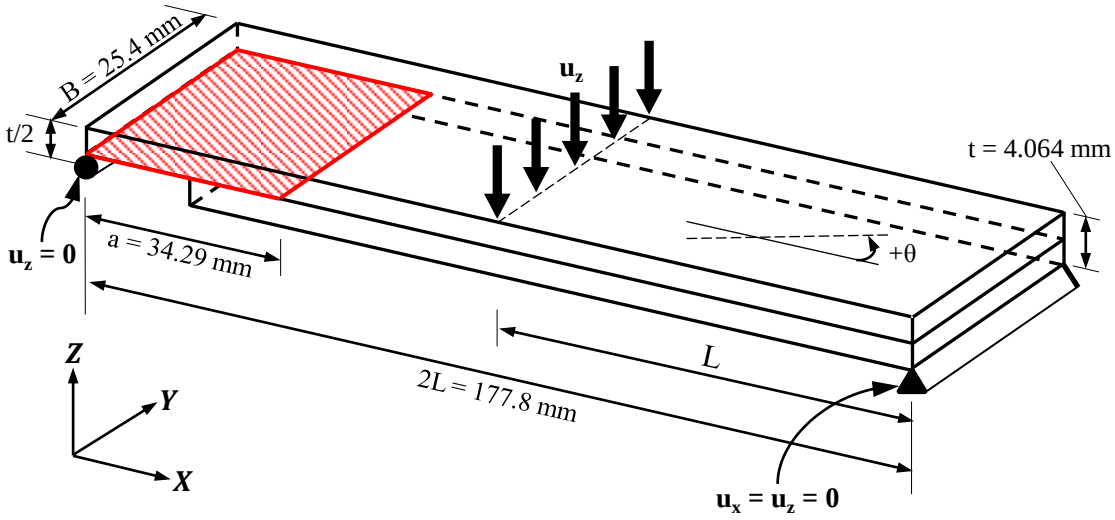

Figure 2.16. Geometry and loading conditions for the SLB specimen.

Table 2.5. Unidirectional material properties for graphite/epoxy lamina.

E_{xx} = 146.86 GPa	ν_{xy} = 0.33	G_{xy} = 5.45 GPa
E_{yy} = 10.62 GPa	ν_{xz} = 0.33	G_{xz} = 5.45 GPa
E_{zz} = 10.62 GPa	ν_{yz} = 0.33	G_{yz} = 3.99 GPa
Single ply thickness =	1.27×10^{-4} m	

The SLB specimen was meshed using the in-house software package tailored to the geometric features of laminated structures. The finite element model contained 64,560 quadratic brick and wedge elements, with a total of 845,580 degrees-of-freedom. The laminate thickness was divided into 16 equal layers of 0.254 mm. The straight-through edge delamination was discretized into 100 segments. The template consisted of three rings of brick elements with a maximum radius of $r_t = 0.762$ mm. The quarter-point brick elements immediately surrounding the delamination front had the following aspect ratios: $l/a = 0.007$ and $l/w = 0.984$ (See Figure 2.4 for parameter reference).

Figure 2.17 shows the mixed-mode energy release rates normalized with the average total energy release rate. The VCE results compare well with the published experimental and finite element results showing a fairly uniform distribution across the delamination front with free-surface effects near the edges due to anticlastic curvature of the delaminated and un-delaminated regions [81,82]. The expected mode I/II behavior resulted in the following average mixed-mode ratios across the front: $G_I/G = 0.60$, $G_{II}/G = 0.40$, and $G_{III}/G = 0.00$.

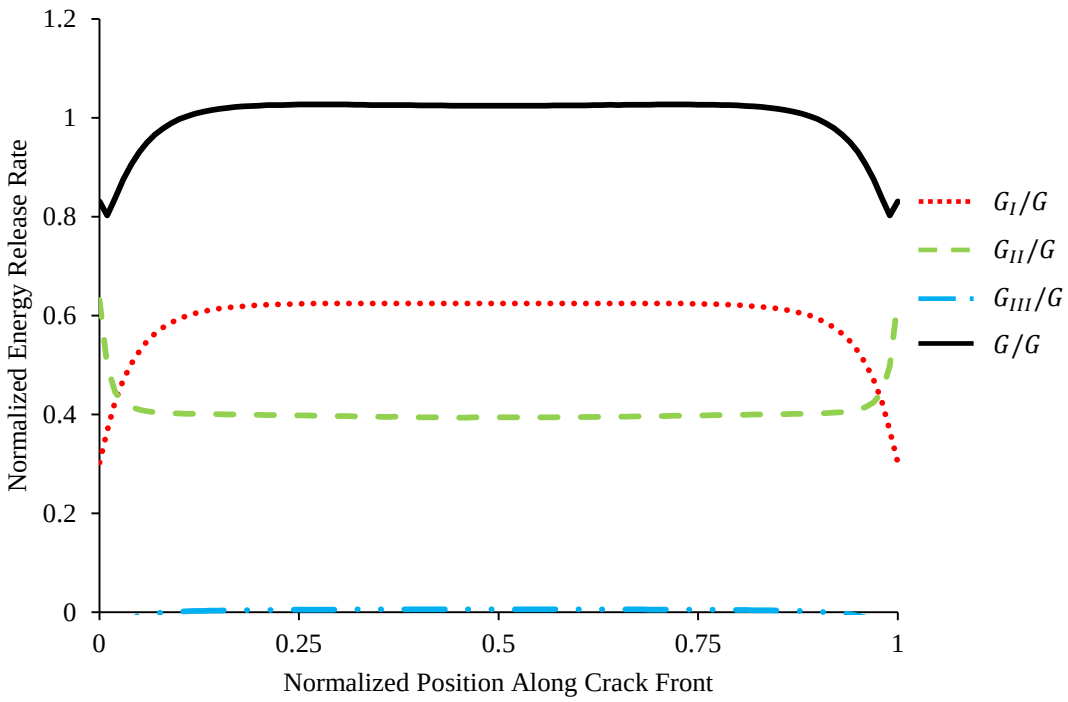

Figure 2.17. Normalized distributions of mixed-mode energy release rates for the SLB specimen.

2.5 Discussion

The five numerical examples demonstrate the accuracy of the presented 3-D mixed-mode VCE implementation for a variety of mode-mixity configurations. In each case, the mixed-mode energy release rates and total energy release rate fall within the 1% error/difference tolerance. The accuracy of the method is determined by the combination of energy release rate distributions along the crack front and the average values. Note that the generated plots show the actual energy release rates calculated at the corner nodes by the VCE method, while the average percent difference

calculations use a linear interpolation to the midside positions for a direct comparison between numerical methods.

The novel contribution of this chapter is the incorporation of the previously overlooked non-zero modal-interaction coupling term, $G_{II/III}$. The calculation of the $G_{II/III}$ term includes both mode II and III decomposed displacements, but only contributes to the mode III energy release rate, as described in Section 2.2.3. The mode III numerical examples agree well with reference solutions, verifying the analytical predictions. The numerical examples also confirm that the $G_{I/II}$ and $G_{III/I}$ coupling terms for a symmetric domain have zero contribution to the mixed-mode energy release rates.

It should be noted that the $G_{II/III}$ term has varying impact on the mode III energy release rate depending on both the overall problem configuration, and the local position on the crack front. In the two numerical examples where the mode III energy release rate was negligible, the $G_{II/III}$ coupling term still influenced the mode III energy release rate value. Regardless of the total mode III presence along the crack front, it is important to account for the contribution of the $G_{II/III}$ coupling term to the mode III energy release rate.

As addressed in Section 2.2.3, the presented VCE mixed-mode energy release rate decomposition technique is limited to problems with material symmetry about the crack plane. This restricts the methodology from being employed for bi-material crack calculations. The total energy release rate at the bi-material crack is captured accurately by the VCE method (Eq. (2.13)), but with the breakdown in symmetry

across the crack plane, the contribution of the coupling terms to the traditional mode I, II, and III energy release rates becomes indeterminate.

This material symmetry restriction on the mixed-mode VCE formulation does not greatly impact its use in the larger framework for simulating quasi-static crack growth at bi-material interfaces, as in cross-ply composite laminates, for example. The salient feature of the VCE formulation is its ability to efficiently obtain total rates of energy release rate, regardless of material properties. These rates of energy release rate have been shown in [67] to provide a mechanics-based approach to explicitly calculate crack extensions allowing for the simulation of arbitrary crack evolution. If mixed-mode information is desired within the crack growth simulation, i.e. for a mixed-mode growth criterion, the computationally inexpensive and easy to implement VCCT can be leveraged to obtain the relative mixed-mode ratios. Those ratios can be used to scale the more accurate VCE total energy release rate predictions, thereby extracting more accurate mode I, II, and III energy release rates.

2.6 Conclusions

This chapter presented the development of a fully 3-D, mixed-mode VCE implementation for the calculation of decomposed energy release rates (G_I, G_{II}, G_{III}) along an arbitrarily shaped crack front. Previous works offered a 2-D method [62] and only suggested its extension to 3-D [36]. The new implementation uses a symmetric/anti-symmetric approach with a local crack-front coordinate system to

obtain mode I, II and III displacements near the front. The decomposed displacements are substituted into the formulation of the global VCE energy release rate expression. Expanding the formulation leads to the emergence of formerly discounted modal-interaction coupling terms: $G_{I/II}$, $G_{II/III}$, and $G_{III/I}$. Through symmetric and anti-symmetric notions, $G_{I/II}$ and $G_{III/I}$ were determined to be zero, while $G_{II/III}$ would have a non-zero contribution to the mode III energy release rate. These results were verified by numerical observations. The mixed-mode energy release rate decomposition technique is limited to homogenous isotropic/anisotropic materials that maintain symmetry about the crack plane.

The five numerical examples confirmed the accuracy of the newly implemented mixed-mode VCE method. The mixed-mode energy release rate results were compared to analytic, M-integral and published results. The VCE results were well within the accepted 1% tolerance with reference solutions. The variety of examples demonstrated the ability of the implementation to accommodate different crack geometries, mode-mixities, and material models (i.e. orthotropic unidirectional layups).

The current implementation is readily available for a variety of crack front applications. The new mixed-mode VCE implementation can also be used within simulation frameworks that employ mixed-mode crack-growth criteria and predict non-planar crack evolution.

CHAPTER 3

3-D SIMULATION OF ARBITRARY CRACK GROWTH USING AN ENERGY-BASED FORMULATION: NON-PLANAR GROWTH

3.1 Introduction

The simulation of 3-D arbitrary crack growth remains a significant challenge and is complicated further by loading or geometric features that induce mixed-mode behavior along the crack front. The resulting crack-front evolution could become curved and tortuous, advancing in arbitrary directions and distances [83]. Utilizing a fracture mechanics approach paired with the finite element method to predict and simulate such intricate crack-shape advances requires three main components: (1) crack representation, (2) fracture parameter (e.g. stress intensity factor or energy release rate) calculations, and (3) crack propagation calculations (i.e. direction and magnitude).

Currently, the prominent techniques for simulating mixed-mode, non-planar crack growth include cohesive zone elements [18,84], the extended finite element method (XFEM) [13,85–88], and explicit crack front re-meshing [25,89–92]. Each approach has been well documented throughout the literature and has demonstrated powerful capabilities for modeling crack-shape evolution. However, as articulated in Chapter 1 [67], crack-growth predictions to date (e.g. described in [13,18,25,84–92]) have been

restricted, to varying extents, due to a reliance on some form of numerical bias or prescribed growth input.

Cohesive zone element approaches explicitly represent the crack front geometry and rely on the energy release rate's relationship with the cohesive traction-separation model to predict growth. The cohesive zone approach has the ability to capture non-linear fracture behavior [17], while allowing crack initiation and growth to progress "naturally" from cohesive model assertions [93]. However, the predicted crack extensions can only occur at the predetermined locations of cohesive elements, leading to a direct bias on the simulated crack path. The extensions are restricted to follow the element boundaries, thereby causing element shape, size and orientation to influence directly the predicted crack-front evolution. Other techniques such as nodal-release methods [94,95] suffer from similar restrictions. To predict pseudo-arbitrary crack-front evolution, these approaches often use high levels of mesh refinement or adaptive meshing techniques [18,22] and populate large volumes of the model with cohesive or nodal-release elements. However, doing so greatly increases the computational cost and does not eliminate the inherent crack growth bias.

XFEM uses a mathematical representation of the crack front, employing enriched finite elements to reproduce the discontinuity across the crack faces and the singular fields near the crack front [11]. XFEM avoids the need to continually update the finite-element mesh that is characteristic of explicit crack front re-meshing techniques. Despite the different forms of crack representation, both XFEM and crack front re-meshing schemes reduce mesh bias. However, each method relies on prescribed user input or cohesive laws to simulate crack extensions. Although a crack trajectory

criterion, such as maximum circumferential stress [96] and maximum energy release rate [48,68], can be used to determine *direction* of the advance, the *magnitudes* of the extensions are often prescribed. The magnitudes of the extensions are usually proportioned along the front based on fracture mechanics parameter distributions or empirical growth laws. In summary, both schemes lack a direct connection between the applied load and resulting crack shape change.

Note, while in theory XFEM can avoid mesh dependent crack growth predictions, most popular contemporary implementations [72] actually locally modify the crack geometry to conform better to the existing mesh. This is done to avoid degenerate or near degenerate crack/element intersections. This modification to the crack geometry simplifies the integration of the enriched elements at the cost of introducing mesh bias to crack growth prediction models.

In Chapter 1, a new finite-element-based simulation technique was developed to predict arbitrary shape evolution of 3-D, planar cracks subjected to quasi-static loading. The technique utilized a new energy-based formulation that allowed for the explicit calculation of crack front extensions. Inspired by concepts from Griffith [97], the formulation is derived from an energy expansion that exploits the first-order variation of the energy release rate. This rate of energy release rate, made readily available via the virtual crack extension (VCE) method [34–36], acts as an influence function that relates changes in energy release rate to changes in geometry along the crack front. This term provides a mechanics-based approach to calculate, rather than prescribe, crack growth increments. The simulation technique also employs a geometrically explicit crack front representation that is continually updated through

re-meshing. As a result, mesh-biased growth is reduced, allowing the crack front to evolve arbitrarily. Note that this explicit representation of the crack geometry within the model is not a limitation of the energy-based formulation, but selected for practical development purposes. The formulation can be used with other crack representation approaches, such as XFEM.

The purpose of the current chapter is to extend the simulation technique presented in Chapter 1 to mixed-mode, non-planar, fully 3-D crack front evolution. To generalize the approach, an augmented toolset is used. The commercial fracture analysis software, FRANC3D [71] is used to explicitly represent and re-mesh the evolving non-planar crack geometries. A new 3-D, mixed-mode VCE implementation, developed in Chapter 2 [98], is used to calculate both energy release rates and the variation of energy release rates along the crack front. A maximum energy release rate criterion is used to extract the point-by-point directions of advances along the front. A salient feature of the new technique is the use of a new basis-function approach within the energy-based growth formulation of Chapter 1.

Using a modified VCE calculation, the new basis-function approach builds an analytical expression to describe the extensions along the front (or segments of the front), rather than relying on the point-by-point calculations used in Chapter 1. This novel method seeks to address numerical sensitivity challenges associated with non-planar crack growth simulations. The amalgamation of complex geometries, finite-element-based calculations, and the local, point-by-point energy-based formulation renders crack growth predictions susceptible to compounding numerical noise. Seemingly insignificant oscillations in the energy release rate distribution along the

front have been found to create substantial instabilities in later crack growth calculations. Employing a truncated series of analytical functions to describe the non-planar extensions along the front mitigates the influence of this numerical noise. The basis-function approach uses a set of global virtual crack extensions to distribute the associated virtual "strains", thereby avoiding point-wise numerical distortions in the VCE calculations. In addition, the overall computational efficiency of the simulation technique is improved by reducing the number of unknowns that require a solution.

Section 3.2 describes the new basis-function approach, providing a summary of the modified VCE calculations and the resulting augmentation to the energy-based growth formulation. Section 3.3 will discuss the basis-function implementation within the incremental, iterative, non-planar crack growth simulation technique. Finally, Section 3.4 offers two example simulations to demonstrate the new, non-planar, crack-growth prediction capabilities.

3.2 The Basis-function approach

Assume that the local crack front extensions, Δa_i, can be represented as a function of position, s, along the front. The crack front extension function, $\Delta \boldsymbol{a}(s)$, can be formed by the combination of independent basis functions, $\boldsymbol{b_k}(s)$:

$$\Delta \boldsymbol{a}(s) = \sum_{k=0}^{n} \boldsymbol{b_k}(s) = \boldsymbol{b_0}(s) + \boldsymbol{b_1}(s) + \boldsymbol{b_2}(s) + \cdots + \boldsymbol{b_n}(s), \tag{3.1}$$

where the subscript k refers to the individual basis functions used in the summation. The selection and total number, n, of basis functions is arbitrary. It is up to the analyst to determine an appropriate form for the crack front extension function that captures the growth behavior. For demonstration purposes, a polynomial form is used herein, but other families of curves, such as trigonometric functions, can be employed. It should be acknowledged that the increased numerical stability and efficiency of the basis-function approach come at a potential cost to the fidelity of crack shape evolution. The approach essentially determines a functional form fitting the crack front extensions. This form is selected by the analyst rather than being obtained from the physics of the problem. However, there is potential to implement an adaptive basis-function scheme that progressively adds higher-order basis functions until a converged shape is reached, thereby improving the fidelity of the crack extension predictions.

The polynomial basis functions in terms of the normalized position along the crack front are represented as:

$$\boldsymbol{b_0}(s) = \Delta b_0, \tag{3.2}$$

$$\boldsymbol{b_1}(s) = \Delta b_1 \cdot s, \tag{3.3}$$

$$\boldsymbol{b_2}(s) = \Delta b_2 \cdot s^2, \tag{3.4}$$

$$\boldsymbol{b_n}(s) = \Delta b_n \cdot s^n, \tag{3.5}$$

where Δb_k represents the coefficients describing the individual basis functions, and s is a normalized position along the crack front.

3.2.1 Augmented energy-based growth formulation

To form fully the expression for the local crack front extensions, the coefficients, Δb_k, for each basis function are required. These terms are obtained by augmenting the energy-based growth formulation that was originally described in Chapter 1:

$$G_{ic} = G_i^0 + \frac{\delta G_i}{\delta P} \odot \Delta P_i + \frac{\delta G_i}{\delta a_j} \Delta a_j.^{\dagger} \tag{3.6}$$

G_{ic} is the critical energy release rate; G_i^0 is the energy release rate along the crack front prior to the applied load increment, ΔP_i; $\frac{\delta G_i}{\delta P}$ is the variation in energy release rate with respect to applied load increment; $\frac{\delta G_i}{\delta a_j}$ is the rate of energy release rate with respect to local virtual crack extensions; and Δa_j is the local crack extension increments. Subscripts i and j indicate positions along the crack front. Equation (3.6) forms a balance expression between the local growth criterion, G_{ic}, and three energetic contributions along the crack front: the current state, the portion due to an incremental load, and the portion due to shape change, i.e. crack growth. The critical parameter in

† $\odot$ denotes the component-wise multiplication of two vectors, $a_i = b_i \odot c_i$

Eq. (3.6) is the rate of energy release rate, $\frac{\delta G_i}{\delta a_j}$. Since this variation of energy release rate is obtained with respect to local virtual crack extensions, the resulting crack growth predictions from Eq. (3.6) are local, point-by-point extensions along the front, Δa_j.

The alternative basis-function approach seeks to determine the coefficients, Δb_k, that describe $\Delta \boldsymbol{a}(s)$. This requires an adjustment to the energy-based growth formulation. The variation of energy release rate is now taken with respect to the *virtual* basis-function extensions, $\delta \boldsymbol{b_k}(s)$, across the crack front segment of interest, s. Substituting the basis-function terms results in the following form of the energy-based growth expression:

$$G_{ic} = G_i^0 + \frac{\delta G_i}{\delta P} \odot \Delta P_i + \frac{\delta G_i}{\delta \boldsymbol{b_k}} \Delta b_k. \tag{3.7}$$

3.2.2 Global virtual crack extension method

To calculate the variation of energy release rate with respect to the global basis functions, the VCE method is modified. As mentioned previously, the traditional VCE method applies a local virtual extension, δa_i, at each position along the front to obtain the energy release rates. The simplified expression for the energy release rate becomes:

$$G_i = -\frac{1}{\ell_i}\left(\frac{1}{2}u^T\frac{\delta K}{\delta a_i}u\right), \tag{3.8}$$

where K is the stiffness, u is the nodal displacements, and ℓ is a geometric parameter associated with the virtual extension area. The expression for the variation of the energy release rate with respect to an additional local virtual extension, δa_j, extends from Eq. (3.8):

$$\frac{\delta G_i}{\delta a_j} = -\frac{1}{\ell_i}\left(u^T\frac{\delta K}{\delta a_i}\frac{\delta u}{\delta a_j} + \frac{1}{2}u^T\frac{\delta^2 K}{\delta a_i \delta a_j}u\right). \tag{3.9}$$

However, the basis-function modification to the VCE method applies a variation to Eq. (3.8) with respect to the global virtual extensions, $\delta\boldsymbol{b_k}$, resulting in the new form:

$$\frac{\delta G_i}{\delta \boldsymbol{b_k}} = -\frac{1}{\ell_i}\left(u^T\frac{\delta K}{\delta a_i}\frac{\delta u}{\delta \boldsymbol{b_k}} + \frac{1}{2}u^T\frac{\delta^2 K}{\delta a_i \delta \boldsymbol{b_k}}u\right). \tag{3.10}$$

This introduces two new terms: the global variation of nodal displacements, $\frac{\delta u}{\delta \boldsymbol{b_k}}$ (which includes the first-order variation of stiffness, $\frac{\delta K}{\delta \boldsymbol{b_k}}$), and the second-order variation of the stiffness matrix with respect to a combination of local and global virtual extensions, $\frac{\delta^2 K}{\delta a_i \delta \boldsymbol{b_k}}$. The formulation of these terms, to comprise the new global virtual crack extension (GVCE) method, extends directly from the traditional, 3-D VCE expressions found in [36] with the proper substitution of $\delta\boldsymbol{b_k}$ for δa_j.

The term of interest in Eq. (3.10) is $\frac{\delta u}{\delta \boldsymbol{b_k}}$. In the traditional VCE formulation, the variation of nodal displacements, $\frac{\delta u}{\delta a_j}$, is obtained by taking the variation of the finite-element equilibrium equation, $Ku - f = 0$, with respect to a local virtual extension. Assuming no crack face tractions, such that $\frac{\delta f}{\delta a_j} = 0$, the resulting expression follows:

$$\frac{\delta u}{\delta a_j} = -K^{-1}\frac{\delta K}{\delta a_j}u. \tag{3.11}$$

This form of the variational displacements potentially yields poor predictions affecting the traditional variation of energy release rate, $\frac{\delta G_i}{\delta a_j}$. $\frac{\delta K}{\delta a_j}u$ is a "force-like" term resulting from the local virtual extension. Similar to applying a point force at a node in a standard finite-element problem, the localized $\frac{\delta K}{\delta a_j}u$ term produces a region of numerical distortion near the area of application leading to inaccuracies in the calculation.

By introducing the basis-function approach, the global virtual extensions are distributed over a larger segment of the crack front. Equation (3.13) taken with respect to the global virtual extensions becomes:

$$\frac{\delta u}{\delta \boldsymbol{b_k}} = -K^{-1}\frac{\delta K}{\delta \boldsymbol{b_k}}u. \tag{3.12}$$

Analogous to applying a distributed force instead of a nodal force, this form for the variation of displacements alleviates the numerical distortion associated with the local perturbations.

It is important to note that the local virtual-extension approach is still used to calculate energy release rates along the front, and the supplemental global virtual extensions associated with the basis functions are leveraged to calculate the variations of energy release rate.

3.2.3 Implementation of the global virtual crack extension approach

The transition from the local virtual-extension approach to the global approach does not require significant modifications to the VCE formulation or implementation. The primary change within the GVCE method is the application of the virtual extensions. Figure 3.1a illustrates the traditional form, where each position, i, along the front experiences a local virtual extension, δa_i. In this case, a unit, linear virtual extension is applied at the position of interest and is tapered to zero at the adjacent positions, $i + 1$, and $i - 1$.

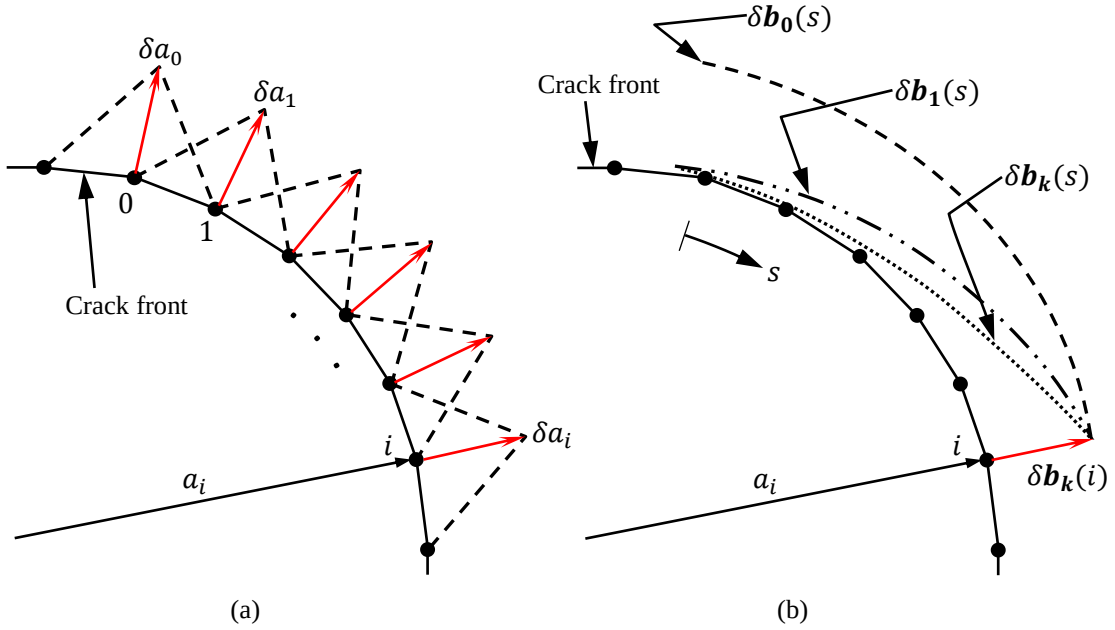

Figure 3.1. Schematics comparing (a) the traditional local virtual extension approach, and (b) the basis-function approach that uses a series of "global" virtual extensions.

Figure 3.1b shows the virtual extensions used within the global, basis-function approach. Here the virtual extensions are constructed in a "global" sense, along the entire crack front segment of interest, s. This requires non-zero virtual extensions at adjacent positions for calculations at position i, as exemplified in Figure 3.2. The global virtual extensions, $\delta \boldsymbol{b_k}(s)$, are applied independently with unit coefficients governing the expressions. Therefore, each crack front position requires n global virtual extension calculations.

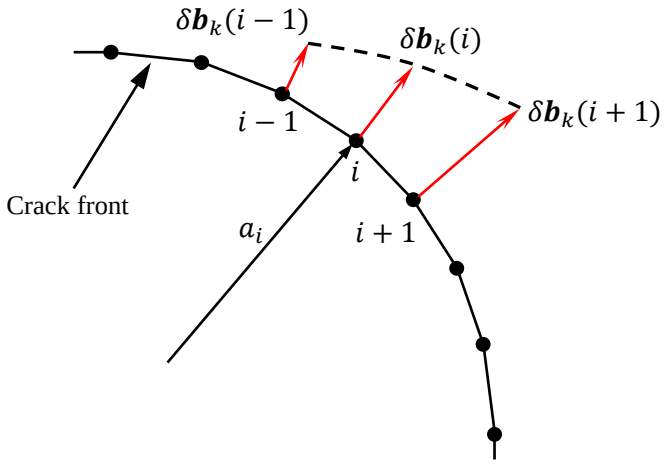

Figure 3.2. Schematic of global virtual extensions applied using the basis-function approach to calculate rates of energy release rates at crack-front position i.

The resulting $\frac{\delta G_i}{\delta \boldsymbol{b_k}}$ matrix from Eq. (3.10) is non-square. Typically, the number of crack front positions is much greater than the number of basis-functions used. Within the energy-based growth formulation of Eq. (3.7), the superfluous energy added to the system from the load increment, denoted by subscript g, is used to solve for the basis-function coefficients, Δb_k:

$$-\frac{\delta G_i}{\delta P} \odot \Delta P_{ig} = \frac{\delta G_i}{\delta \boldsymbol{b_k}} \Delta b_k. \tag{3.13}$$

In general, Eq. (3.13) is an over-determined system, requiring a normal equation or singular value decomposition approach to obtain Δb_k. The system has been made more computationally efficient by reducing the number of unknowns, no longer requiring a solution for extensions at each crack front position as in the point-by-point approach of Chapter 1. The determined coefficients can then be used to generate Eq.

(3.1) to obtain an explicit expression for extensions along the front for a given load increment.

3.3 Non-planar growth simulation technique

The basis-function approach with the GVCE method is used with the simulation technique developed in Chapter 1. The algorithm employs an incremental-iterative procedure to predict growth. The technique involves finite-element model generation, analysis, fracture mechanics calculations, the basis-function crack growth formulation, and crack geometry updates via re-meshing. The ABAQUS commercial finite element software [72] is used as both the environment and solver for the simulations. As described in Section 3.2, the mixed-mode GVCE method is used for fracture mechanics calculations, taking advantage of its ability to extract rates of energy release rate. To allow for non-planar behavior, the current implementation also includes crack-trajectory predictions based on a maximum energy release rate criterion [48,68]. FRANC3D [71] is used to construct meshes that conform to the predicted, non-planar crack geometry.

3.3.1 Crack-growth formulation

The simulation technique requires an initially stable crack front configuration, i.e. for all positions along the crack front:

$$G_i \leq G_{ic}. \tag{3.14}$$

As in Chapter 1, the current implementation uses a total critical energy release rate as its crack growth criterion. This criterion is not a requirement of the technique or the growth formulation but is selected for development purposes. An effective energy release rate criterion that incorporates mode-mixity contributions would be more realistic for non-planar growth. A variable G_{ic} vector can also be incorporated that takes into account non-uniform fracture toughness as in cross-ply fiber laminates, for example.

After an applied load increment, ΔP_i, the energy release rates are calculated again. If the updated energy release rates remain at or below the critical energy release rate, no growth is predicted and the simulation proceeds to the next load increment. However, if the updated energy release rates exceed the critical value, the energy-based crack growth formulation is activated. The energy surpassing the critical value is separated, and the contributing component for growth is used in Eq. (3.13) to determine the basis-function coefficients.

The resulting expression for the crack front extensions, $\Delta \boldsymbol{a}(s)$, is used to calculate the local extensions at each discretized position along the front. In the current implementation and for the examples presented in Section 3.4, s is taken to be the entire length of the front. This is not a requirement; the basis-function approach can be applied across multiple segments of the front. The procedure is repeated until the

energy release rates for the updated geometry at the applied load increment satisfy Eq. (3.14), thereby reaching a stable configuration.

For a more detailed discussion of the general simulation algorithm and crack growth formulation, please refer to Chapter 1 of this dissertation [67].

3.3.2 Maximum energy release rate trajectory criterion

A critical component of the new implementation is its ability to track non-planar crack front evolution. In this version, a maximum energy release rate criterion is used to predict crack front extension directions. Use of other methods, such as maximum circumferential stress, is possible. The maximum energy release rate approach was deemed most practical considering the use of the GVCE method.

Using a local crack-front coordinate system, a series of virtual extensions that sweep radially within the crack front normal plane at angle φ are applied to each position along the front. Figure 3.3 shows the crack front normal plane for position i, and the bounding virtual extensions that range from $\varphi = +/-\beta$ about the 0° crack front normal. Within this range, incremental virtual extensions are applied at an interval angle, α. The corresponding energy release rates are calculated for each trial virtual extension via the VCE method. For the simulation examples presented in Section 3.4, $\beta = 60°$ and $\alpha = 5°$, resulting in 25 trial virtual extensions for each crack front position. From the generated distribution of energy release rates for each position, the angle φ_i associated with the maximum value is chosen as the local

extension direction. The associated cost of the extra VCE calculations is minor compared to the total computations required for the crack growth simulation.

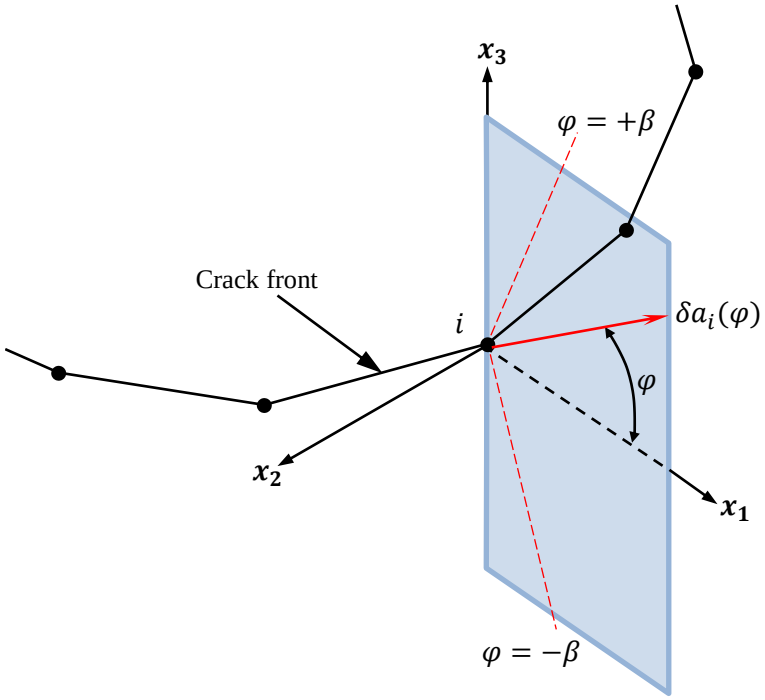

Figure 3.3. Schematic of the radially applied, local virtual extensions used with the VCE method to determine the direction of maximum energy release rate at position i along the crack front.

3.3.3 Re-meshing with FRANC3D

To maintain the evolving crack geometry, the entire crack surface is tracked through the simulation procedure. The crack surface geometry is updated by applying the calculated extension vectors for each position along the front. FRANC3D 6.0.5 software [71] is used to re-mesh the updated geometry. The FRANC3D meshing scheme relies on a local crack-front element template to surround the geometrically explicit crack representation, portrayed in Figure 3.4a. The template, as shown in Figure 3.4b, encompasses the crack front with a ring of eight, 15-noded quarter-point wedge elements. A user-controlled number of standard 20-noded, quadratic, brick-element rings encircle the quarter-point ring, creating a rosette template. In the example simulations of Section 3.4, a three-ring template is used. The remaining volume is meshed using predominately 10-noded tetrahedral elements.

The use of the crack-front template improves the integration schemes and accuracy of the GVCE calculations [98]. However, the adherence to the template geometry introduces some limitations when applying crack front extensions. A balance needs to be maintained between the "template radius" and the updated geometry so that a well-formed mesh can be constructed along the crack front.

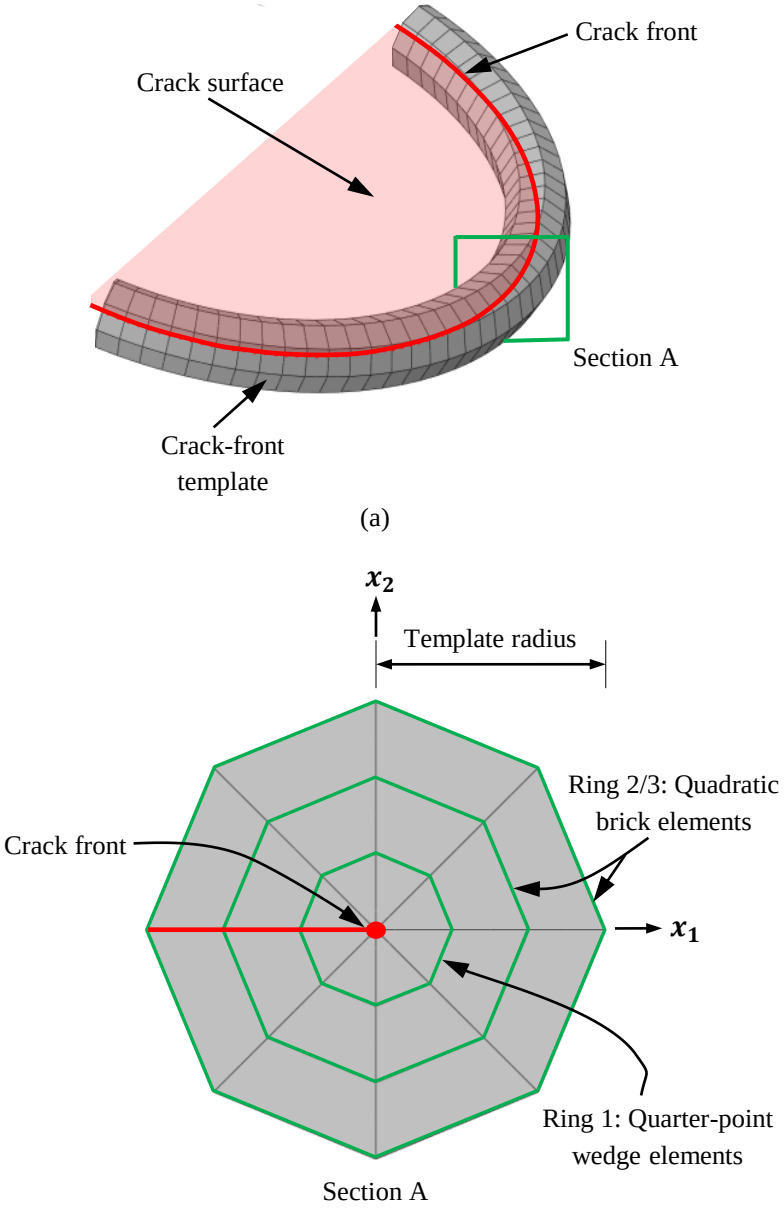

Figure 3.4. (a) Segment of a crack front surrounded by the crack-front template. (b) Planar section of the crack-front template exposing the element configuration.

3.4 Non-planar crack growth simulations and results

In this section, two example crack growth simulations are presented to verify the new, non-planar predictive capabilities. Both make use of a modified edge-crack specimen to induce mixed-mode behavior along the crack front. Each model is also loaded under displacement control to ensure a stable crack growth situation. Here crack *growth stability* refers to the sign of the change in energy along the crack front with respect to crack extension. Section 3.4.1 describes the simulation of an initially declined crack that exhibits crack path instability, whereas Section 3.4.2 illustrates the simulation of an initially angled crack that tends towards a stable crack path. In this context, crack *path stability* refers to directional change of the advancing crack shape [99,100].

Having a stable crack growth problem ensures that the energy release rate decreases with crack extension. This means that a stable crack front configuration can be predicted for a given load increment that satisfies Eq. (3.14). The simulations enforce Eq. (3.14) with a normalized residual tolerance of $\left|\frac{G_i - G_{ic}}{G_{ic}}\right| \leq 0.05$. This tolerance was deemed acceptable considering the confluence of numerical calculations and finite element analyses for the complicated non-planar crack growth behavior. The energy release rates used in the simulation procedure are total energy release rates associated with the direction determined from the maximum energy release rate criterion. The variations of energy release rates were determined using the GVCE method described in Section 3.2. A third-order polynomial constituted the set of basis functions, consisting of a constant, linear, quadratic, and cubic term.

Both specimens were modeled as an isotropic material with Young's modulus, $E = 700$ MPa, and a Poisson's ratio, $\nu = 0.1$. A constant, local, critical energy release rate was selected for both cases. Note that the example simulations presented are demonstrative and use arbitrary geometries and material properties without loss of generality.

3.4.1 Declined crack specimen

The first simulation, shown in Figure 3.5, consisted of an initially declined crack geometry. The crack is rotated $15°$ about the global Z-axis and centered along the neutral axis of the specimen. For this configuration, a constant, critical energy release rate of $G_{ic} = 0.385$ N/mm was arbitrarily selected for each position along the front. An initial applied displacement of $u_y = 1.00$ mm was followed by 20 additional displacement increments that ranged from $0.01 - 0.06$ mm. The final total applied displacement reached was 1.68 mm.

The initial model, generated using FRANC3D, consisted of 23,038 elements and a total of 115,371 degrees of freedom. Throughout the simulation, the crack front was discretized into 28-30 element segments with an average template radius of 2.48 mm. The number of degrees of freedom and crack front discretization vary with the evolving geometry to maintain well-formed meshes.

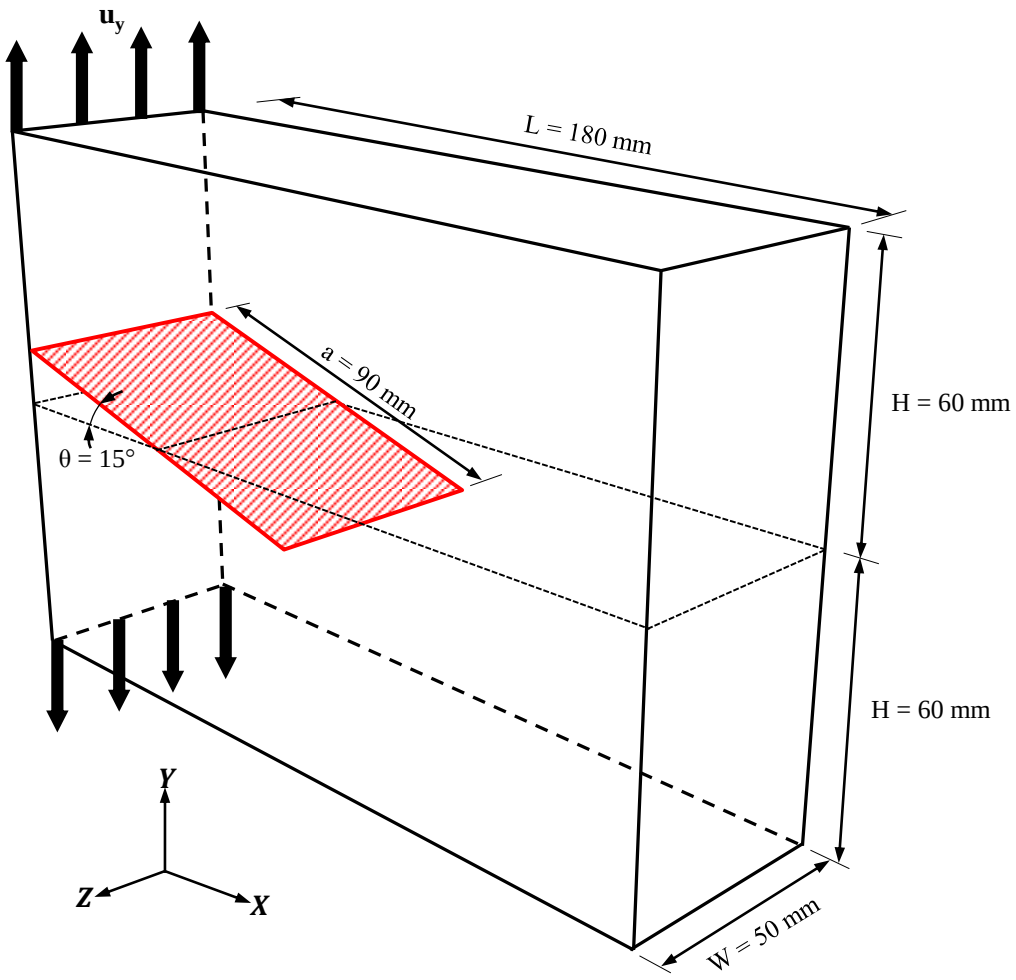

Figure 3.5. Declined crack specimen initial geometry and boundary conditions.

Figure 3.6 shows the initial "straight-ahead" mixed-mode energy release rate distributions along the crack front. The behavior is predominately mode I with the following mixed-mode ratios: $G_I/G = 0.98$, $G_{II}/G = 0.02$, and $G_{III}/G = 0.0$. The combination of the mode II presence and the geometric "kink" of the declined crack front induce non-planar crack growth. Using T-stress and path stability notions from [100], the crack evolution is expected to progress ahead and in the negative-Y direction.

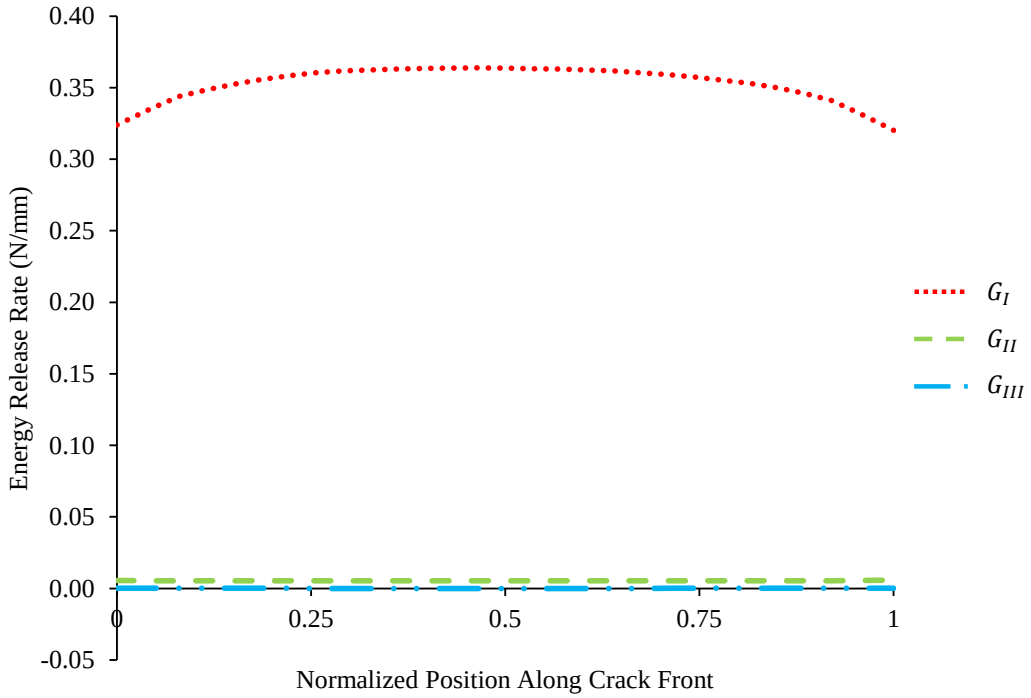

Figure 3.6. Initial mixed-mode energy release rate distributions for the declined crack configuration.

A stable crack front configuration according to Eq. (3.14) was reached for each of the 20 applied displacement increments. The average energy release rate residual compared to the critical value was approximately 2.8%. An average of three crack-front extension iterations were required to obtain each stable configuration. Figure 3.7 shows selected stages of the crack front propagation as the applied displacement was increased. The predicted shape evolution compares qualitatively well with a less accurate, quasi-static, FRANC3D, crack growth analysis using prescribed extension increments and a trajectory criterion based on maximum circumferential stress.

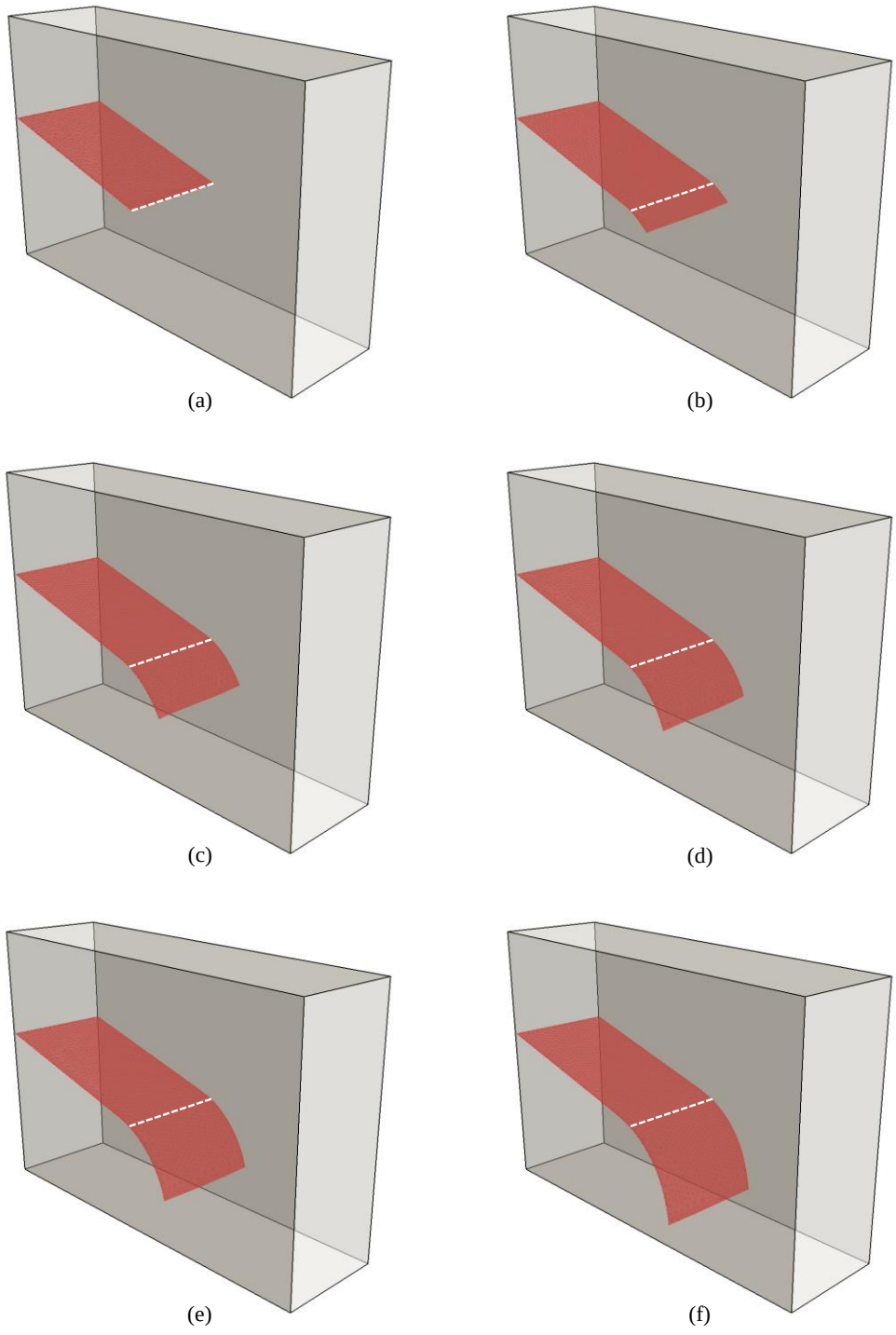

Figure 3.7. (a) Initial crack-front geometry for the declined crack specimen. (b)-(f) Predicted geometries for the evolving crack front after displacement increments 2, 4, 6, 10, and 20, respectively.

3.4.2 Angled crack specimen

Figure 3.8 depicts the initial geometry for the second simulation. In this configuration, the initial crack geometry is rotated 15° about the X-axis and centered along the neutral axis. A constant, critical energy release rate of $G_{ic} = 0.360\ \mathrm{N/mm}$ was chosen. Again, the simulation began with an initial applied displacement of $u_y = 1.00$ mm. Fourteen displacement increments were applied, ranging from $0.05 - 0.10$ mm. The final total applied displacement was 1.90 mm.

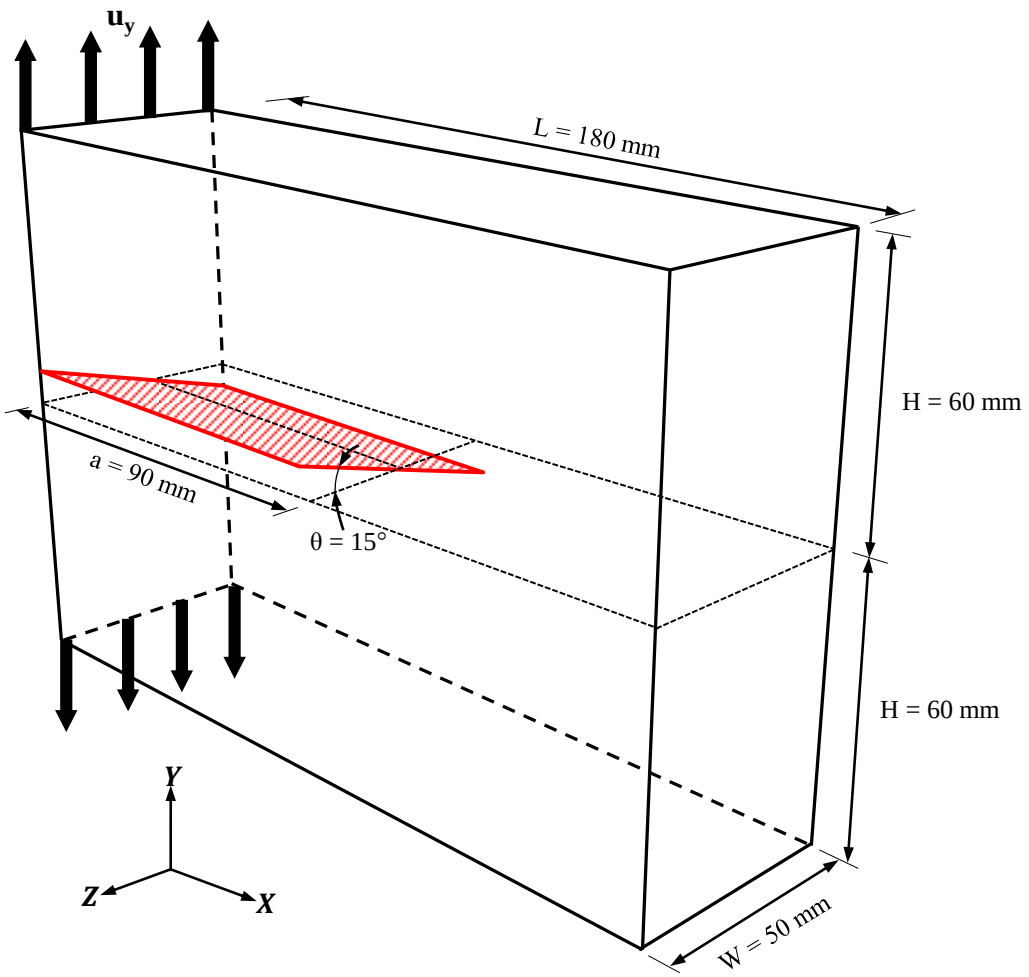

Figure 3.8. Initial geometry and boundary conditions for the angled-crack specimen.

The initial finite element model contained 24,641 elements and a total of 124,332 degrees of freedom. Throughout the 14-step simulation the crack front discretization varied, ranging from 34-54 element segments with an average template radius of 1.76 mm.

Figure 3.9 shows the initial "straight-ahead" mixed-mode energy release rate distributions along the angled crack front. In this configuration, mode I remained the prevailing contribution, but there was a consistent mode III influence along the front, as well as a mode II contribution near the free surfaces. The averaged mixed-mode ratios along the front were: $G_I/G = 0.96$, $G_{II}/G = 0.01$, and $G_{III}/G = 0.03$. Observing simulations of similar initial-crack configurations in the literature, such as the angled three-point-bend specimen [78,86,91,92,101], the crack is expected to grow and rotate back towards a planar configuration in the $X - Z$ plane.

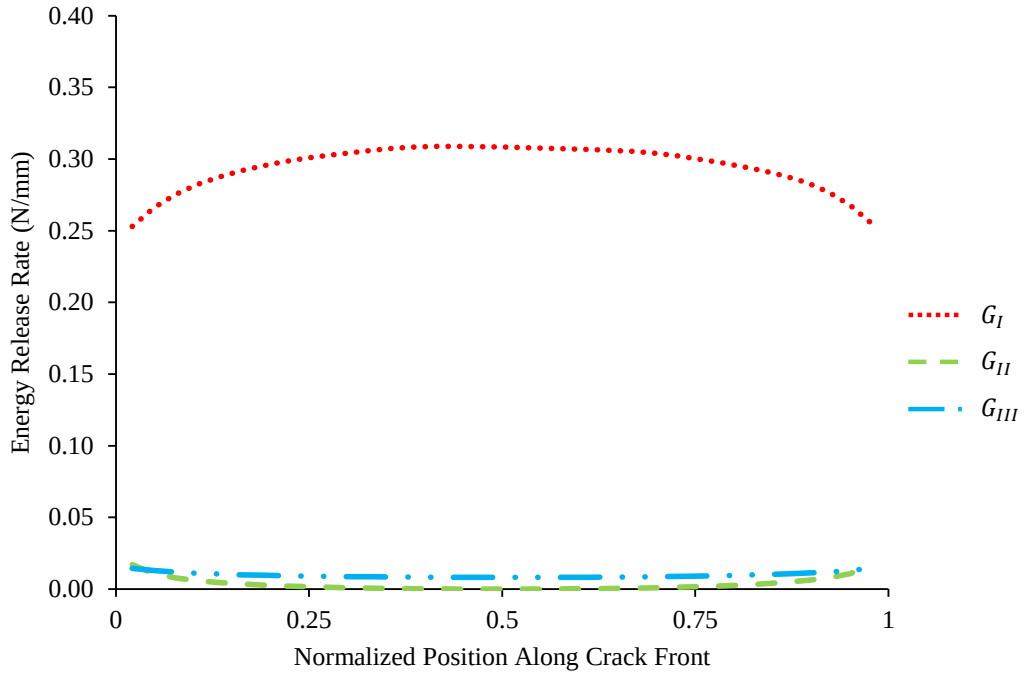

Figure 3.9. Initial mixed-mode energy release rate distributions for the angled-crack specimen.

The simulation successfully obtained stable crack front configurations for each of the applied displacement increments, but required the use of an artificial smoothing approach to suppress "factory-roof" formation along the crack front, as described below. The average energy release rate residual of the stable configurations compared to the critical value was approximately 3.2%, well within the functional tolerance. The unique and tortuous crack front geometry of this growth simulation required more iterations than the simulation in Section 3.4.1. On average, approximately 9 crack-front extension iterations were needed per crack-extension increment. Figure 3.10 shows selected configurations of the crack front evolution for various displacement increments. As in Section 3.4.1, the simulation results were qualitatively verified with a quasi-static, FRANC3D, prescribed crack growth analysis. As expected, the initially angled crack front advanced such that the path rotated back to a planar, mode I configuration. Figure 3.11 shows the stable crack geometry for step 5, demonstrating the capacity of the simulation technique to capture both the non-planar behavior of the crack evolution, and also the subtle in-plane curvature along the front.

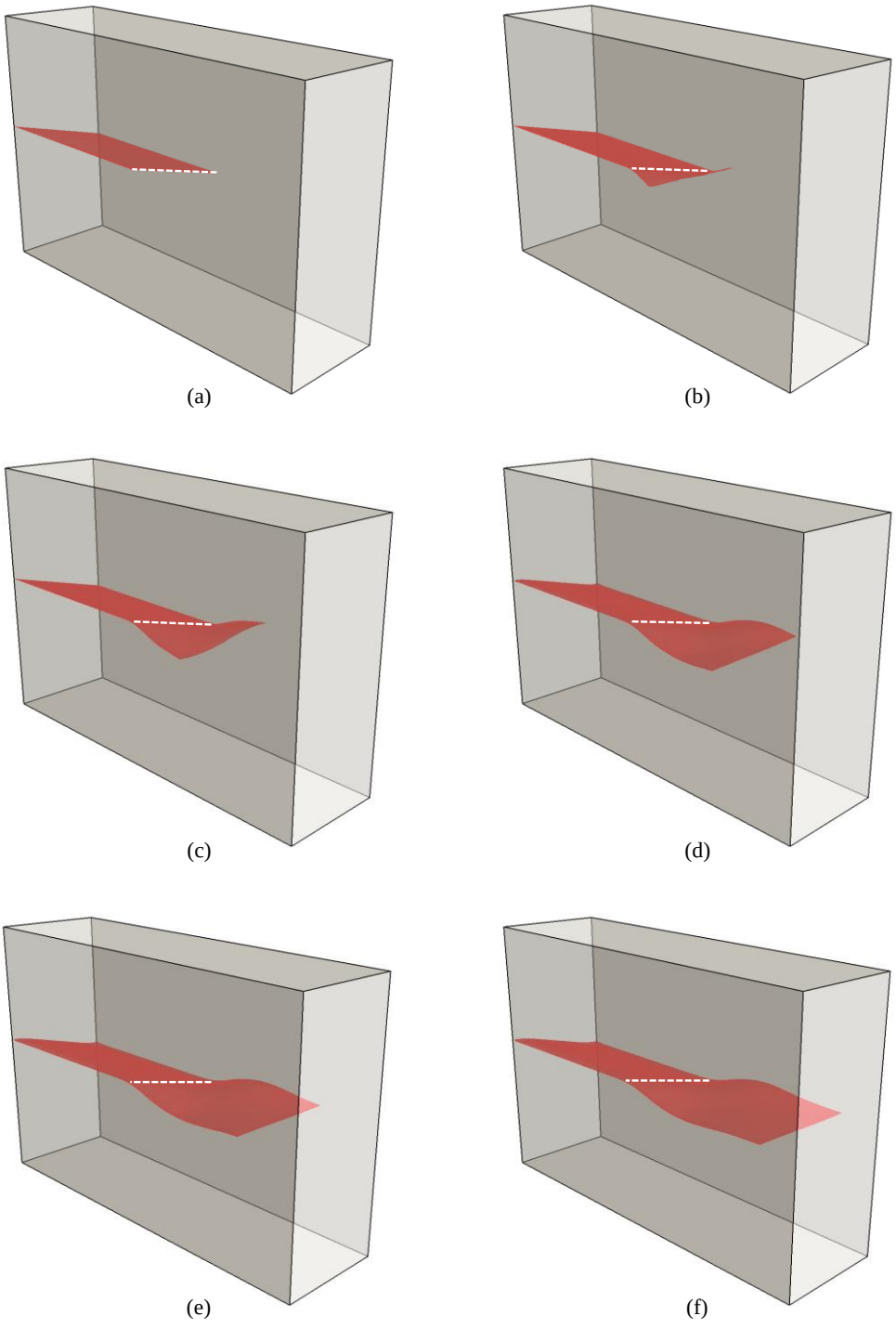

Figure 3.10. (a) Initial crack-front geometry for the angled-crack specimen. (b)-(f) Predicted geometries for the evolving crack front after displacement increments 2, 4, 6, 8, and 14, respectively.

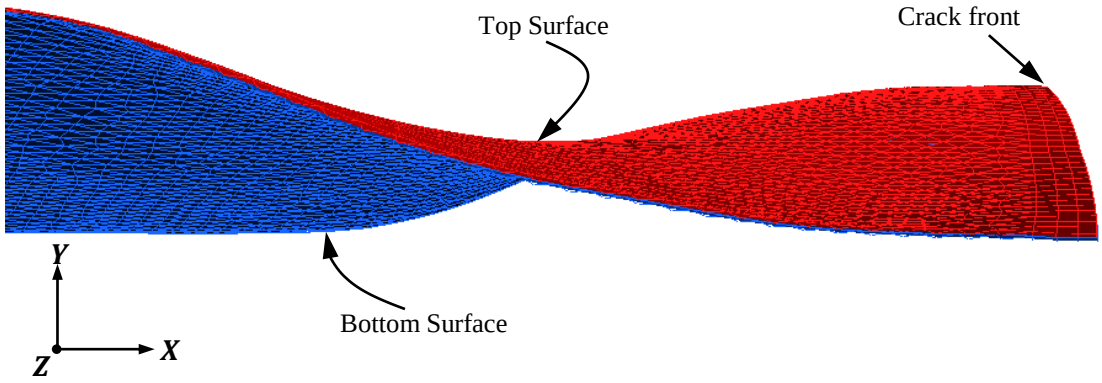

Figure 3.11. Side view of crack geometry in the angled-crack specimen at the stable configuration for applied displacement increment 5. The top surface is highlighted in red, while the bottom surface is in blue. Note the slight curvature of the front in the *X*-*Z* plane.

As mentioned previously and shown in Figure 3.12, the simulation scheme was also able to generate and predict the early stage of "factory-roof" formation along the crack front profile [102] for several iterations of crack growth. This unique behavior associated with mode III crack growth has been observed experimentally [103,104] and discussed in analytical/modeling approaches [105–107]. References [101,108] show "factory-roof" formation in angled, three-point bend specimens that have similar growth behavior to the example presented here. Figure 3.12 displays the progression and developing "factory-roof" profile in the current simulation.

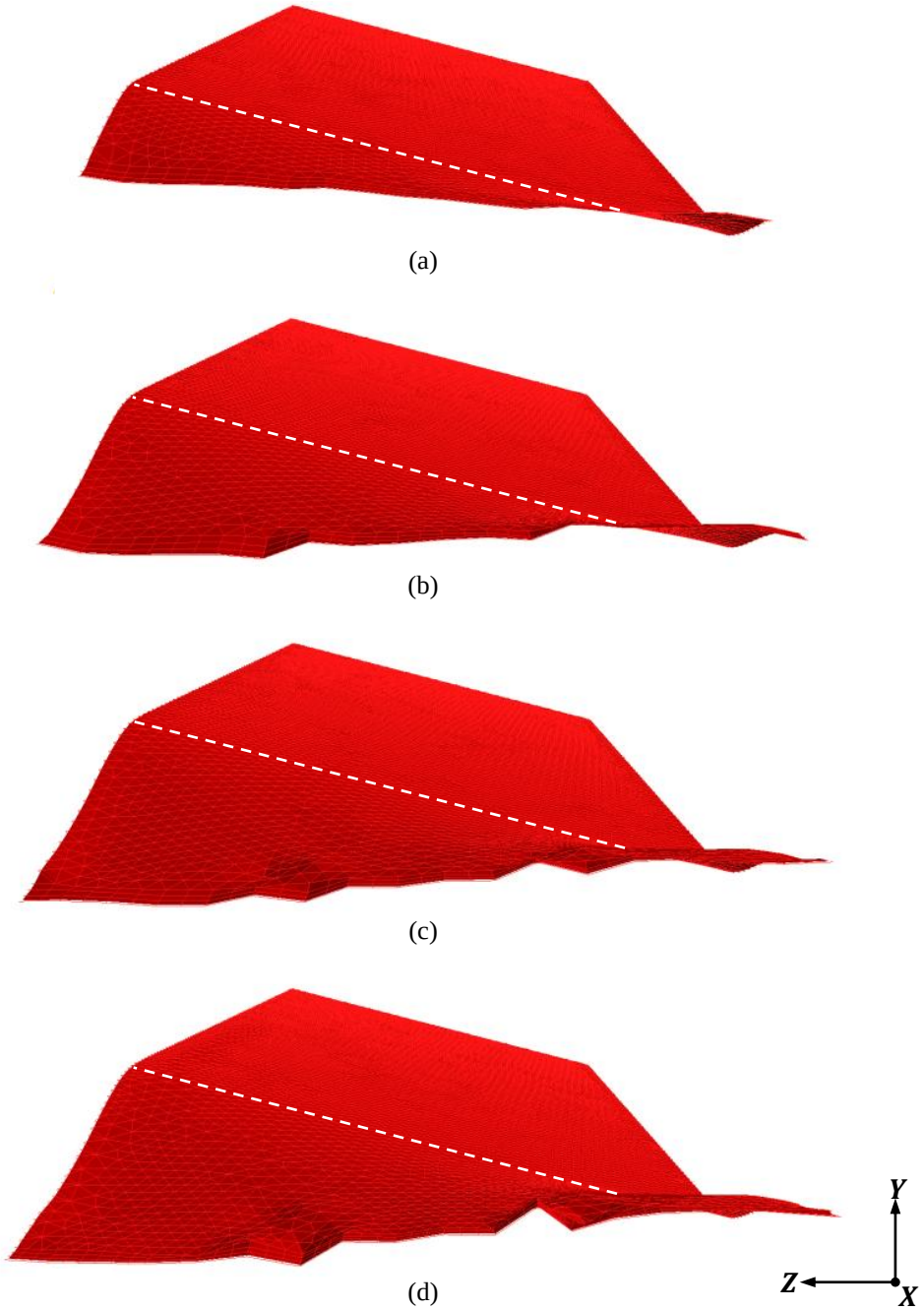

Figure 3.12. "Factory-roof" formation along advancing crack front: (a) increment 2 stable configuration, (b) increment 3 stable configuration, (c) increment 4 - iteration 1, unstable, (d) increment 4 - iteration 3, unstable. The initial crack front position is highlighted in white.

The energy-based growth formulation in conjunction with the maximum energy release rate trajectory criterion was able to predict the physical phenomenon of "factory-roof" onset. The expected subsequent breakdown of the entire crack front into individual, small, localized mode I cracks was unattainable in the numerical simulation due to current limitations in crack representation capabilities. Instead, a geometric smoothing approach was applied to the front to circumvent issues associated with numerically capturing the formation and ultimate coalescence of these local, mode I cracks. The smoothing approach allowed the simulation to proceed directly to the coalesced, final stage of crack growth so that the ensuing evolution into the single mode I crack configuration could be achieved.

3.5 Discussion

The basis-function modifications to the energy-based formulation and the new GVCE method had two primary objectives in terms of simulating non-planar crack growth. The first deals with the compounding complexity of crack representation, fracture mechanics calculations, and crack growth predictions. All three components have certain numerical sensitivities that become interrelated. For example, the nominally insignificant undulations in energy release rate distributions along a crack front transpire through the growth formulation to create instabilities in the calculated crack front extensions. These can accumulate and render the crack growth predictions nonsensical. The basis-function approach offers an opportunity to mitigate this

situation by generating an expression to govern crack growth predictions. The basis functions provide "insulation" against numerical noise by restricting the extensions along the front to be generally smooth and continuous.

The second objective of the basis-function approach is to stabilize the variation of energy release rate calculation using the GVCE method. The term of interest within Eq. (3.9) is the variation of nodal displacement, $\frac{\delta u}{\delta a_j}$, which is obtained essentially by applying a local virtual point perturbation at each position along the crack front then executing a finite element solution. Similar to applying a nodal force in a standard finite element model, an area of distortion is created near the location of the applied virtual perturbation. The GVCE approach effectively distributes the virtual perturbations, relieving the local distortion influence on the variation of nodal displacement calculations, and ultimately on the variation of energy release rate. An added benefit of the GVCE approach is the increase in computational efficiency. The size of the overall system of equations to predict crack extensions is reduced requiring the solution to fewer unknowns than the local, point-by-point approach.

The basis-function approach was successfully implemented within the energy-based formulation described in Chapter 1 [67], providing accurate calculations to predict non-planar crack front evolution. It is important to note that the selection of functions is arbitrary. In the examples presented, a third-order polynomial was used. The basis-function approach is a coarsening measure to obtain realistic crack front predictions. In some cases, such as partial growth and the emergence of local instabilities along the crack front, the fine adjustments characteristic of the point-by-point approach of Chapter 1 might be employed. Opportunities exist within the basis-

function approach to improve simulation fidelity by incorporating an adaptive scheme that progressively adds higher-order terms to the governing crack extension function until a converged shape is achieved. Additional refinement can be made by subdividing the crack front into multiple segments and determining separate crack extension functions for each segment.

Another aspect of the simulation technique that warrants further discussion is the incremental-iterative approach. The simulation relies on the user to prescribe a load increment. The chosen load increment induces a crack extension. The crack extension is calculated and the geometry of the crack front is updated. A new finite element mesh is generated with a new crack-front template. In the current implementation, the user has control over the applied load increment and the crack-front template meshing parameters. With the applied load increment indirectly influencing the magnitude of crack front extensions, the crack front meshing parameters must be selected to adhere to the predicted growth. For example, since the updated crack geometry proceeds directly from the previous discretization, care must be taken to avoid topological issues when re-meshing volumes with overlapping or poorly defined intersections. These concerns can be alleviated with more sophisticated methods for tracking crack geometries and re-meshing techniques.

The scope of the current implementation is limited to stable crack growth situations. This directly motivated the selection of the example simulations. However, this is not a restriction on the crack growth formulation or simulation technique. Manipulating Eq. (3.6) by setting $G_i^0 = G_{ic}$ generates the energy-balance used to calculate crack extensions:

$$\frac{\delta G_i}{\delta P} \odot \Delta P_i + \frac{\delta G_i}{\delta a_j} \Delta a_j = 0. \tag{3.15}$$

It is obvious that both $\frac{\delta G_i}{\delta P}$, and Δa_j are positive since increasing load increases energy, and crack fronts cannot shrink, i.e. have negative growth. This leaves the load increment term, ΔP_i, and the variation of energy release rate, $\frac{\delta G_i}{\delta a_j}$. In a stable crack growth problem, the variation of energy release rate is inherently negative, meaning as the crack advances the energy release rate decreases. To maintain the energy balance of Eq. (3.15), this requires ΔP_i to be positive. Alternatively, in an unstable crack growth problem, where the variation in energy release rate is positive, ΔP_i must be negative to preserve Eq. (3.15). Therefore, to simulate unstable crack growth with the energy-based formulation, load must be incrementally removed from the system. With this understanding of the simulation framework, the capability can be fully generalized, predicting arbitrary crack front evolution for stable/unstable and planar/non-planar problems. Note that this argument extends to the basis-function form of the energy-balance, Eq. (3.13), but is more robust using Eq. (3.15), which directly relates to crack extensions, rather than the coefficients of a crack extension function.

3.6 Conclusions

This chapter extends the new, energy-based growth formulation and implementation developed in Chapter 1 [67], to simulate arbitrary crack growth of non-planar, 3-D cracks. The generalized simulation technique employs a unique basis-function approach to determine an explicit expression to govern crack front extensions. The basis-function approach seeks to mitigate the influence of numerical noise on non-planar crack growth predictions that was observed when using the point-by-point approach in Chapter 1.

The novelty of this generalized simulation technique lies in its simple energetic approach. The formulation stems from an energy balance, weighing the energy available due to load input and shape change versus a critical fracture toughness value. The salient feature of the technique is its ability to explicitly predict crack evolution, where other methods often rely on numerical artifacts, such as the mesh, to direct crack growth or use ad-hoc prescribed extension increments. The explicit non-planar crack growth predictions described in this dissertation are made possible through the basis-function approach and global variation of energy release rate, which serves as a mechanics-based link that relates energy change to crack geometry change.

Two example simulations demonstrate the effectiveness of the basis-function simulation technique to capture mixed-mode, non-planar crack growth. The combination of the energy-based growth formulation and a trajectory criterion based on maximum energy release rate enable the prediction of general non-planar behavior,

while preserving local curvature and twisting behavior, evidenced by the “factory-roof” formation in the second simulation example.

Future work includes potential advancements to improve efficiency and optimization of computational resources. Validations of the simulation technique with experimental observations that precisely track the crack front geometry are required. Also being considered are improvements to rate of energy release rate calculations using various numerical integration schemes and alternative methods.

APPENDIX A

SYMMETRY NOTIONS FOR COUPLING MODE CANCELLATION AND CONTRIBUTION

For brevity, the expansion and derivation to demonstrate the symmetry effects on the modal-interaction coupling terms is shown for the cancellation of $G_{III/I}$. The same approach can be applied to verify the cancellation of the $G_{I/II}$ term and the additive contribution of $G_{II/III}$.

The expression for the mode III/I coupling term is:

$$G_{III/I}{}_i = -\frac{1}{\ell_i}\left(u_{III}{}^T \frac{\delta K}{\delta a_{i_L}} u_I\right). \tag{A.1}$$

The objective of this derivation is to show that with integration about a symmetric domain, there is a cancelation between the domain above the crack plane and the domain below the crack plane for the $G_{III/I}$ coupling term.

Without loss of generality, an arbitrary point involved in the integration above the crack plane, P_A, is selected with local displacements (u_1, u_2, u_3). Let the mirror point across the crack plane, P_B, according to Figure 2.2, have local displacements (v_1, v_2, v_3). The resulting mode III displacement vectors for P_A and P_B follow according to Section 2.2.2:

$$u_{A,III} = \frac{1}{2}\begin{Bmatrix} 0 \\ 0 \\ u_3 - v_3 \end{Bmatrix}, \tag{A.2}$$

$$u_{B,III} = \frac{1}{2}\begin{Bmatrix} 0 \\ 0 \\ v_3 - u_3 \end{Bmatrix}. \tag{A.3}$$

The decomposed mode I displacement vectors for P_A and P_B are:

$$u_{A,I} = \frac{1}{2}\begin{Bmatrix} u_1 + v_1 \\ u_2 - v_2 \\ u_3 + v_3 \end{Bmatrix}, \tag{A.4}$$

$$u_{B,I} = \frac{1}{2}\begin{Bmatrix} v_1 + u_1 \\ v_2 - u_2 \\ v_3 + u_3 \end{Bmatrix}. \tag{A.5}$$

The expression for the local stiffness variation in Eq. (A.1) is:

$$\frac{\delta K}{\delta a_i}_L = \int \left[\frac{\delta B^T}{\delta a_i} DB + B^T D \frac{\delta B}{\delta a_i} + \frac{\delta |J|}{\delta a_i} B^T DB \right] dV. \tag{A.6}$$

Let D be a standard isotropic finite-element constitutive matrix. To maintain symmetry, D is considered constant within the integration domain and across the crack plane. Note that this assumption breaks down when dealing with cracks at a bi-material interface. See Section 2.2.3 for comments concerning this loss of symmetry.

The variation of the strain-displacement matrix, $\frac{\delta B}{\delta a_i}$, is determined through the application of the virtual crack extensions. A more detailed formulation can be found in [36], but a general overview of the relevant expressions follows.

First, a virtual "strain-like" matrix, $\tilde{\varepsilon}$, is formed as a result of the virtual perturbations:

$$\tilde{\varepsilon} = J^{-1} \begin{Bmatrix} \partial N/\partial \xi^1 \\ \partial N/\partial \xi^2 \\ \partial N/\partial \xi^3 \end{Bmatrix} \lfloor \Delta_n^1 \quad \Delta_n^2 \quad \Delta_n^3 \rfloor, \tag{A.7}$$

where Δ_n are nodal values of the virtual crack front extensions in the local coordinate system, x_1, x_2, x_3, and $\partial N/\partial \xi$ represent the shape function derivatives in parametric space. The use of the local coordinate system results in $\Delta_n^2 = \Delta_n^3 = 0$ for the applied virtual extension. The simplified $\tilde{\varepsilon}$ matrix becomes:

$$\tilde{\varepsilon} = \begin{bmatrix} \tilde{\varepsilon}_{11} & 0 & 0 \\ \tilde{\varepsilon}_{21} & 0 & 0 \\ \tilde{\varepsilon}_{31} & 0 & 0 \end{bmatrix} = \begin{bmatrix} \lfloor \tilde{\varepsilon}_1 \rfloor \\ \lfloor \tilde{\varepsilon}_2 \rfloor \\ \lfloor \tilde{\varepsilon}_3 \rfloor \end{bmatrix}. \tag{A.8}$$

The variation of the strain-displacement matrix is then formed by:

$$\frac{\delta B}{\delta a} = -\begin{bmatrix} \lfloor \tilde{\varepsilon}_1 \rfloor & 0 & 0 \\ 0 & \lfloor \tilde{\varepsilon}_2 \rfloor & 0 \\ 0 & 0 & \lfloor \tilde{\varepsilon}_3 \rfloor \\ \lfloor \tilde{\varepsilon}_2 \rfloor & \lfloor \tilde{\varepsilon}_1 \rfloor & 0 \\ 0 & \lfloor \tilde{\varepsilon}_3 \rfloor & \lfloor \tilde{\varepsilon}_2 \rfloor \\ \lfloor \tilde{\varepsilon}_3 \rfloor & 0 & \lfloor \tilde{\varepsilon}_1 \rfloor \end{bmatrix} \begin{bmatrix} \frac{\partial N}{\partial x_1} & 0 & 0 \\ \frac{\partial N}{\partial x_2} & 0 & 0 \\ \frac{\partial N}{\partial x_3} & 0 & 0 \\ 0 & \frac{\partial N}{\partial x_1} & 0 \\ 0 & \frac{\partial N}{\partial x_2} & 0 \\ 0 & \frac{\partial N}{\partial x_3} & 0 \\ 0 & 0 & \frac{\partial N}{\partial x_1} \\ 0 & 0 & \frac{\partial N}{\partial x_2} \\ 0 & 0 & \frac{\partial N}{\partial x_3} \end{bmatrix} = \begin{bmatrix} \delta b_{11} & 0 & 0 \\ 0 & \delta b_{22} & 0 \\ 0 & 0 & \delta b_{33} \\ \delta b_{41} & \delta b_{42} & 0 \\ 0 & \delta b_{52} & \delta b_{53} \\ \delta b_{61} & 0 & \delta b_{63} \end{bmatrix}. \tag{A.9}$$

The traditional finite element strain-displacement matrix, B, takes on a similar form:

$$B = \begin{bmatrix} \frac{\partial N}{\partial x_1} & 0 & 0 \\ 0 & \frac{\partial N}{\partial x_2} & 0 \\ 0 & 0 & \frac{\partial N}{\partial x_3} \\ \frac{\partial N}{\partial x_2} & \frac{\partial N}{\partial x_1} & 0 \\ 0 & \frac{\partial N}{\partial x_3} & \frac{\partial N}{\partial x_2} \\ \frac{\partial N}{\partial x_3} & 0 & \frac{\partial N}{\partial x_1} \end{bmatrix} = \begin{bmatrix} b_{11} & 0 & 0 \\ 0 & b_{22} & 0 \\ 0 & 0 & b_{33} \\ b_{22} & b_{11} & 0 \\ 0 & b_{33} & b_{22} \\ b_{33} & 0 & b_{11} \end{bmatrix}. \tag{A.10}$$

Let Eqs. (A.9) and (A.10) represent the strain-displacement and variation of strain-displacement for point P_A, and now be denoted as $\frac{\delta B}{\delta a_A}$ and B_A. Based on symmetry, the strain-displacement expressions for point P_B, relative to the Eqs. (A.9) and (A.10) become:

$$\frac{\delta B}{\delta a_B} = \begin{bmatrix} \delta b_{11} & 0 & 0 \\ 0 & -\delta b_{22} & 0 \\ 0 & 0 & \delta b_{33} \\ -\delta b_{41} & \delta b_{42} & 0 \\ 0 & \delta b_{52} & -\delta b_{53} \\ \delta b_{61} & 0 & \delta b_{63} \end{bmatrix}, \tag{A.9}$$

$$B_B = \begin{bmatrix} b_{11} & 0 & 0 \\ 0 & -b_{22} & 0 \\ 0 & 0 & b_{33} \\ -b_{22} & b_{11} & 0 \\ 0 & b_{33} & -b_{22} \\ b_{33} & 0 & b_{11} \end{bmatrix}. \tag{A.10}$$

Two contributing expressions for $G_{III/I}$ are now formed for above and below the crack plane. Substituting the equations for the separate instances, point P_A and point P_B, into Eq. (A.1) leads to the following two equations:

$$G_{A,III/I} = -\frac{1}{\ell}\left(u_{A,III}^T \int \left[\frac{\delta B}{\delta a_A}^T D B_A + B_A^T D \frac{\delta B}{\delta a_A} + \frac{\delta |J|}{\delta a} B_A^T D B_A\right] dV \, u_{A,I}\right), \tag{A.11}$$

$$G_{B,III/I} = -\frac{1}{\ell}\left(u_{B,III}^T \int \left[\frac{\delta B}{\delta a_B}^T D B_B + B_B^T D \frac{\delta B}{\delta a_B} + \frac{\delta |J|}{\delta a} B_B^T D B_B\right] dV \, u_{B,I}\right), \tag{A.12}$$

where $G_{A,III/I}$ represents the coupled energy above the crack plane at P_A, and $G_{B,III/I}$ represents the symmetric coupled energy below the crack plane at P_B.

Dropping the constant terms ℓ and $\frac{\delta|J|}{\delta a}$, and moving the modal displacements inside the integral, the updated integrands, denoted by the * superscript, can be evaluated:

$$G_{A,III/I}{}^{*} = u_{A,III}^{T}\left(\frac{\delta B^{T}}{\delta a_A} DB_A + B_A^T D \frac{\delta B}{\delta a_A} + B_A^T D B_A\right) u_{A,I}, \tag{A.13}$$

$$G_{B,III/I}{}^{*} = u_{B,III}^{T}\left(\frac{\delta B^{T}}{\delta a_B} DB_B + B_B^T D \frac{\delta B}{\delta a_B} + B_B^T D B_B\right) u_{B,I}. \tag{A.14}$$

The resulting algebraic expansions and matrix multiplication leads to expressions for $G_{A,III/I}{}^{*}$, and $G_{B,III/I}{}^{*}$ that cancel term by term (not shown for brevity). This analytic exercise demonstrates the symmetry cancellation effect found in the mode III/I coupling term that leads to $G_{III/I} = 0$. The approach can be repeated with the $G_{I/II}$, and $G_{II/III}$ terms to verify their respective cancellation and additive contribution to the overall energy release rate. These symmetric notions have been further verified with numerical investigations.

APPENDIX B

COUPLING MODE $G_{II/III}$ CONTRIBUTION TO MODE III ENERGY RELEASE RATE

The expression for the $G_{II/III}$ interaction coupling term follows:

$$G_{II/III_i} = -\frac{1}{\ell_i}\left(u_{II}{}^T \frac{\delta K}{\delta a_{i_L}} u_{III}\right), \tag{B.1}$$

where ℓ_i is an effective normalizing length for a 3-D virtual extension, u_{II} are the mode II displacements, u_{III} are the mode III displacements, and $\frac{\delta K}{\delta a_{i_L}}$ is the local crack-front coordinate stiffness variation.

The pertinent modal displacements are defined by the following equations:

$$u_{II} = \frac{1}{2}\begin{Bmatrix} u_1 - u_1' \\ u_2 + u_2' \\ 0 \end{Bmatrix}, \tag{B.2}$$

$$u_{III} = \frac{1}{2}\begin{Bmatrix} 0 \\ 0 \\ u_3 - u_3' \end{Bmatrix}, \tag{B.3}$$

The stiffness derivative is formed from the following integral expression over the volume of an element experiencing a virtual extension:

$$\frac{\delta K}{\delta a_i}_L = \int \left[\frac{\delta B^T}{\delta a_i} DB + B^T D \frac{\delta B}{\delta a_i} + \frac{\delta |J|}{\delta a_i} B^T DB\right] dV, \tag{B.4}$$

where D is the constitutive matrix, B is the strain-displacement matrix and J is the Jacobian of the traditional finite element formulation. Substituting Eq. (B.4) into Eq. (B.1) leads to the following:

$$G_{II/III}{}_i = -\frac{1}{\ell_i}\left(u_{II}^T \left(\int \left[\frac{\delta B^T}{\delta a_i} DB + B^T D \frac{\delta B}{\delta a_i} + \frac{\delta |J|}{\delta a_i} B^T DB\right] dV\right) u_{III}\right). \tag{B.5}$$

With the subsequent expansion, the mode II/III interaction coupling term becomes:

$$\begin{aligned} G_{II/III}{}_i = &-\frac{1}{\ell_i}\left(u_{II}^T \int \frac{\delta B^T}{\delta a_i} DB dV\, u_{III}\right) - \frac{1}{\ell_i}\left(u_{II}^T \int B^T D \frac{\delta B}{\delta a_i} dV\, u_{III}\right) - \\ &\frac{1}{\ell_i}\left(u_{II}^T \int \frac{\delta |J|}{\delta a_i} B^T DB dV\, u_{III}\right). \end{aligned} \tag{B.6}$$

The variation of the strain-displacement matrix with respect to a virtual crack extension, $\frac{\delta B}{\delta a_i}$, is formed in Appendix A, Eqs. (A.7) – (A.10).

To determine the kinematics associated with the $G_{II/III}$ coupling term a single point is investigated without loss of generality, similar to the approach taken in Appendix A. Also, Eq. (B.6) is simplified by dropping the integration and constants $\frac{1}{\ell_i}$ and $\frac{\delta |J|}{\delta a_i}$:

$$G_{II/III} = -\left(u_{II}^T \frac{\delta B^T}{\delta a} DBu_{III}\right) - \left(u_{II}^T B^T D \frac{\delta B}{\delta a} u_{III}\right) - (u_{II}^T B^T DBu_{III}). \quad \text{(B.7)}$$

Collecting strains, virtual strain rates, stresses, and virtual stress rates leads to the following expression:

$$G_{II/III} = -\left(\frac{\delta {\varepsilon_{II}}^T}{\delta a} \sigma_{III}\right) - \left({\varepsilon_{II}}^T \frac{\delta \sigma_{III}}{\delta a}\right) - ({\varepsilon_{II}}^T \sigma_{III}). \quad \text{(B.8)}$$

Assuming plane strain conditions (i.e. $\varepsilon_3 = \delta\varepsilon_3 = 0$), the formulations for the modal strains, virtual strain rates, modal stresses and virtual stress rates in Eq. (B.8) can be determined using Eqs. (B.2) and (B.3). The expressions for ε_{II}, $\frac{\delta \varepsilon_{II}}{\delta a}$, σ_{III} and $\frac{\delta \sigma_{III}}{\delta a}$ become:

$$\varepsilon_{II} = Bu_{II} = \frac{1}{2}\begin{bmatrix} b_{11} & 0 & 0 \\ 0 & b_{22} & 0 \\ 0 & 0 & b_{33} \\ b_{41} & b_{42} & 0 \\ 0 & b_{52} & b_{53} \\ b_{61} & 0 & b_{63} \end{bmatrix} \begin{Bmatrix} u_1 - u_1' \\ u_2 + u_2' \\ 0 \end{Bmatrix} = \begin{Bmatrix} \varepsilon_1 \\ \varepsilon_2 \\ 0 \\ \varepsilon_{12} \\ \varepsilon_{23} \\ \varepsilon_{31} \end{Bmatrix}, \quad \text{(B.9)}$$

$$\frac{\delta \varepsilon_{II}}{\delta a} = \frac{\delta B}{\delta a} u_{II} = \frac{1}{2}\begin{bmatrix} \delta b_{11} & 0 & 0 \\ 0 & \delta b_{22} & 0 \\ 0 & 0 & \delta b_{33} \\ \delta b_{41} & \delta b_{42} & 0 \\ 0 & \delta b_{52} & \delta b_{53} \\ \delta b_{61} & 0 & \delta b_{63} \end{bmatrix} \begin{Bmatrix} u_1 - u_1' \\ u_2 + u_2' \\ 0 \end{Bmatrix} = \begin{Bmatrix} \delta\varepsilon_1 \\ \delta\varepsilon_2 \\ 0 \\ \delta\varepsilon_{12} \\ \delta\varepsilon_{23} \\ \delta\varepsilon_{31} \end{Bmatrix}, \quad \text{(B.10)}$$

$$\sigma_{III} = DBu_{III} = \frac{1}{2}D\begin{bmatrix} b_{11} & 0 & 0 \\ 0 & b_{22} & 0 \\ 0 & 0 & b_{33} \\ b_{41} & b_{42} & 0 \\ 0 & b_{52} & b_{53} \\ b_{61} & 0 & b_{63} \end{bmatrix}\begin{Bmatrix} 0 \\ 0 \\ u_3 - u_3' \end{Bmatrix} = \begin{Bmatrix} 0 \\ 0 \\ 0 \\ 0 \\ \sigma_{23} \\ \sigma_{31} \end{Bmatrix}, \tag{B.11}$$

$$\frac{\delta\sigma_{III}}{\delta a} = D\frac{\delta B}{\delta a}u_{III} = \frac{1}{2}D\begin{bmatrix} \delta b_{11} & 0 & 0 \\ 0 & \delta b_{22} & 0 \\ 0 & 0 & \delta b_{33} \\ \delta b_{41} & \delta b_{42} & 0 \\ 0 & \delta b_{52} & \delta b_{53} \\ \delta b_{61} & 0 & \delta b_{63} \end{bmatrix}\begin{Bmatrix} 0 \\ 0 \\ u_3 - u_3' \end{Bmatrix} = \begin{Bmatrix} 0 \\ 0 \\ 0 \\ 0 \\ \delta\sigma_{23} \\ \delta\sigma_{31} \end{Bmatrix}. \tag{B.12}$$

For this exercise, let D represent an isotropic constitutive matrix. Substituting Eqs. (B.9) – (B.12) into Eq. (B.8) and evaluating the vector-vector multiplication reveals the only non-zero contributions to $G_{II/III}$ originate from the out-of-plane shear components of stress, strain and their rates. For plane strain, by definition, the out-of-plane shear stresses are zero for mode I and mode II energy release rates. Therefore, any contribution to the total energy release rate from $G_{II/III}$ is a factor of the mode III energy release rate.

APPENDIX C

FINITE ELEMENT MESHES FOR CHAPTER 2 NUMERICAL EXAMPLES

Figure C.1 – Figure C.5 depict global and local crack front images of the finite element meshes used in the numerical examples of Section 2.4.

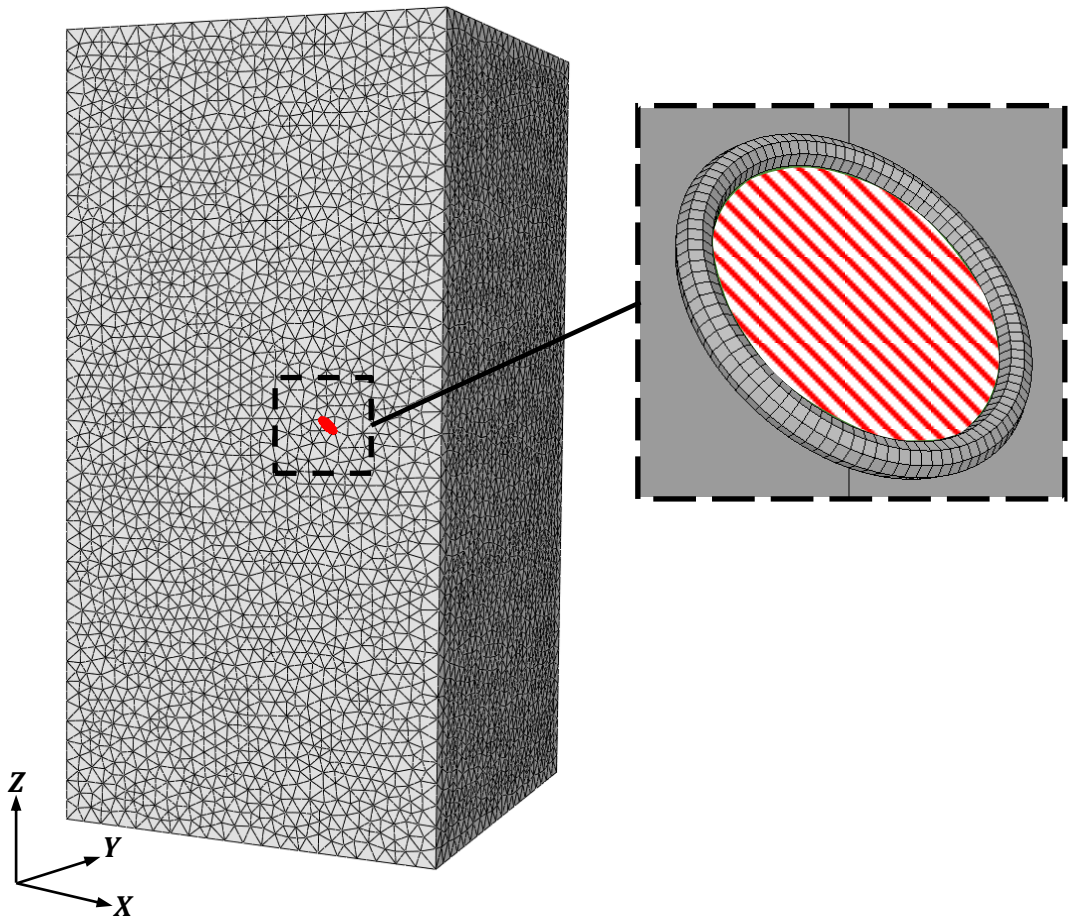

Figure C.1. Global finite element mesh and local crack front template for the inclined penny crack specimen.

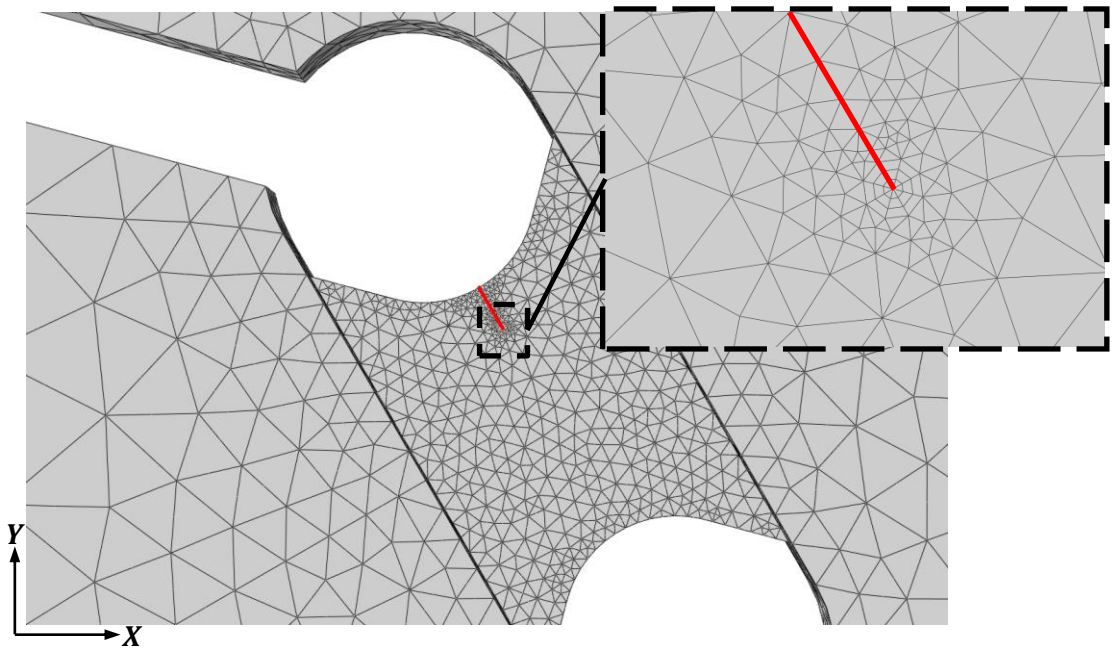

Figure C.2. Global finite element mesh and local crack front view for the Arcan fracture specimen.

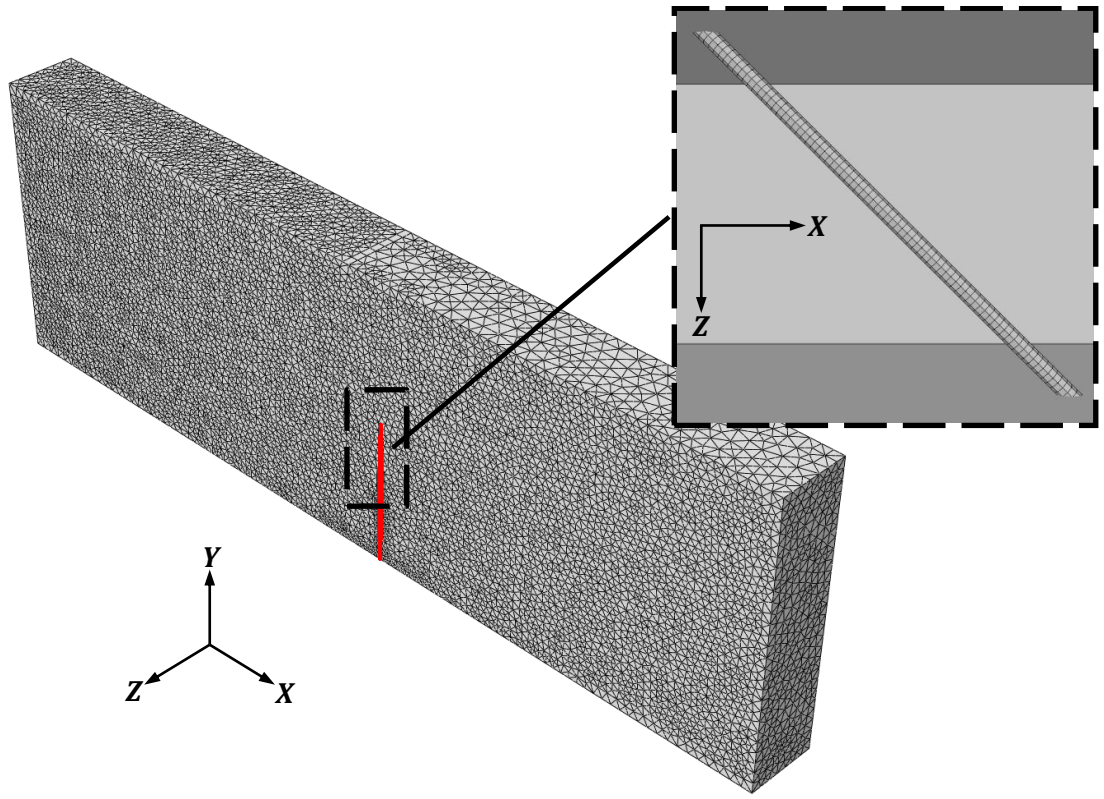

Figure C.3. Global finite element mesh and local crack front template for the angled-crack three-point bend specimen.

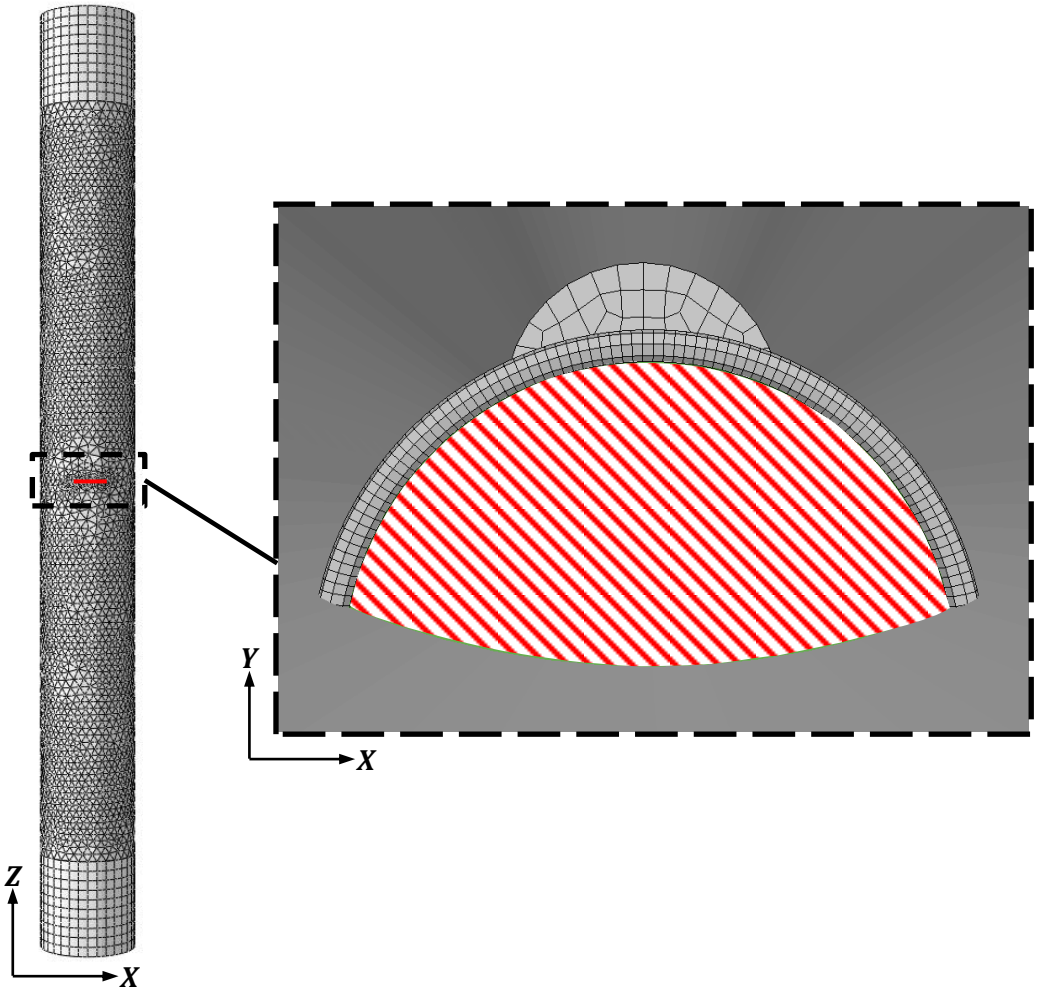

Figure C.4. Global finite element mesh and local crack front template for the surface-cracked cylinder specimen.

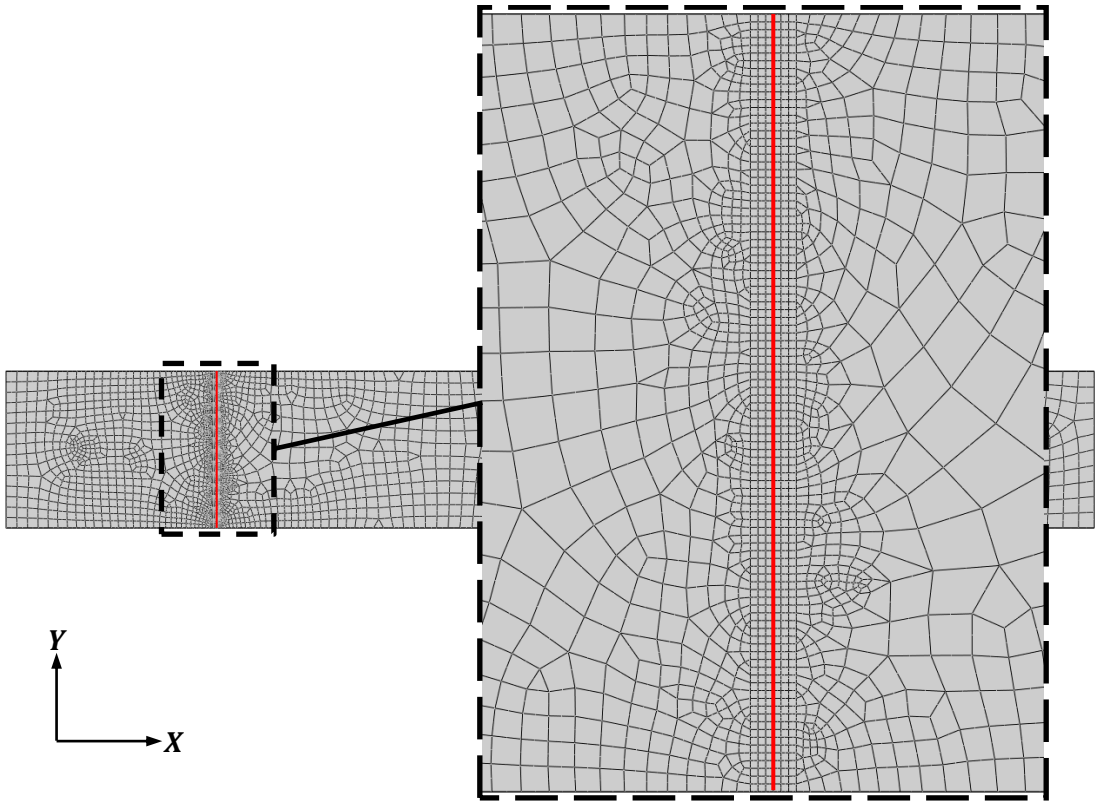

Figure C.5. Global finite element mesh and local crack front view for the single leg bending specimen.

APPENDIX D

ENERGY RELEASE RATE DISTRIBUTION COMPARISON FOR AN INCLINED PENNY CRACK

Figure D.1 – Figure D.4 show the mode I, II, III, and total energy release rate distribution comparisons, respectively, for the inclined penny crack described in Section 2.4.1. The plots compare the VCE mixed-mode energy release rate results against the analytical reference solution [75]. Figure D.5 shows the point-by-point percent difference between the VCE and analytical mixed-mode energy release rate distributions.

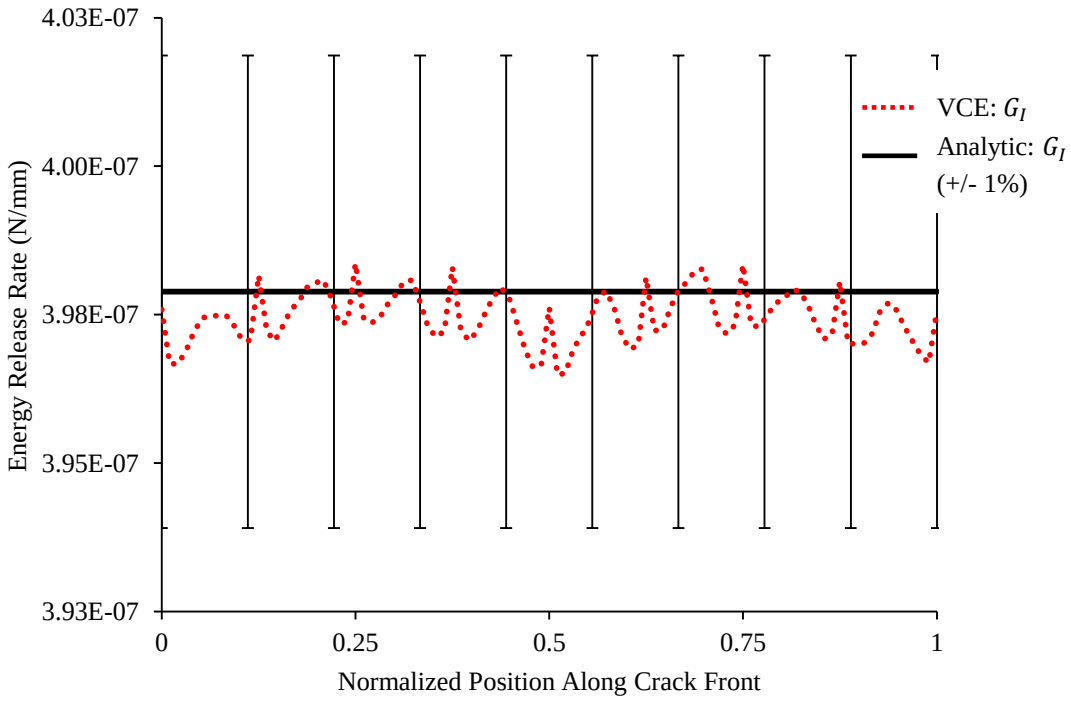

Figure D.1. Mode I energy release rate distribution comparison between the VCE method and analytical reference solution (+/- 1% error bars) for the inclined penny-crack specimen.

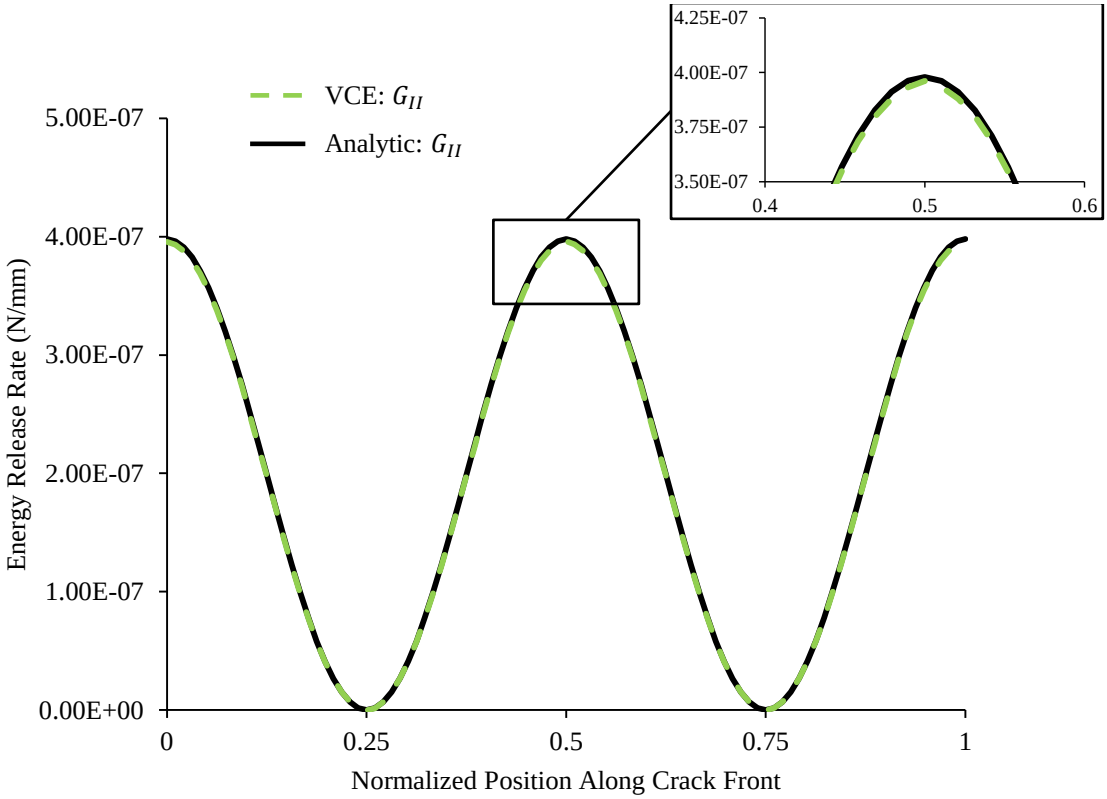

Figure D.2. Mode II energy release rate distribution comparison between the VCE method and analytical reference solution for the inclined penny-crack specimen.

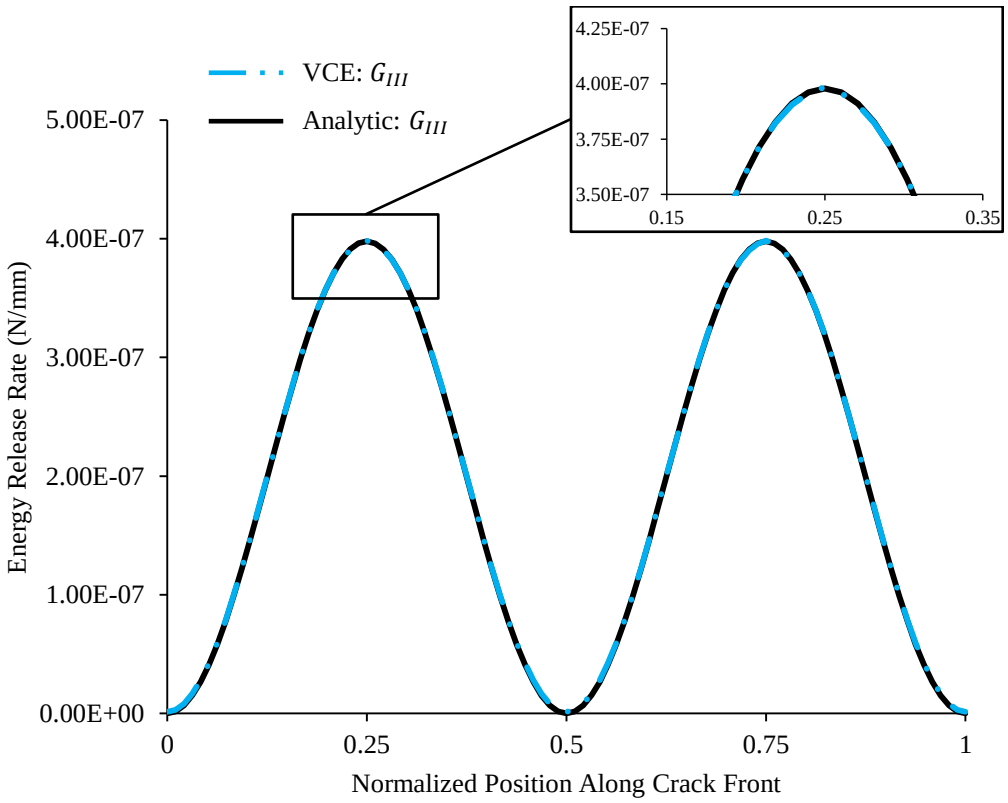

Figure D.3. Mode III energy release rate distribution comparison between the VCE method and analytical reference solution for the inclined penny-crack specimen.

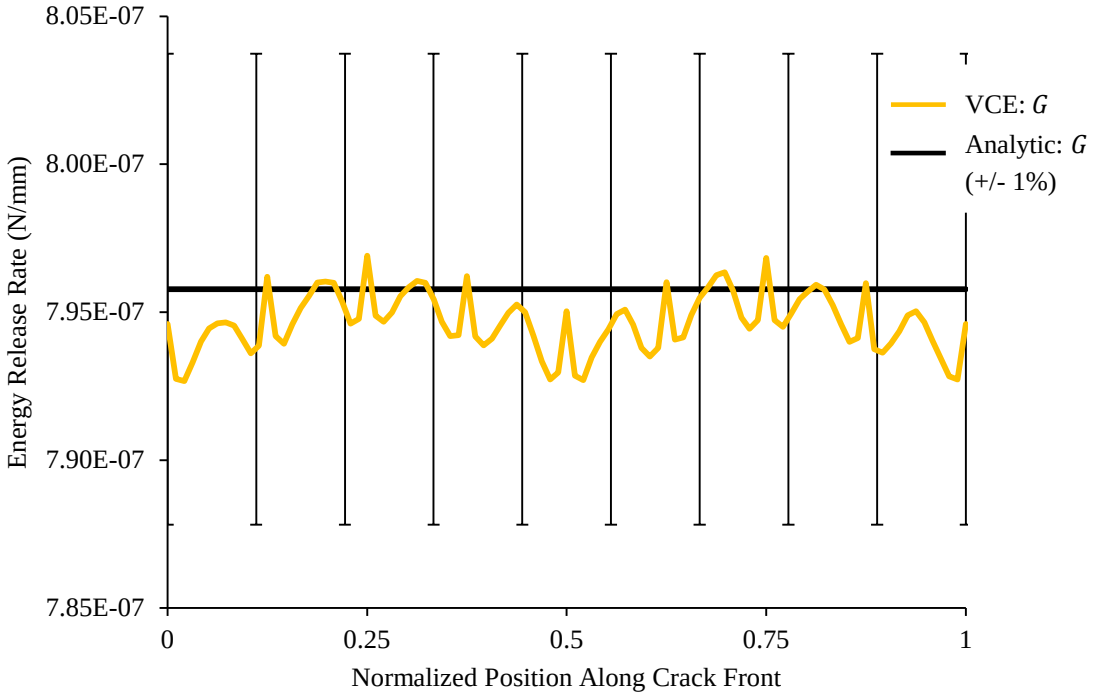

Figure D.4. Total energy release rate distribution comparison between the VCE method and analytical reference solution (+/- 1% error bars) for the inclined penny-crack specimen.

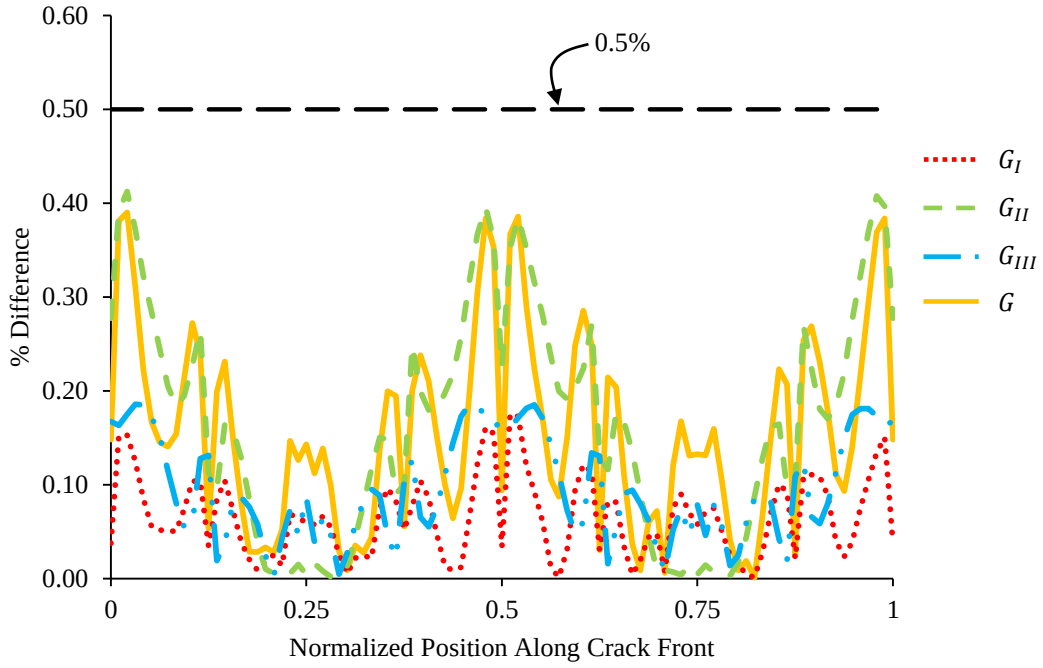

Figure D.5. Percent difference comparison between the VCE calculated energy release rates and the analytical reference solution for the inclined penny-crack specimen.

REFERENCES

[1] Ingraffea AR. Computational Fracture Mechanics. In: Stein E, de Borst R, Hughes T, editors. Encycl. Comput. Mech. Vol. 2, John Wiley and Sons; 2008.

[2] Rashid YR. Ultimate Strength Analysis of Prestressed Concrete Pressure Vessels. Nucl Eng Des 1968;7:334–44.

[3] Krajcinovic D. Damage Mechanics. Mech Mater 1989;8:117–97.

[4] Beissel SR, Johnson GR, Popelar CH. An element-failure algorithm for dynamic crack propagation in general directions. Eng Fract Mech 1998;61:407–25.

[5] De Borst R. Damage, Material Instabilities, and Failure. In: Stein E, de Borst R, Hughes T, editors. Encycl. Comput. Mech. Vol. 2, John Wiley and Sons; 2008.

[6] Needleman A, Tvergaard V. Mesh effects in the analysis of dynamic ductile crack growth. Eng Fract Mech 1994;47:75–91.

[7] Comi C, Mariani S, Perego U. An extended FE strategy for transition from continuum damage to mode I cohesive crack propagation. Int J Numer Anal Methods Geomech 2007;31:213–38.

[8] Belytschko T, Black T. Elastic crack growth in finite elements with minimal remeshing. Int J Numer Methods Eng 1999;45:601–20.

[9] Moes N, Dolbow J, Belytschko T. A finite element method for crack growth without remeshing. Int J Numer Methods Eng 1999;46:131–50.

[10] Belytschko T, Gracie R, Ventura G. A review of extended/generalized finite element methods for material modeling. Model Simul Mater Sci Eng 2009;17.

[11] Areias PMA, Belytschko T. Analysis of three-dimensional crack initiation and propagation using the extended finite element method. Int J Numer Methods Eng 2005;63:760–88.

[12] Moes N, Belytschko T. Extended finite element method for cohesive crack growth. Eng Fract Mechancis 2002;69:813–33.

[13] Huang R, Sukumar N, Prévost J-H. Modeling quasi-static crack growth with the extended finite element method Part II: Numerical applications. Int J Solids Struct 2003;40:7539–52.

[14] Sukumar N, Chopp DL, Moran B. Extended finite element method and fast marching method for three-dimensional fatigue crack propagation. Eng Fract Mech 2003;70:29–48.

[15] Dugdale DS. Yielding of Steel Sheets Containing Slits. J Mech Phys Solids 1960;8:100–4.

[16] Barenblatt GI. The mathematical theory of equilibrium cracks formed in brittle fracture. Adv Appl Mechancis 1962;7:55–129.

[17] Roy YA, Dodds RH. Simulation of ductile crack growth in thin aluminum panels using 3-D surface cohesive elements. Int J Fract 2001;110:21–45.

[18] Khoei AR, Moslemi H, Sharifi M. Three-dimensional cohesive fracture modeling of non-planar crack growth using adaptive FE technique. Int J Solids Struct 2012;49:2334–48.

[19] Lo CY, Nakamura T, Kushner a. Computational analysis of dynamic crack propagation along a bimaterial interface. Int J Solids Struct 1994;31:145–68.

[20] Gullerud AS, Dodds Jr. RH, Hampton RW, Dawicke DS. Three-dimensional modeling of ductile crack growth in thin sheet metals: computational aspects and validation. Eng Fract Mech 1999;63:347–74.

[21] Krueger R. An Approach to Assess Delamination Propagation Simulation Capabilities in Commercial Finite Element Codes. NASA/TM-2008-215123 2008.

[22] Park K, Paulino GH, Celes W, Espinha R. Adaptive mesh refinement and coarsening for cohesive zone modeling of dynamic fracture. Int J Numer Methods Eng 2012;92:1–35.

[23] Shephard MS, Yehia NAB, Burd GS, Weidner TJ. Automatic Crack Propagation Tracking. Comput Struct 1985;20:211–23.

[24] Wawrzynek PA, Ingraffea AR. An interactive approach to local remeshing around a propagating crack. Finite Elem Anal Des 1989;5:87–96.

[25] Carter BJ, Wawrzynek PA, Ingraffea AR. Automated 3-D crack growth simulation. Int J Numer Methods Eng 2000;47:229–53.

[26] Carter BJ, Schenck EC, Wawrzynek PA, Ingraffea AR, Barlow KW. Three-dimensional simulation of fretting crack nucleation and growth. Eng Fract Mech 2012;96:447–60.

[27] Hwang CG, Ingraffea AR. Shape prediction and stability analysis of mode-I planar cracks. Eng Fract Mech 2004;71:1751–77.

[28] Wimmer G, Pettermann HE. Numerical Simulations of Progressive Growth of Delaminations with Curved Fronts. 2nd ECCOMAS Themat. Conf. Mech. Response Compos., Imperial College, London, UK: 2009, p. 1–3.

[29] Dixon J, Pook L. Stress intensity factors calculated generally by the finite element technique. Nature 1969;224:166–7.

[30] Watwood Jr VB. The finite element method for prediction of crack behavior. Nucl Eng Des 1969;11:323–32.

[31] Hellen TK. On the method of virtual crack extensions. Int J Numer Methods Eng 1975;9:187–207.

[32] Parks DM. A stiffness derivative finite element technique for determination of crack tip stress intensity factors. Int J Fract 1974;10:487–502.

[33] Haber RB, Koh HM. Explicit expressions for energy release rates using virtual crack extensions. Int J Numer Methods Eng 1985;21:301–15.

[34] Lin SC, Abel JF. Variational approach for a new direct-integration form of the virtual crack extension method. Int J Fract 1988;38:217–35.

[35] Hwang CG, Wawrzynek PA, Tayebi AK, Ingraffea AR. On the virtual crack extension method for calculation of the rates of energy release rate. Eng Fract Mech 1998;59:521–42.

[36] Hwang CG, Wawrzynek PA, Ingraffea AR. On the virtual crack extension method for calculating the derivatives of energy release rates for a 3D planar crack of arbitrary shape under mode-I loading. Eng Fract Mech 2001;68:925–47.

[37] Leblond J-B, Lazarus V, Mouchrif S. Crack paths in three-dimensional elastic solids. II: three-term expansion of the stress intensity factors - applications and perpsectives. Int J Solids Struct 1999;36:105–42.

[38] Williams JG. On the calculation of energy release rates for cracked laminates. Int J Fract 1988;36:101–19.

[39] Kanninen MF. An augmented double cantilever beam model for studying crack propagation and arrest. Int J Fract 1973;9:83–92.

[40] Davidson BD, Schapery RA. A technique for predicting mode I energy release rates using a first-order shear deformable plate theory. Eng Fract Mech 1990;36:157–65.

[41] Sun CT, Zheng S. Delamination Characteristics of Double-Cantilever Beam and End-Notched Flexure Composite Specimens. Compos Sci Technol 1996;56:451–9.

[42] Davidson BD. An Analytical Investigation of Delamination Front Curvature in Double Cantilever Beam Specimens. J Compos Mater 1990;24:1124–37.

[43] Nilsson KF. On growth of crack fronts in the DCB-test. Compos Eng 1993;3:527–46.

[44] Sneddon IN. The distribution of stress in the neighbourhood of a crack in an elastic solid. Proc Roy Soc London, Ser A 1946;187:229–60.

[45] Mi Y, Aliabadi MH. Three-Dimensional Crack Growth Simulation Using BEM. Comput Struct 1994;52:871–8.

[46] Rybicki EF, Kanninen MF. A finite element calculation of stress intensity factors by a modified crack closure integral. Eng Fract Mech 1977;9:931–8.

[47] Krueger R. Virtual crack closure technique: History, approach, and applications. Appl Mech Rev 2004;57:109–43.

[48] Hussain MA, Pu SL, Underwood J. Strain energy release rate for a crack under combined mode I and mode II. Fract Anal ASTM STP 560 Am Soc Test Mater 1974:2–28.

[49] Chan SK, Tuba IS, Wilson WK. On the finite element method in linear fracture mechanics. Eng Fract Mech 1970;2:1–17.

[50] Irwin GR. Fracture I. In: Flugge, editor. Handb. der Phys. VI, Berlin, Germany: Springer Verlag; 1958, p. 558–90.

[51] Broek D. Elementary Engineering Fracture Mechanics. 4th Revise. Dordrecht, Netherlands: Kluwer Academic Publishers; 1991.

[52] Singh R, Carter BJ, Wawrzynek PA, Ingraffea AR. Universal crack closure integral for SIF estimation. Eng Fract Mech 1998;60:133–46.

[53] Shivakumar K, Tan P, Newman J. A virtual crack-closure technique for calculating stress intensity factors for cracked three dimensional bodies. Int J Fract 1988;36:R43–R50.

[54] Chen F, Shield R. Conservation laws in elasticity of the J-integral type. J Appl Math Phys 1977;28:1–22.

[55] Yau JF, Wang SS, Corten HT. A mixed-mode crack analysis of isotropic solids using conservation laws of elasticity. J Appl Mech 1980;47:335–41.

[56] Wang SS, Yau JF, Corten HT. A mixed-mode crack analysis of rectilinear anisotropic solids using conservation laws of elasticity. Int J Fract 1980;16:247–59.

[57] Banks-Sills L, Hershkovitz I, Wawrzynek PA, Eliasi R, Ingraffea AR. Methods for calculating stress intensity factors in anisotropic materials: Part I— z= 0 is a symmetric plane. Eng Fract Mech 2005;72:2328–58.

[58] Banks-Sills L, Wawrzynek PA, Carter BJ, Ingraffea AR, Hershkovitz I. Methods for calculating stress intensity factors in anisotropic materials: Part II—Arbitrary geometry. Eng Fract Mech 2007;74:1293–307.

[59] Cherepanov GP. Crack propagation in continuous media. J Appl Math Mech 1967;31:503–12.

[60] Rice JR. A path independent integral and the approximate analysis of strain concentration by notches and cracks. J Appl Mech 1968;35:379–86.

[61] Banks-Sills L. Update: application of the finite element method to linear elastic fracture mechanics. Appl Mech Rev 2010;63.

[62] Ishikawa H. A finite element analysis of stress intensity factors for combined tensile and shear loading by only a virtual crack extension. Int J Fract 1980;16:243–6.

[63] Nikishkov GP, Atluri SN. Calculation of fracture mechanics parameters for an arbitrary three-dimensional crack, by the “equivalent domain integral”method. Int J Numer Methods Eng 1987;24:1801–21.

[64] Hellen TK, Blackburn WS. The calculation of stress intensity factors for combined tensile and shear loading. Int J Fract 1975;11:605–17.

[65] Shivakumar KN, Raju IS. An equivalent domain integral method for three-dimensional mixed-mode fracture problems. Engineering 1992;42:935–59.

[66] Huber O, Nickel J, Kuhn G. On the decomposition of the J-integral for 3D crack problems. Int J Fract 1993;64:339–48.

[67] Davis BR, Wawrzynek PA, Ingraffea AR. 3-D simulation of arbitrary crack growth using an energy-based formulation – Part I: Planar growth. Eng Fract Mech 2014;115:204–20.

[68] Wu CH. Maximum-energy-release-rate criterion applied to a tension-compression specimen with crack. J Elast 1978;8:235–57.

[69] Henshell RD. Crack tip finite elements are unnecessary. Int J Numer Methods Eng 1975;9:495–507.

[70] Barsoum RS. On the use of isoparametric finite elements in linear fracture mechanics. Int J Numer Methods 1976;10:25–37.

[71] FRANC3D 6.0.5, Fracture Analysis Consultants, Inc., www.fracanalysis.com, Ithaca, NY, USA, 2013.

[72] ABAQUS 6.11-1, Dassault Systemes Simulia Corp., Providence, RI, USA, 2011.

[73] Banks-Sills L, Sherman D. On quarter-point three-dimensional finite elements in linear elastic fracture mechanics. Int J Fract 1989;41:177–96.

[74] Anderson TL. Fracture Mechanics: Fundamentals and Applications. Third Edit. Boca Raton: Taylor & Francis Group; 2005.

[75] Kassir MK, Sih GC. Three-dimensional crack problems. In: Sih GC, editor. Mech. Fract. II, Leyden: Noordhoff International Publishing; 1975.

[76] Arcan M, Hashin Z, Voloshin A. A Method to Produce Uniform Plane-stress States with Applications to Fiber-reinforced Materials. Exp Mech 1978;18:141–6.

[77] Banks-Sills L, Arcan M, Bortman Y. A mixed mode fracture specimen for mode II dominant deformation. Eng Fract Mech 1984;20:145–57.

[78] Maitireyimu M, Kikuchi M, Geni M. Comparison of Experimental and Numerically Simulated Fatigue Crack Propagation. J Solid Mech Mater Eng 2009;3:952–67.

[79] Levan A, Royer J. Part-circular surface cracks in round bars under tension, bending and twisting. Int J Fract 1993;61:71–99.

[80] Ismail AE, Ariffin AK, Abdullah S, Ghazali MJ. Stress intensity factors under combined tension and torsion loadings. Indian J Eng Mater Sci 2012;19:5–16.

[81] Davidson BD, Krüger R, König M. Three-dimensional analysis of center-delaminated unidirectional and multidirectional single-leg bending specimens. Compos Sci Technol 1995;54:385–94.

[82] Polaha JJ, Davison BD, Hudson RC, Pieracci A. Effects of Mode Ratio, Ply Orientation and Precracking on the Delamination Toughness of a Laminated Composite. J Reinf Plast Compos 1996;15:141–73.

[83] Hull D. Tilting cracks: the evolution of fracture surface topology in brittle solids. Int J Fract 1993;62:119–38.

[84] Ortiz M, Pandolfi A. Finite-Deformation Irreversible Cohesive Elements for Three-Dimensional Crack-Propagation Analysis. Int J Numer Methods Eng 1999;44:1267–82.

[85] Moes N, Gravouil A, Belytschko T. Non-planar 3D crack growth by the extended finite element and level sets - Part I: Mechanical model. Int J Numer Methods Eng 2002;53:2549–68.

[86] Gravouil A, Moes N, Belytschko T. Non-planar 3D crack growth by the extended finite element and level sets - Part II: Level set update. Int J Numer Methods Eng 2002;53:2569–86.

[87] Sukumar N, Prévost J-H. Modeling quasi-static crack growth with the extended finite element method Part I: Computer implementation. Int J Solids Struct 2003;40:7513–37.

[88] Sukumar N, Chopp DL, Bechet E, Moes N. Three-dimensional non-planar crack growth by a coupled extended finite element and fast marching method. Int J Numer Methods Eng 2008;76:727–48.

[89] Bouchard PO, Bay F, Chastel Y, Tovena I. Crack propagation modelling using an advanced remeshing technique. Comput Methods Appl Mech Eng 2000;189:723–42.

[90] Maligno AR, Rajaratnam S, Leen SB, Williams EJ. A three-dimensional (3D) numerical study of fatigue crack growth using remeshing techniques. Eng Fract Mech 2010;77:94–111.

[91] Khoei AR, Eghbalian M, Moslemi H, Azadi H. Crack growth modeling via 3D automatic adaptive mesh refinement based on modified-SPR technique. Appl Math Model 2013;37:357–83.

[92] Moslemi H, Khoei AR. 3D adaptive finite element modeling of non-planar curved crack growth using the weighted superconvergent patch recovery method. Eng Fract Mech 2009;76:1703–28.

[93] Ruiz G, Pandolfi A, Ortiz M. Three-dimensional cohesive modeling of dynamic mixed-mode fracture. Int J Numer Methods Eng 2001;52:97–120.

[94] Gürses E, Miehe C. A computational framework of three-dimensional configurational-force-driven brittle crack propagation. Comput Methods Appl Mech Eng 2009;198:1413–28.

[95] Krueger R. An Approach to Assess Delamination Propagation Simulation Capabilities in Commercial Finite Element Codes 2008.

[96] Erdogan F, Sih GC. On the Crack Extension in Plates Under Plane Loading and Transverse Shear. J Basic Eng 1963;85:519–25.

[97] Griffith AA. The Theory of Rupture. Proc. First Int. Cong. Appl. Mech., Delft: 1924, p. 55–63.

[98] Davis BR, Wawrzynek PA, Hwang CG, Ingraffea AR. Decomposition of 3-D Mixed-Mode Energy Release Rates using the Virtual Crack Extension Method. Eng Fract Mech, under review.

[99] Finnie I, Saith A. A Note on the Angled Crack Problem and the Directional Stability of Cracks. Int J Fract 1973;9:484–6.

[100] Cotterell B, Rice JR. Slightly curved or kinked cracks. Int J Fract 1980;16:155–69.

[101] Lazarus V, Buchholz F-G, Fulland M, Wiebesiek J. Comparison of predictions by mode II or mode III criteria on crack front twisting in three or four point bending experiments. Int J Fract 2008;153:141–51.

[102] Lin B, Mear ME, Ravi-Chandar K. Criterion for initiation of cracks under mixed-mode I + III loading. Int J Fract 2010;165:175–88.

[103] Sommer E. Formation of fracture “lances” in glass. Eng Fract Mech 1969;1:539–46.

[104] Knauss WG. An Observation of Crack Propagation in Anti-Plane Shear. Int J Fract Mech 1970;6:183–7.

[105] Gao H. Three-Dimensional Slightly Nonplanar Cracks. J Appl Mech 1992;59:335–43.

[106] Xu G, Bower AF, Ortiz M. An analysis of non-planar crack growth under mixed mode loading. Int J Solids Struct 1994;31:2167–93.

[107] Leblond J-B, Karma A, Lazarus V. Theoretical analysis of crack front instability in mode I+III. J Mech Phys Solids 2011;59:1872–87.

[108] Citarella R, Buchholz F-G. Comparison of crack growth simulation by DBEM and FEM for SEN-specimens undergoing torsion or bending loading. Eng Fract Mech 2008;75:489–509.